②

Beam Combining
by
Phase Transition Nonlinear Media

Final Report

Rockwell International

2

Rockwell International

Rocketdyne Division
6633 Canoga Avenue
Canoga Park, California 91304

Beam Combining
by
Phase Transition Nonlinear Media

Final Report

DTIC
S ELECTE D
MAR 1 5 1990
D

February 1990

Contract N00014-87-C-0340
CDRL Seq. A003
(Unclassified)

Sponsored
by
The Strategic Defense Initiative Office
Innovative Science and Technology
and
Monitored by

Office of Naval Research
800 North Quincy Street
Arlington, Virginia 22217-5000

RI/RD 90-121

DISTRIBUTION STATEMENT A
Approved for public release
Distribution Unlimited

Rockwell International

Rockwetdyne Division
6633 Canoga Avenue
Canoga Park, California 91304

Beam Combining
by
Phase Transition Nonlinear Media
Final Report

1 June 1987 through 28 February 1990
Contract N00014-87-C-0340
CDRL Seq. A003
(Unclassified)
Prepared for
Scientific Officer
Lasers and Optics Division
Office of Naval Research
800 North Quincy Street
Arlington, Virginia 22217-5000

Attn: Dr. Matthew B. White (Code 1112L0)

Accesion For		
NTIS CRA&I	☑	
DTIC TAB	☐	
Unannounced	☐	
Justification		
By Per Call		
Distribution /		
Availability Codes		
Dist	Avail and / or Special	
A-1		

Prepared by:

Glenn Bennett

Kevin Schehrer

Victor Wang
Principal Investigator

QUALITY INSPECTED 4

RI/RD 90-121

STATEMENT "A" per Matthew White
ONR/Code 1112L0
TELECON 3/14/90 VG

FOREWORD

This report was prepared by Advanced Programs, Rocketdyne Division, Rockwell International under Contract No. N00014-87-0340. The period of performance extended from June 1, 1987 to February 28, 1990 and the principal authors of this report are G. Bennett, K. Schehrer, and Victor Wang. The Program Manager was R. N. Hindy, the principal contributor to the analysis in Section 2 was K. Schehrer, the principal contributor to the stimulated experiments as well as the theory was G. Bennett, and the Principal Investigator was Victor Wang. Acknowledgements of all the contributors to this work are listed on the following page.

The authors wish to acknowledge the support of the Optical Systems Department and the technical support of R. McGraw, D. Rogovin, and M. Khoshnevisan of the Rockwell Science Center. We also wish thank M. B. White of ONR and Lt. K. Morton of SPAWAR, the technical monitors of the program, for their interest and support of the program.

ACKNOWLEDGEMENTS

Theory

- Glenn Bennett
- Kevin Schehrer
- T.T. Yang
- R. McGraw

Experiment

- P. Roullard
- N. Miller
- K. Jackson
- R. Hassler
- G. Bennett
- P. Stanley
- R. Kim
- R. Demers
- K. Carrillo

Design

- G. Culp
- M. Stormo
- L. Rojas
- J. Tellier
- D. Wiltz
- J. Osmundsen

Program Management

- R. N. Hindy

TABLE OF CONTENTS

SECTION 1

INTRODUCTION AND SUMMARY

1.1 Introduction and Summary

This Final Report describes the work carried out for the SDIO-IST Office, under the supervison of the Office of Naval Research, to develop a high response nonlinear material suitable for use with high power lasers. The objective of this program was to demonstrate the use of a gas or liquid near a phase transition as an efficient phase conjugation material. We have attempted to explore this enhancement for both static equilibrium conditions near the critical point and for nonequilibrium conditions created by sudden expansion in a nozzle. The achievement of such a high response nonlinear material would make practical the application of nonlinear phase conjugate techniques to the beam combining of multiple lasers with a coherence characteristic of a single laser. [illegible]

1.2 Background

The desire to preserve the coherence that a laser can provide has placed unprecedented demands on the accuracy of optical components and structures. In large lasers these requirements have limited the scalability of lasers to less than the size needed for weapons and in smaller lasers these optical requirements have limited their widespread applicatiion because of high cost. Nonlinear phase conjugation has been one of the most promising techniques for overcoming this barrier. Due to the relatively weak nonlinearities of existing media,application of theses methods has been limited to pulsed lasers of high peak power but low average power. The near-critical point phase transition nonlinear media developed in this program addresss this problem by providing an increase in response of several orders of magnitude at a small penalty of speed of response. This characteristic of nonlinear media where speed is traded off for response is illustriated in Figure1.2-1.

Since most applications require the correction of disturbances induced by flow or acoustic disturbances, response times of less than one millisecond are all that are necessary. For many applications, the response times of typical nonlinear media are faster than necessary. However, higher response can greatly increase the utility of nonlinear media.

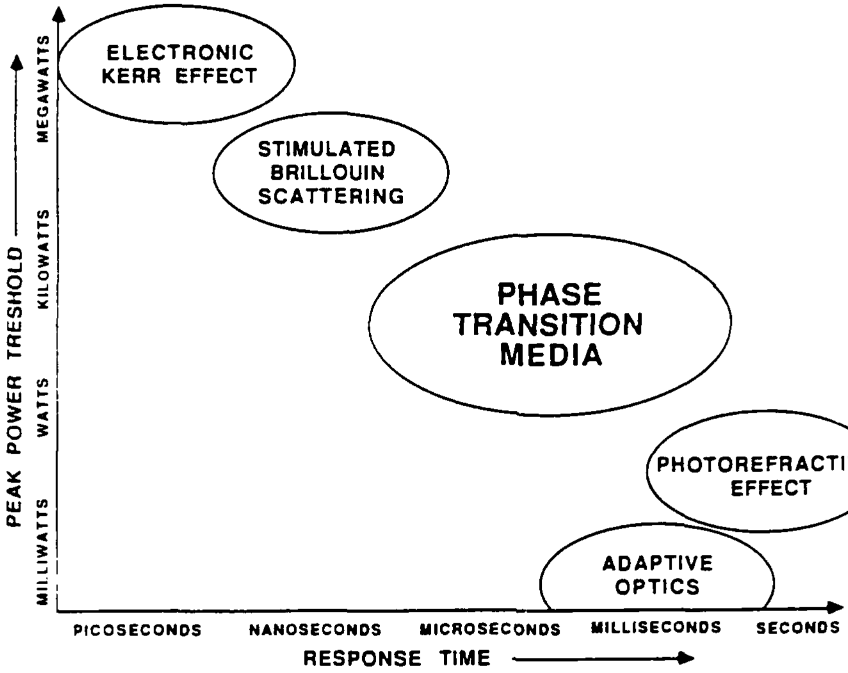

Fig. 1.2-1 Threshold power and response time classification of some phase conjugate media.

1.3 Highlights and Accomplishments

The aim of this program was to demonstrate optical phase conjugation at a lower power level than was previously required in conventional nonresonant media. This goal was achieved late in the program using stimulated scattering in a simple near critical point static fluid. In reaching this demonstration a new substantially complete understanding of the optical interaction of fluids near their critical phase transition was developed. While the original intentions were to exploit the nonequilibrium conditions within a flowing fluid in the throat of a nozzle using degenerate four wave mixing (DFWM), the achievement of stimulated scattering in a near critiical point fluid (NCPF) is a great simplification. Some highlights of this program are:

- the development of an understanding of the nonlinear optics of NCPF that quantifies the phase conjugate reflectivity, time dependence, signal to noise ratio, and optimum interaction length for NCPF..

- the identification of thermal nonlinearities in and their competition with electrostrictive nonlinearities in NCPF.
- the prediction of the transient response times for stimulated Rayleigh scattering (SRS) and stimulated Brillouin scatttering (SBS) and their competition in NCPF.
- the development of a flowing, nozzle-driven fluid system that demonstrates two-phase operation in the metastable region of spontaneous nucleation.
- the measurement of SBS and DFWM in the transient (short pulse) regime in NCPF.
- the demonstration of SRS with giant nonlinearities in NCPF using 20 μsec long pulses.

This last accomplishment of very high response in NCP Freon 116 validates the basic premise of enhanced response near a phase transition. This fast response nonlinear media makes practical the phase conjugation and beam combining of continuous wave high power lasers of almost any wavelength. The enhancement of nonlinear response exceeds what is possible with any other nonresonant materials suited for high power operation that is known to date and the speed of response greatly exceeds existing candidates such as Artifical Kerr media and photorefractors.

The physics of the new type of nonlinear interaction with NCPF and two-phase fluids is discussed in Section 2 and the experiments that guided and validated our theoritical developments are described in Section 3. Section 4 provides a short Summary of the program, offer suggestions for future research and development, and outlines the merits of this technology for application to high power lasers.

SECTION 2

THE THEORY OF NEAR CRITICAL POINT COMPRESSIBILITY-ENHANCED RESPONSE IN THE SINGLE PHASE REGION

The isothermal compressibility of near-critical-point fluids (NCPFs) can be quite large. This was the motivation for the initial proposition that such media might be used as highly efficient nonlinear optical media. An underlying theme in our research has been to explore relatively simple ways of exploiting NCPFs, so that they can be used practically, in "real world" environments. Thus, for example, we have not attempted to maintain temperatures to millikelvin tolerances. This relatively coarse temperature control impacts the lower limit in laser power that results in a detectable signal. This will be thoroughly discussed in the following analyses.

In Section 2.1 we present a number of analytical results on degenerate four wave mixing (DFWM). The largest part of our theoretical work pertained to DFWM, partly because a large portion of the experimental effort was expended on DFWM, and partly because we often found it easier to develop intuition in DFWM rather than e.g. stimulated scattering since the refractive index grating is stationary in DFWM. Included at the beginning of Section 2.1 is a discussion of some of the basic equations and ideas that are fundamental to an analysis of DFWM in NCPFs.

In Section 2.1.1 we consider the simple case of two counterpropagating beams of equal frequency, and the nonlinear interaction that results in a refractive index grating being written in the NCPF. By using such a simple case it is easy to focus attention on the most important aspects of nonlinear optical interactions in NCPFs. In particular, we point out the dependence on isothermal compressibility (κ_T), and the competition of electrostrictive and thermal effects in grating formation.

In Section 2.1.2 we derive an expression for the reflectivity, neglecting spontaneous scattering. However, since the spontaneous scattering and reflectivity are both enhanced near the critical point, we treat the reflectivity as an intermediate result. The more important result is the signal to noise ratio that is derived in Section 2.1.5.

In Section 2.1.3 the relation between the scattering due to spontaneous density fluctuations and the nonlinear susceptibility of NCFP's is emphasized. A physical picture of the thermodynamics of grating formation emerges as it is shown that the laser energy density required to write a grating must dominate the thermal energy density per grating mode.

In Section 2.1.4 the linearized time-dependent hydrodynamic equations are solved for a grating generated by either thermal heating or electrostrictive pressure. In particular, the equations are solved an optical field which is a step function in time, and the transient response of the grating is studied. As an example of this transient behavior, the NCP DFWM response, from lasers whose pulse duration is much less than the grating formation time, is found to be a ratio where the increasing DFWM gain is divided by the increasing grating formation times. This gain versus formation time competition results in no NCP enhancement for DFWM using short pulse lasers.

In Section 2.1.5 an analysis of the spontaneous light scattering into a detector in a typical experimental configuration [illegible]erformed. This allows us to derive an expression for the signal to noise ratio expected from NCPF experiments. The *SNR*, discussed in Section 2.1.5, is arguably the most important quantity that we discuss since, in the end, it determines the utility of any device that uses an NCPF for DFWM. In this section we show that spontaneous scattering (noise) and reflectivity are enhanced in the same way by the diverging isothermal compressibility. However, only near the critical point can the interaction length be close to optimum, and in this sense the SNR is greatly enhanced near the critical point.

Throughout the work that follows, we use the Redlich Kwong equation of state for the media we consider. This equation of state can be written

$$P = \frac{RT}{\rho_m^{-1} - b} - \frac{a}{\sqrt{T}\left(\rho_m^{-1} + b\right)\rho_m^{-1}} \tag{2-1}$$

where R is the ideal gas constant, T is the temperature in degrees Kelvin (K), P is the pressure in J/m^3, and ρ_m is the molar density in mole/m^3. The critical point values for P, V, and T, along with the constants a and b are given in Table 2-1, for Freon 116 (C_2F_6). The T_c shown in the table is that which is consistent with the values preceding it (a,b,P_c,V_c), and the implied precision is only useful in calculations and should not be construed as the precision with which the true T_c is known.

Table 2-1. Parameters for Freon 116		
parameter	value	units
a	14.5866	J mole^{-1} K$^{1/2}$
b	7.10068×10^{-5}	m^3 mole^{-1}
P_c	2.96940×10^{6}	J/m^3
V_c	3.66051×10^{4}	m^3 mole^{-1}
T_c	292.6993342	K

In Fig. 2-1 we show a set of isotherms on a P vs. V plot for C_2F_6, we have restricted the plot to values of the thermodynamic variables that are close to the critical values. In addition to the isotherms we show the coexistence curve, which is obtained by requiring that the chemical potential of liquid and vapor states—μ_l and μ_g, respectively—be equal at coexistence. This can also be expressed

$$\mu_l - \mu_g = \int_{V_1}^{V_2} V dP = 0 \qquad (2\text{-}2)$$

i.e., for V_1, V_2 defining the coexistence curve, the area under the P vs V curve between V_1 and V_2 is zero. The spinoidal curve is also shown in Fig. 2-1. It consist of the points where the isothermal compressibility diverges. The spinoidal lies below the coexistence curve and so—except at the critical point—it is in the metastable region. The isotherms are for temperatures from 287.7 to 294.7 in increments of 0.25 °K. The pressure is in lbs/in^2, and the volume is in m^3/mole.

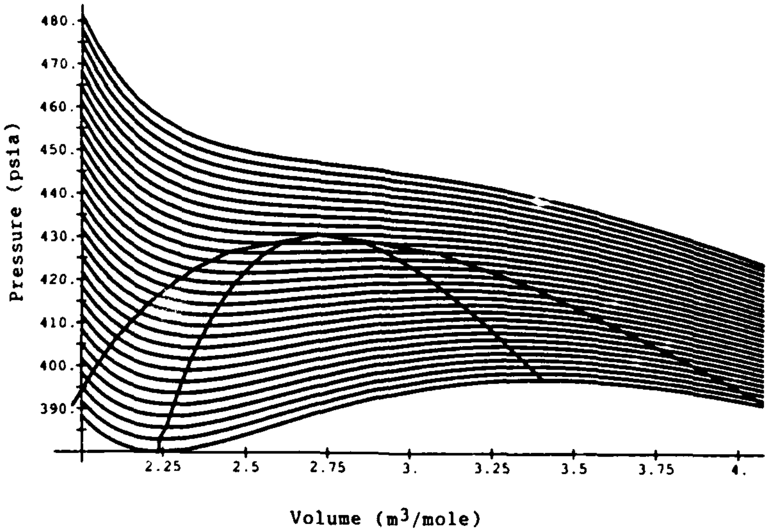

Fig. 2-1 Pressure -Volume relation for typical fluids.

The interest in using NCPF's for nonlinear optical processes is motivated by the fact that their isothermal compressibilities become very large near the critical point. To illustrate, and quantify this statement we used Eq. (2-1) to compute the isothermal compressibility

$$\kappa_T \equiv -\frac{1}{V}\left(\frac{\partial V}{\partial P}\right)_T \tag{2-3}$$

for C_2F_6 at temperatures in a region above the critical temperature. A plot of these data is shown in Fig. 2.1-2. Evidently, the region over which the isothermal compressibility can be considered "divergent" is extremely narrow; i.e., confined to small $T-T_c$. Of course, caution is due when using any equation of state near the critical point. Consequently, the results shown in Fig. 2.1-2 need to be verified experimentally.

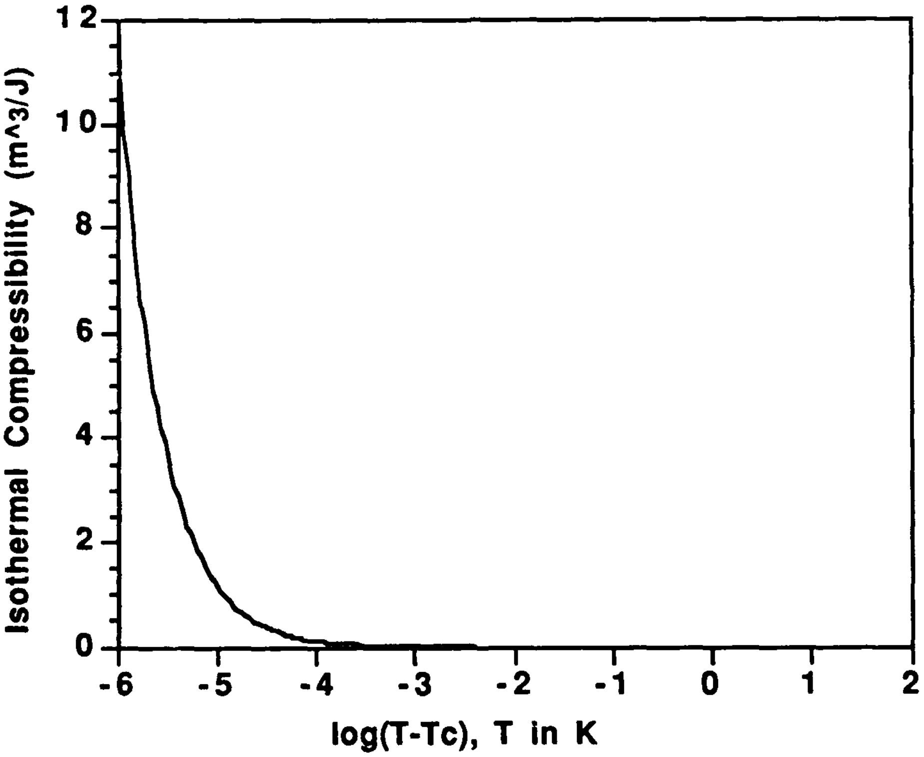

Fig. 2-2. Isothermal compresibility κ_T as a function of temperature difference from the critical temperature. The range in tempertature has been compressed by taking the logarithm base ten of the difference: $(T\text{-}T_c)$

2.1 Degenerate Four Wave Mixing in Near Critical Point Fluids

Degenerate four wave mixing (DFWM) requires that only stationary refractive index gratings be "written" in a medium. And, in this sense, DFWM is easier to analyze than stimulated processes, where some care must be taken in analyzing time dependencies in the transient case, and the dynamics of the medium in general. However, DFWM has the disadvantage (with respect to stimulated scattering) that it requires accurate beam alignment.

The DFWM configuration we use throughout this section is illustrated in Fig. 2.1-1. The beams are assumed collinear, and propagate along the z direction, interacting in a region of length L. At least one counterpropagating pair of beams is of a single polarization, the polarization of the output is then determined by the polarization of the third input. Since the susceptibility is assumed to be isotropic the configuration is equivalent for any two input polarizations, regardless of their relative angle. With this equivalence identified, we will consider a specific configuration to simplify the wording of what follows. Referring to Fig. 2.1-1, we let A_1 and A_2 be pumps of identical polarization, and A_4 is the phase conjugate reflection of A_3. We assume in this section that the temperature is far enough from the critical point so that the anisotropies (see Appendix 5.2) that become important very near the critical point can be ignored.

The interference of the counterpropagating beams A_2 and A_3 produces an intensity grating in the interaction volume. If A_2 is a plane wave, then the transverse phase profile of A_3 is manifested as a transverse intensity profile. This intensity profile "writes" a refractive index grating in the medium, and this variation in refractive index causes plane wave A_1 to be reflected (scattered coherently) into A_4, which has a phase profile conjugate to A_3.

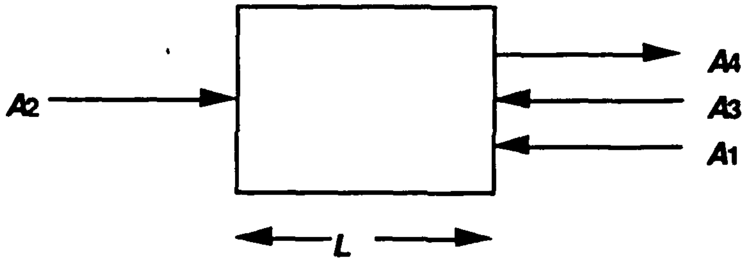

Fig. 2.1-1. Schematic representation of the four wave mixing geometry. All four beams are colinear and are assumed to interact only in the region of length L. The transverse extent of the interaction is determined by the transverse beam profile.

2.1.1 Competition Between Electrostrictive and Thermal Gratings

The variation in the dielectric constant (and refractive index) that arises due to variations in pressure (P) and temperature (T) can be obtained by treating the dielectric constant ε as a function of the independent thermodynamic variables P and T and computing the variation:

$$\delta\varepsilon = \frac{\partial\varepsilon}{\partial\rho}\left[\left(\frac{\partial\rho}{\partial T}\right)_P \delta T + \left(\frac{\partial\rho}{\partial P}\right)_T \delta P\right]. \tag{2.1.1-1}$$

It is worthwhile to cast $(\partial\rho/\partial T)_P$ in a form that exhibits explicitly the dependence on the isothermal compressibility. Treating V as a function of T and P we can write

$$dV = \left(\frac{\partial V}{\partial T}\right)_P dT + \left(\frac{\partial V}{\partial P}\right)_T dP. \tag{2.1.1-2}$$

And, treating P as a function of T and V

$$dP = \left(\frac{\partial P}{\partial T}\right)_V dT + \left(\frac{\partial P}{\partial V}\right)_T dV. \tag{2.1.1-3}$$

Substitution of Eq. (2.1-1-3) into Eq. (2.1-1-2) results in

$$\left(\frac{\partial V}{\partial T}\right)_P = -\left(\frac{\partial V}{\partial P}\right)_T \left(\frac{\partial P}{\partial T}\right)_V. \tag{2.1.1-4}$$

Then, using $V=\rho^{-1}$, whence

$$\frac{\partial V}{\partial T} = -\frac{1}{\rho^2}\frac{\partial\rho}{\partial T}, \tag{2.1.1-5}$$

and substitution of Eqs. (2.1.1-4) and (2.1.1-5) into Eq. (2.1.1-1) we obtain

$$\delta\varepsilon = \kappa_T \rho \frac{\partial\varepsilon}{\partial\rho}\left[\delta P - \left(\frac{\partial P}{\partial T}\right)_V \delta T\right]. \tag{2.1.1-6}$$

Equation (2.1-1-6) is an important result. It will be shown that neither δP nor δT depend on κ_T; thus their near critical point influence on $\delta\varepsilon$ is seen to be the same. Stated more explicitly, $\delta\varepsilon$ is proportional to both δP and $(\partial P/\partial T)_V \delta T$ with proportionality constant κ_T.

The Clausius Massotti relation relates the density to the dielectric constant

$$\rho = C\frac{\varepsilon - \varepsilon_0}{\varepsilon + 2\varepsilon_0}, \tag{2.1.1-7}$$

where C is a numerical medium specific constant. Using Eq. (2.1.1-7) one can show that

$$\rho\frac{\partial\varepsilon}{\partial\rho} = \frac{\varepsilon_0}{3}\left(n^2 - 1\right)\left(n^2 + 2\right), \tag{2.1.1-8}$$

where

$$n^2 = \frac{\varepsilon}{\varepsilon_0}, \tag{2.1.1-9}$$

and n is the refractive index.

Consider a grating that is produced by two counterpropagating beams having the same intensity, and direction of polarization. The total electric field can be written

$$E = A_0\frac{1}{2}\left\{\exp[ikz - i\omega t - \alpha z/2] + \exp[-ikz - i\omega t - \alpha(L - z)/2] + c.c.\right\}\exp\left(-\frac{r^2}{w_0^2}\right), \tag{2.1.1-10}$$

where a TEM_{00} beam profile is assumed with spot size w_0, and α is d loss coefficient that includes absorptive losses (α_d) and scattering losses (α_S); i.e.

$$\alpha \equiv \alpha_d + \alpha_S \tag{2.1.1-11}$$

The intensity is obtained from $E \cdot E^*$ using Eq. (2.1.1-10)

$$I = I_0\left[e^{-\alpha z}\left(1 + e^{-\alpha L}\right) + 2I_0e^{-\alpha L/2}\cos(2kz)\right]\exp\left(-2r^2/w_0^2\right), \tag{2.1.1-12}$$

where I_0 is the peak intensity of either of the individual beams.

The rate at which energy is deposited into an element of the medium of length δz and with transverse dimensions much larger than the spot size (w_0) is obtained by using Eq. (2.1.1-12) for the intensity, and interpreting α in the standard way

$$\delta U = \alpha_d \delta z I_0 \left[\left(1 + e^{-\alpha L}\right) e^{-\alpha z} + 2e^{-\alpha L/2} \cos(2kz) \right] \int_{-\infty}^{+\infty} \int_{-\infty}^{+\infty} dx dy \exp\left[-2\left(x^2 + y^2\right) / w_0^2 \right],$$

(2.1.1-13)

where δU has dimensions of power. Performing the integration in Eq. (2.1.1-13) and letting δU and δz approach zero results in

$$\frac{\partial U}{\partial z} = \alpha_d I_0 \left[\left(1 + e^{-\alpha L}\right) e^{-\alpha z} + 2e^{-\alpha L/2} \cos(2kz) \right] \frac{\pi w_0^2}{2}. \tag{2.1.1-14}$$

The integration over z now gives the time rate of energy is deposition at the point z

$$U_{in} = I_0 \left\{ \frac{\alpha_d}{\alpha} \left(1 + e^{-\alpha L}\right) e^{-\alpha z} + \frac{\alpha_d}{k} e^{-\alpha L/2} \sin(2kz) \right\} \frac{\pi w_0^2}{2}. \tag{2.1-1-15}$$

If one constructs an arbitrary surface inside the medium, then the heat flow per unit area per unit time across that surface is given by [1]

$$H_{out} = -\lambda_T \frac{\partial T}{\partial n}, \tag{2.1-1-16}$$

where λ_T is the thermal conductivity, and $\partial T/\partial n$ is the gradiant in the temperature along the outward normal to the surface. It is intuitively obvious, from Eq. (2.1.1-13), that the "hottest" part of the medium for any plane perpendicular to z is at the center, x=y=0. And, for typical spot sizes (≈>100 μm), and typical wavelengths (≈< 1 μm), the gradiant in temperature is usually greatest along z. (There is the obvious exception at points z such that $2kz=n\pi$, where $n=\{0,1,2...\}$.) Thus, to obtain an approximate solution for $\delta T(z)$, we take

$$U_{out} = -\lambda_T \frac{\partial T}{\partial z} \pi w_0^2. \tag{2.1.1-17}$$

We are interested here only in the δT that produces a refractive index grading, and we therefore neglect the slowly varying part in Eq. (2.1-1-15) when we equate Eqs. (2.1-1-15) and (2.1-1-17). After integration with respect to z we get

$$\delta T = \frac{\alpha_d}{4k^2 \lambda_T} \cos(2kz) \exp[-\alpha L / 2] \tag{2.1.1-18}$$

for the δT grating. With use of Eq. (2.1.1-9) this can be cast in the convenient form

$$\delta T = \frac{\alpha_d \lambda_0^2}{16\pi^2 n^2 \lambda_T} \cos(2kz) \exp[-\alpha L / 2], \tag{2.1-1-19}$$

where λ_0 is the wavelength of light in vacuum.

We now turn to a computation of the δP grating that is produced by electrostriction. Electrostriction is discussed in numerous textbooks, and it is found that δP is given by

$$\delta P = \frac{1}{2}\rho\left(\frac{\partial \varepsilon}{\partial \rho}\right)E^2, \tag{2.1.1-20}$$

which, with Eqs. (2.1.1-8) and (2.1.1-10) results in

$$\delta P = \frac{2(n^2-1)(n^2+2)}{3cn} I_0 e^{-\alpha L/2} \cos(2kz), \tag{2.1.1-21}$$

where the intensity and electric field are related by

$$\frac{1}{2}E^2 = \frac{1}{c\varepsilon_0 n} I \tag{2.1.1-22}$$

in SI units. Again, we consider ony the grating, neglecting slowly varying terms.

Substitution of Eqs. (2.1.1-21) and (2.1.1-19) for δP and δT, respectively, into Eq. (2.1.1-6) for $\delta\varepsilon$ gives

$$\delta\varepsilon = \delta\varepsilon_0 \cos(2kz), \tag{2.1.1-23a}$$

where

$$\delta\varepsilon_0 \equiv K_T D\{\Delta_P - \Delta_T\} I_0 e^{-\alpha L/2}, \tag{2.1-1-23b}$$

$$D \equiv \frac{\varepsilon_0(n^2-1)(n^2+2)}{3}, \tag{2.1-1-23c}$$

$$\Delta_P \equiv \frac{2(n^2-1)(n^2+2)}{3cn}, \tag{2.1-1-23d}$$

and

$$\Delta_T \equiv \left(\frac{\partial P}{\partial T}\right)_V \frac{\alpha_d \lambda_0^2}{16\pi^2 n^2 \lambda_T}. \qquad (2.1\text{-}1\text{-}23e)$$

Typically, $(\partial P/\partial T)_V$ is positive and $n^2>1$. Thus, Eq. (2.1.1-23b) shows that the temperature and pressure gratings are of opposite sign. They are competing effects in grating formation. Which of the two effects dominates can be computed by comparing Δ_p and Δ_T; i.e. the terms in brackets in Eq. (2.1-1-23b) with $\partial P/\partial T$ obtained from the equation of state.

The competition of thermal and electrostrictive effects results because the optical density decrease from increased temperature due to absorption is maximum at the same points where the optical density increases from increased pressure is maximum due to electrostrictive forces.

To compare Δ_P with Δ_T we define the dimensionless ratio

$$R_{PT} \equiv \frac{\Delta_P}{\Delta_T} = \frac{32\pi^2 n(n^2-1)(n^2+2)\lambda_T}{3c\alpha_d \lambda_0^2}\left(\frac{\partial P}{\partial T}\right)_V^{-1} \qquad (2.1.1\text{-}24)$$

Evidently, the electrostrictive effects are more prominent as the wavelength and thermal conductivity decrease. As the wavelength decreases the gradiant in temperature increases and, according to Eq. (2.1.1-17), this causes an increase in the rate at which energy moves from hot to relatively cool regions. Of course, a high thermal conductivity also contributes to the movement of energy from hot to cool regions. Both of these effects aid in heat transport, contributing to a homogenization of the thermal grating making it a less effective "reflector."

Note that R_{PT} does not depend on the isothermal compressibility i.e. both the thermal and electrostrictive contributions to $\delta\epsilon$ are enhanced in the same way by κ_T. This suggests that one could exploit either electrostrictive or thermal effects in producing a deep grating near the critical point.

We now compute R_{PT} for the specific case of Freon 116 (C_2F_6). The equation of state we use is

$$P(T,V) = \frac{RT}{V-b} - \frac{a}{\sqrt{T}V(V+b)}, \qquad (2.1.1\text{-}25)$$

where the parameters are given in Table ??. It is a simple matter to solve for $\partial P/\partial T$

$$\left(\frac{\partial P}{\partial T}\right)_V = \frac{R}{V-b} + \frac{a}{2T^{3/2}V(V+b)}. \qquad (2.1.1\text{-}26)$$

And computation of $\partial P/\partial T$ at the critical point gives $\partial P/\partial T = 5.67\times10^{4}$ N m^{-2} K^{-1}. For the thermal conductivity we use the value provided in Dupont supplied data at 200 ^{o}K for liquid phase, $\kappa_C = 7.39\times10^{-2}$ J m^{-1} sec^{-1} K^{-1}. Substitution of the numbers into Eq. (2.1-1-24) gives, at the critical point,

$$R_{PT} = \frac{5.23\times10^{-14}}{\alpha_d\lambda_0^2}, \quad [\lambda_0] = m, \quad [\alpha_d] = m^{-1}. \qquad (2.1.1\text{-}27)$$

And, for the two cases of primary interest to us—owing to the lasers that are most accessible in our laboratories—we find that the crossover from thermal to electrostrictive dominance; i.e. when $R_{PT}=1$, obtains when $\alpha_d(1.06\ \mu\text{m}) = 4.56\times10^{-4}$ cm^{-1} for a Nd:YAG laser, and $\alpha_d(514\ \text{nm}) = 1.98\times10^{-3}$ cm^{-1} for an argon ion laser. These are extremely small values for absorption, and if electrostrictive effects are to be exploited, one must have samples that are free of absorbing impurities, this in turn demands a very clean mechanical system that holds and flows the fluid.

In our experimental work, we took care to ensure the purity of the fluid so that the electrostrictive effect, was exploited. However, due to the limitations of our laboratories, we were unable to verify experimentally thatα_d (was sufficiently small. The calculations above came late in the program and so there was insufficient time to explore various ways to enhance the absorption so that the Δ_T term was strongly dominant. One option we did consider was to dissolve an absorbing material in the Freon 116. The absorption would need to occur at the incident wavelength. We expect that if the relaxation is radiationless, the temperature of the Freon 116 would rise. One possible difficulty in using strong absorption is that the local heating could cause the fluid to be convective on small scales so that the scattering by the turbulence might overwhelm the scattering by the intensity produced grating.

2.1.2 Reflectivity in Degenerate Four Wave Mixing

Consider a degenerate four wave mixing (DFWM) experiment , where the total field present is given by

$$E_j = \frac{1}{2}\left\{e_{1j}A_1 \exp[ikz - \alpha z/2] + e_{2j}A_2 \exp[-ikz - \alpha(L-z)/2]\right.$$

$$\left. + e_{3j}A_3 \exp[ikz - \alpha(L-z)/2] + e_{4j}A_4 \exp[-ikz - \alpha z/2] + c.c.\right\} \qquad (2.1.2\text{-}1)$$

e_{ij} is the component of polarization in the j'th direction for the i'th field, A_i is the slowly spatially varying i'th field amplitude at steady state, k is the wavevector in the medium, L is the interaction length, α is the loss coefficient, which with *c.c.* denotes the complex conjugate. The wave equation follows from Maxwell's equations, which with the slowly varying envelope approximation (SVEA), gives the spatial evolution. In particular, focus attention on the 4'th field, which is taken hereafter to be the signal, then [2]

$$\frac{\partial A_4}{\partial z} = i\frac{\mu_0\omega}{2cn}\delta\varepsilon_0 A_3^* \exp[-\alpha(z - L/2)]. \qquad (2.1.2\text{-}2)$$

Using the boundary condition $A_4(z=0)=0$, the spatial integration of Eq. (2.1.2-2), which gives the reflected signal, results in

$$A_4(L) = \frac{\mu_0\omega}{2c\alpha n}\delta\varepsilon_0 A_3^* e^{-\alpha L/2}\left(e^{\alpha L} - 1\right). \qquad (2.1.2\text{-}3)$$

We can now compute the ratio of the reflected signal to that which is incident

$$R = \frac{I_4}{I_3} = e^{-\alpha L}\left[\frac{\mu_0\omega D\kappa_T}{2n\alpha c}(\Delta_P - \Delta_T)\left(1 - e^{-\alpha L}\right)\right]^2 I_1 I_2. \qquad (2.1.2\text{-}4)$$

We define

$$\eta \equiv \frac{3^{3/2}}{2}e^{-\alpha L/2}\left(1 - e^{-\alpha L}\right), \qquad (2.1.2\text{-}5)$$

which is the same as η defined by Hellwarth in Eq. (3) of Ref. [3]. Then the intensity reflectivity is

$$R = \left[\frac{\omega D\kappa_T}{2n\varepsilon_0 c\alpha}(\Delta_P - \Delta_T)\right]^2 I_1 I_2 \frac{4}{27}\eta^2. \qquad (2.1.2\text{-}6)$$

This reflectivity is proportional to the square of the isothermal compressibility, and the square of the intensity for equal intensity pump beams. Unfortunately, as we will show in the next subsection, the signal to noise ratio is not enhanced in the same way by κ_T.

Owing to the dependence of $\delta\varepsilon$ on δT and δP, we see here the competition of electrostrictive and thermal effects that was discussed in the previous subsection.

Analogous to the analysis of Hellwarth [3], we compute the total loss coefficient that results in maximum reflectivity; i.e., we find the maximum in η from $d\eta/d(\alpha L)=0$ to get $\alpha L=\ln(3)$ and confirm that this is a maximum. This says that, with respect to the αL dependency, the reflectivity is maximized when $\alpha L\approx 1$; i.e., when the interaction length is approximately one inverse loss coefficient.

2.1.3 The Thermodynamic Relation Between Scattering and Reflectivity

As the system approaches the critical point, many of the thermodynamic variables diverge. This is usually seen in the optical phenomena known as critical opalescence. The divergent compressibility translates the thermal energy of the fluid into large density fluctuations. In other words, the $k_B T$ energy is acting much like the external laser in the fact that it causes perturbations in the density, although they will have random amplitudes and wavevectors, which scatter the laser beams in the four wave mixing process. This is seen as a loss of power to all of the participating inputs, but it is handled on the same footing as the mechanically enhanced nonlinear susceptibility and it scales with the thermodynamics in the same way as the DFWM gain.

This is the manifestation of the thermodynamic fluctuation-dissapation theorem for DFWM. This theorem states that the response of a system, i.e. its susceptibility, in this case the isothermal compressibility, is related to the magnitude of the density fluctuations in the system at a given temperature. A physical statement relating to DFWM is that there exists no DFWM gain without the associated noise due to scattering off of thermally driven density fluctuations. This can be more easily seen by writing the effective nonlinear susceptibility ;

$$\chi^{(3)} = \frac{1}{2}\kappa_T\left(\rho_0\frac{\partial\varepsilon}{\partial\rho}\right)_T^2 \qquad (2.1.3\text{-}1)$$

and the integrated volume scattering coefficient (alpha$_S$);

$$\alpha_S = \frac{8\pi^4 k_B T}{3\lambda^4\varepsilon_0^2}\kappa_T\left(\rho_0\frac{\partial\varepsilon}{\partial\rho}\right)_T^2 . \qquad (2.1.3\text{-}2)$$

Both the scattering loss term and the susceptibility have the same dependence on the mechanical susceptibility and the electrostrictive coefficient. The scattering loss term is the

Rayleigh scattering produced by thermal fluctuations as was first done by Einstein. It has the characteristic $1/\lambda^4$ dependence of Rayleigh scattering, but its magnitude is a function of the temperature and the isothermal compressibility. The DFWM response is driven by the energy per unit volume in the laser field, while the noise or scattering loss is driven by the thermal energy in the system. The ratio of the susceptibility to the scattering loss is given by:

$$\frac{\chi^{(3)}}{\alpha_S} = \frac{3\lambda^4 \varepsilon_0^2}{16\pi^4 k_B T} \quad . \tag{2.1.3-3}$$

This ratio is implicit in the electrostrictive DFWM reflectivity. The reflectivity can be written in such a manner as to explicitly show this dependency;

$$R = \left[e^{-\alpha L/2}\left(1-e^{-\alpha L}\right)\right]^2 \left(\frac{\chi^{(3)}}{\alpha_S}\right)^2 \frac{\mu_0^2 w^4 A_1^2 A_2^2}{4k^2} \quad . \tag{2.1.3-4}$$

In the above expression the divergences are now found only in the loss prefactor. This is the justification for saying that the static reflectivity is independent of the critical point thermodynamics if αL can be made constant.

Further insight into the reflectivity is obtained by substituting equation 2.1.3-3 into 2.2.3-4 along with writing intensities instead of field amplitudes;

$$R = \left[e^{-\alpha L/2}\left(1-e^{-\alpha L}\right)\right]^2 \frac{9 I_1 I_2}{\left(\frac{c}{n} k^3 k_B T\right)^2} \quad . \tag{2.1.3-5}$$

The denominator in the second factor on the right hand side has the units of watts^2. This power is clearly thermal in origin, because of the $k_B T$, and it represents the thermal power driving the fluctuations which degrade and smear out the laser impressed gratings. The implications are that in order to achieve high reflectivities the laser power must be greater than th[illegible]ower. In a more precise statement the thermal power is just the thermal energy per laser spatial mode, $(2\pi/\lambda)^3$, multiplied by the speed of light in the medium. It is this energy density per mode which the laser has to dominate in order to produce effective gratings in the fluid.

In conclusion the DFWM gain and the scattering loss due to density fluctuations are just different facets of the same dynamics in the fluid. They are linked by the thermodynamics and their ratio appears in the DFWM reflectivities. The reflectitity still retains the sensitivity to the critical point divergences in the scattering loss prefactor which comes into play only if the αL product cannot be maintained.

order of duration as the fluid time constants and the effective peak power over the laser pulse was much larger than what had been available before.

In conclusion of this section the dynamics of the fluid enter into the DFWM reflectivity not only in the enhancement of the mechanical response, but also in the formation times of that response. A usable low power system must have a laser pulse which is at least comparable to the formation time of the grating to obtain the near critical point increase in the reflectivity.

2.1.4 Dynamics of Degenerate Four Wave Mixing Near the Critical Point

A first step in understanding the dynamics of grating formation in near critical point fluids is to look at the decay and formation rates of fluctuations in the fluid. Gratings and fluctuations may be mathematically represented as a superpostion of the hydrodynamic modes in the fluid. The hydrodynamic modes are further divided into a thermal, or dissapative, mode and two acoustic, or traveling wave, modes. The DFWM grating is a thermal mode, stationary with wave vector $\boldsymbol{q}$, in contrast to the SBS grating which is an acoustic wave. In this derivation $\boldsymbol{q}$ is the wavevector of the material grating while $k = q/2$ is the optical wavevector which produces the grating. The classical linear hydrodynamic equations for density ρ, temperature T, and pressure P, are coupled to Maxwell's equations for the electric fields and the polarizations in the medium. The set of coupled equations are given by:

Conservation of mass;

$$\partial_t\rho_1 + \rho_0\psi_1 = 0 \qquad (2.1.4\text{-}1a)$$

Conservations of momenta;

$$\rho_0\,\partial_t\psi_1 + c_T^2\nabla^2\rho_1 + \rho_0\beta_T\, c_T^2\nabla^2 T_1 - \rho_0 D_V\nabla^2\psi_1 = \frac{\rho_0}{2}\left(\frac{\partial\varepsilon}{\partial\rho}\right)_T \nabla^2\left\langle E_T{}^2\right\rangle$$

(2.1.4-1b)

Conservation of energy;

$$\partial_t T_1 - \frac{(\gamma-1)}{\beta_T\rho_0}\partial_t\rho_1 - \gamma D_T\nabla^2 T_1 = \frac{\alpha_d c\varepsilon}{2n\rho_0 C_V}\left\langle E_T{}^2\right\rangle \qquad (2.1.4\text{-}1c)$$

Wave equation for the total electric field;

$$\nabla^2 E_T - \mu_0\varepsilon\,\partial_t^2 E_T = -\mu_0\partial_t^2 P_{NL} \tag{2.1.4-1d}$$

and the susceptibility as a function of the thermodynamic variables;

$$\chi_{NL} = \left(\frac{\partial\varepsilon}{\partial\rho}\right)_T \rho_1 + \left(\frac{\partial\varepsilon}{\partial T}\right)_\rho T_1 \; . \tag{2.1.4-1e}$$

Here ψ_1 is the divergence of the velocity field, E_T is the total elctric field, D_T is the thermal diffusivity of the fluid, c_T is the isothermal speed of sound, β_T is the thermal expansion coefficient, C_V is the specific heat at constant volume, α_d is the intrinsic absorption coefficient, D_V is the longitudinal kinematic viscosity and ε is the dielectric permittivity. the variables with the subscript 0 refer to the static or time averaged values for those variables, while the subscript 1 designates a small linear variation in the variable.

The initial step is to see what the equations of motion are for the fluid given without regard for the exact nature or geometry of the driving forces. This is done by solving for the density as a function of wavevector and either s or t depending whether or not we are working in the time or Laplace domain. Equations (2.1.4-1a and b) are combined to eliminate ψ_1:

$$-\partial_t^2\rho_1 + c_T^2\nabla^2\rho_1 + \rho_0\beta_T\, c_T^2\nabla^2 T_1 + D_V\nabla^2\partial_t\rho_1 = \frac{\rho_0}{2}\left(\frac{\partial\varepsilon}{\partial\rho}\right)_T \nabla^2\langle E_T{}^2\rangle \tag{2.1.4-2}$$

where the left hand side is a damped wave equation for the density and the right hand side is the electrostrictive driving term. The thermal driving term for the gratings enters through the intrinsic absorption in the energy conservation equation. In equation (2.1.4-2), the third and fourth terms on the left hand side correspond to the damping by thermal conduction and fluid viscosity respectively. These terms provide the phase shifts necessary for the stimulated scattering response to take place. Equations (2.1.4-1c and 2.1 4-2) are then Fourier-Laplace transformed:

$$s\bar{T}_1 - \frac{(\gamma-1)}{\beta_T\rho_0}s\bar{\rho}_1 + \gamma D_T q^2\bar{T}_1 = T_1(q,0) - \frac{(\gamma-1)}{\beta_T\rho_0}\rho_1(q,0) + \frac{\alpha_d c\,\varepsilon}{2n\rho_0 C_V}\langle E_T{}^2\rangle(q,s) \tag{2.1.4-3a}$$

and

$$s^2\bar{\rho}_1 - s\dot{\rho}_1(q,0) - \rho_1(q,0) + q^2 c_T^2\bar{\rho}_1 + \rho_0\beta_T\, c_T^2 q^2\bar{T}_1 +$$

$$D_V q^2 s\bar{\rho}_1 - D_V q^2 \rho_1(q,0) = \frac{\rho_0}{2}\left(\frac{\partial\varepsilon}{\partial\rho}\right)_T q^2 \langle E_T{}^2\rangle(q,s) \tag{2.1.4-3b}$$

where the tildas represent the Laplace transform variables and the initial values of the variables at time zero and wavevector q are explicitly shown. The transform of the time average of the electric field energy density is used to simplify the following results. The simplification stems from the fact that the fluid cannot mechanically respond to any driving frequencies close to the optical frequencies present in the system and they are dropped. This is really not necessary as the fluid response integrates the driving terms and the high frequency component would be suppressed in any event, but it reduces the number of driving terms one must consider in the problem. As an example of this time averaging, this nonlinearity does not support optical second harmonic generation because there is no bulk mechanical polarization wave which can be generated at twice the optical frequency. Equations (2.1.4-3a and b) can now be solved for just the density and the driving electric field. Substituting the expression for T_1:

$$\bar{T}_1 = \frac{\dfrac{(\gamma-1)}{\beta_T\rho_0}s\bar{\rho}_1 + T_1(q,0) - \dfrac{(\gamma-1)}{\beta_T\rho_0}\rho_1(q,0) + \dfrac{\alpha_d c\varepsilon}{2n\rho_0 C_V}\langle E_T{}^2\rangle(q,s)}{s+\gamma D_T q^2} \tag{2.1.4-4}$$

into (2.1.4-3b) and separating the response from the initial conditions and the driving terms:

$$\begin{aligned} s^2\bar{\rho}_1 + q^2 c_T^2\bar{\rho}_1 + D_V q^2 s\bar{\rho}_1 + c_T^2 q^2 \frac{(\gamma-1)}{s+\gamma D_T q^2}s\bar{\rho}_1 = {} \\ s\dot{\rho}_1(q,0) + \rho_1(q,0)\left(1 + D_V q^2 + \frac{c_T^2 q^2(\gamma-1)}{s+\gamma D_T q^2}\right) - \frac{\rho_0\beta_T\, c_T^2 q^2 T_1(q,0)}{s+\gamma D_T q^2} \\ -\left(\frac{\beta_T\, c_T^2 q^2 \alpha_d c\varepsilon}{2n\left(s+\gamma D_T q^2\right)C_V} - \frac{\rho_0}{2}\left(\frac{\partial\varepsilon}{\partial\rho}\right)_T q^2\right)\langle E_T{}^2\rangle(q,s) \end{aligned} \tag{2.1.4-5}$$

where the left hand side is still a damped wave equation for the density perturbations. The second line of the equation is the initial values of the density and temperature and the last two terms are the thermal input to the grating and the electrostrictive compression. It can now be seen that the thermal and electrostrictive are competing effects. In reading the time response from this equatiion the terms which have positive powers of s are more important at the higher frequencies, they correspond to the powers of the time derivative for that term. On the other hand, the terms which contain a $(s+\gamma D_T q^2)^{-1}$ integrate the response over a time period of $1/\gamma D_T q^2$, which is the characteristic time for thermal diffusion of the grating with wavevector q in the fluid. For laser inputs which are much shorter than $1/\gamma D_T q^2$, the electrostrictive term may dominate the thermal term even if the intrinsic absorption is high. For long duration laser inputs, much greater than the thermal diffusion time for the grating, a more detailed analysis may be required. This will be done in a later section of this report.

The next step is to cosider a specific DFWM senario where no feedback, no stimulated process, is allowed to couple the electric field to the density perturbations. A grating is written by two of the input beams and it is read out by a third beam and only the two writing beams interference terms are used to create the grating.

The solution to equation (2.1.4-5) for the case of an impressed sinusoidal intensity pattern which is turned on at $t=0$ and having no initial perturbations in ρ_1 or T_1 is done through the inverse Laplace transform. The spatial Fourier transform is left as it is because we are only cancerned with gratings of wavevector q. The transform pairs are given by:

$$\bar{\rho}_1(s,q) = \int_0^{\infty} dt\, \rho_1(t,q)\, e^{-st} \tag{2.1.4-6a}$$

$$\rho_1(t,q) = \frac{1}{2\pi j} \int_{\sigma-j\infty}^{\sigma+j\infty} ds\, \bar{\rho}_1(s,q)\, e^{st} \tag{2.1.4-6b}$$

where $j=\sqrt{-1}$. There are two asumptions which will be made at this point. The first one is for the non-depleted pump, small signal DFWM approximation. The second assumption is that the time scales of the processes will be long and we can neglect the second derivative term when compared with the first derivative terms. This latter assumption reduces the equations to a single diffusion equation for the density with a heat source and an electrostrictive pressure source:

$$\left(s + D_T q^2\right)\gamma c_T^2 q^2 \bar{\rho}_1(s,q) = \frac{E_T^2}{2s}\left[q^2 \rho_0 \left(\frac{\partial \varepsilon}{\partial \rho}\right)_T \left(s + \gamma D_T q^2\right) - \frac{\beta_T c_T^2 q^2 \alpha_d c \varepsilon}{n C_V} \right] \tag{2.1.4-7}$$

where n is the index of refraction and $E\ {}^{2}{}_{T}/s$ is the Laplace transform of the sinusoidal interference pattern of the writing beams. This equation is solved algerbraically for the density perturbation transform :

$$\bar{\rho}_1(s,q)=\frac{\frac{E_T^2}{2}\left[q^2\rho_0\left(\frac{\partial\varepsilon}{\partial\rho}\right)_T\left(s+\gamma D_T q^2\right)-\frac{\beta_T c_T^2 q^2\alpha_d c\varepsilon}{nC_V}\right]}{s\left(s+D_T q^2\right)\gamma c_T^2 q^2} \qquad (2.1.4\text{-}8)$$

where the time dependence is more clearly seen in the form of the two poles at $s=0$ and $s=-D_Tq^2$ and a zero for the electrostrictive driving force at $s=-\gamma D_Tq^2$ The inverse transform is easily done using the residue theorem because of the simple nature of the poles:

$$\rho_1(t,q)=\left(s\bar{\rho}_1(s,q)\big|_{s=0}+\left(s+D_T q^2\right)\bar{\rho}_1(s,q)e^{st}\Big|_{s=-q^2D_T}\right) \qquad (2.1.4\text{-}9)$$

and the final form is :

$$\rho_1(t,q)=\frac{E_T^2}{2}\rho_0\left(\frac{\partial\varepsilon}{\partial\rho}\right)_T\left[\frac{1}{c_T^2}-\frac{(\gamma-1)e^{-q^2D_Tt}}{\gamma c_T^2}\right]-\frac{E_T^2}{2}\frac{\beta_T\alpha_d c\varepsilon}{nC_V}\frac{\left(1-e^{-q^2D_Tt}\right)}{\gamma D_T q^2} \qquad (2.1.4\text{-}10)$$

This solution is valid for $t > 0$ and the first bracketed term on the right hand side is the formation of the electrostrictive grating to its steady state value, while the last term is the thermal grating formation. The solution may be further simplified by explicitly writing out the thermal diffusivity and the velocity of sound;

$c_T^2=1/\rho_0\kappa_T$, $\gamma=C_P/C_V$, and $D_T=\lambda_T/\rho_0 C_P$ with λ_T being the thermal

conductivity and κ_T being the isothermal compressibility.

$$\rho_1(t,q)=\frac{E_T^2}{2}\rho_0^2\kappa_T\left(\frac{\partial\varepsilon}{\partial\rho}\right)_T\left(1-\left(1-\frac{1}{\gamma}\right)e^{-q^2D_Tt}\right)-\frac{E_T^2}{2}\frac{\beta_T\alpha_d c\varepsilon}{n\lambda_T q^2}\left(1-e^{-q^2D_Tt}\right) \qquad (2.1.4\text{-}11)$$

is the solution for the DFWM electrostrictive and thermal gratings formed by the appliciation of a CW laser interference pattern starting at $t=0$ with no initial perturbations. The discrepancy of the electrostrictive response at $t=0$, i.e. the response does not start from zero at $t=0$, is due to the acostic modes which were thrown away in the approximations. Equation (2.1.4-11), after including the acoustic modes, has a causal response. The grating response time is now seen to be a function of the grating wavevector and the thermal diffusivity. Using the definitions above the thermal diffusivity depends on the thermal conductivity λ_T, the mass density ρ_0, and C_P the specific heat at constant pressure. At a slight distance away from the critical point, the mass density and the thermal conductivity change very little if at all. However, the specific heat does diverge as the critical point is approached. This causes the decay time for thermal modes to diverge as well. This "critical slowing down" controls the rate of formation of modes with grating spacing $2\pi/q$. Therefore, as the system approaches the critical point, the DFWM gratings take longer to form and decay. This was verified experimentally by observing the buildup time of stimulated scattering at 1.064 µm. The time constant for those gratings was on the order of 20 μsec.

This formulation can be generalized to arbitrary laser input, but the basic change in the DFWM reflectivity calculated in the previous section is the addition of a functional dependence which is an asymptotic exponential increase to the steady state value;

$$R_{pulsed}=R_{steady\,state}\left(1-e^{-q^2D_Tt_{laser}}\right). \qquad (2.1.4\text{-}12)$$

For laser pulses longer than the formation time of the grating the response is that calculated in steady state and can be quite large. If the laser pulse is much shorter than the fluid time constant, the response becomes independent of the thermodynamics to first order in the divergences. This is seen by assuming a short duration laser pulse and expanding the exponential;

$$R_{pulsed}=R_{steady\,state}\frac{q^2\lambda_T t_{laser}}{\rho_0 C_P} \qquad (2.1.4\text{-}13)$$

where the steady state reflectivity is proportional to κ_T. C_P and κ_T are nearly equal in their divergences and so the DFWM gain is roughly cancelled by the integration time of the fluid. This was seen in the eximer pumped dye laser DFWM experiments. In these experiements, it was noted that going closer to the critical point did not produce the expected increase in reflectivity which the static theory predicted. The static gain was reduced by a factor of close to 1000. In terms of the laser performance, the 100 kW peak power in the pulse was integrated by the fluid to be the equivalent of a 100 W CW laser. No real increase was seen and then the signal was lost in the noise of critical opalescence. This led to an experiment using the Nd:YAG laser whose pulse width was on the same order of duration as the fluid time constants and the effective peak power over the laser pulse was much larger than what had been available before.

In conclusion of this section the dynamics of the fluid enter into the DFWM reflectivity not only in the enhancement of the mechanical response, but also in the formation times of that response. A usable low power system must have a laser pulse which is at least comparable to the formation time of the grating to obtain the near critical point increase in the reflectivity.

2.1.5 The Signal to Noise Ratio in Degenerate Four Wave Mixing

Light scattering can be observed in fluids that are far from their critical points. In this case the fluid is relatively clear indicating that little light is scattered. The light scattering is caused by density fluctuations; but, since the characteristic size of the fluctuations is much less than wavelength of incident light, the scattering cross section is small.

Near the critical point, on the other hand, the size of the fluctuations can become large. When the size of the fluctuations approaches a wavelength the scattering coefficient becomes large and the fluid appears milky. This phenomenon is termed critical opalescence. The correlation length is the characteristic of the size of the fluctuations and it becomes large near the critical point.

It will be shown in the analysis to follow that, like the DFWM reflectivity, the intensity of the scattered light is proportional to κ_T. Since, near the critical point this is the dominant form of the noise, the signal to noise ratio is independent of κ_T if an optimum interaction length can be provided. However, in practice, the interaction length is typically non-optimal unless one is operating near the critical point. Thus, only near the critical point can the optimum interaction length and maximum signal to noise ratio be obtained.

We now proceed to illustrate these points in detail.

It is shown elsewhere [4], that for a single beam of intensity $I(x,y,z)$, the power scattered out of the beam by a volume element of material, dV, into angular area $\Delta\Omega$, is

$$dU_S = dVI(x,y,z)\frac{\pi^2 n^4 \kappa_T k_B T}{\lambda_0^4}\left(\frac{\rho}{\varepsilon_0}\frac{\partial\varepsilon}{\partial\rho}\right)^2 \int_{\Delta\Omega}\sin^2(\phi)d\Omega, \tag{2.1.5-1}$$

where k_B is Boltzman's constant, and ϕ is the angle between the wave vector of the scattered light and the direction of the electric field of the incident light. We assume a TEM_{00} transverse mode with spot size w_0 given most naturally when we write the amplitude A_i in the form (see Eq. [2.1.2-1])

$$A_i = a_i \exp\left(-\frac{x^2+y^2}{w_0^2} + i\phi_i\right), \quad \{a_i, \phi_i\} \in \Re.$$

Use of Eqs. (2.1.1-7), (2.1.5-1), and integration over the transverse dimensions x and y yields

$$\frac{dU_S}{dz} = I(z)\frac{\omega^4 n^4 \kappa_T k_B T D^2 w_0^2}{32\pi c^4 \varepsilon_0^2}\int_{\Delta\Omega}\sin^2(\phi)d\Omega. \tag{2.1.5-2}$$

Letting $U_i(z)$ be the incident power and performing the integral in Eq. (2.1.5-2) over $\Delta\Omega=4\pi$ gives an absorption coefficient due to scattering (α_S)

$$\frac{dU_S}{dz} = -\frac{\partial U_i}{\partial z} = \alpha_S U_i(z), \tag{2.1.5-3}$$

where

$$\alpha_S = \frac{\omega^4 r^2 K_T k_B T D^2}{6\pi c^4 \varepsilon_0^2}. \tag{2.1.5-4}$$

Implicit in Eqs. (2.1.5-3) and (2.1.5-4) is the assumption that the nonscattering portion of the absorption is small compared to scattering losses. This is typically the case when one is working with pure materials near their critical point.

Use of Eqs. (2.1.5-3) allows us to rewrite Eq. (2.1.5-2) in a more convenient form

$$\frac{dU_S}{dz} = \alpha_S I(z)\frac{3w_0^2}{16}\int_{\Delta\Omega}\sin^2(\phi)d\Omega. \tag{2.1.5-5}$$

Consider a single beam still, and a detector of area σ placed in the forward or backward scattering direction, a distance d from the scattering element, where d^3>> the scattering volume. The intensity present in the medium at a point z from z=0 is

$$I(z) = I_0 e^{-\alpha z}; \qquad (2.1.5\text{-}6)$$

hence, the power scattered from that beam into the detector is

$$U_\sigma = I_0\left(1 - e^{-\alpha L}\right)\frac{\alpha_S}{\alpha}\frac{3w_0^2}{16}\frac{\sigma}{d^2}. \qquad (2.1.5\text{-}7)$$

For a DFWM configuration in which the pump beams and the incident probe are of the same intensity, and the reflected signal is relatively weak (undepleted pump approximation), the total scattered power at the detector is three times that given in Eq. (2.1.5-7).

For DFWM, with a detector area that is large with respect to the incident beam area, Eqs. (2.1.2-6) and (2.1.5-7) can be used to solve for the signal to noise ratio (*SNR*),

$$SNR = \frac{2\pi}{9}\left[\frac{\omega D \kappa_T}{2n\varepsilon_0 c}(\Delta_P - \Delta_T) I_0\right]^2 \frac{1}{\alpha\alpha_S}\frac{d^2}{\sigma} e^{-\alpha L}\left(1 - e^{-\alpha L}\right). \qquad (2.1.5\text{-}8)$$

There are a number of qualitative deductions one can make by inspection of Eq. (2.1.5-8). Noting that both α_S, and therefore α, depend on κ_T, we see that very near the critical point the *SNR* is independent of κ_T, provided that αL is optimized. Also, the *SNR* is independent of spot size, and increases as the solid angle ($\approx\sigma/d^2$) subtended by the detector decreases.

In contrast to the discussion following Eq. (2.1.2-6), the *SNR*, in the near critical point case, is maximum when $\alpha L = \ln(2) \approx 0.7$. In Fig. 2.1.5-1 we show α_S^{-1} for some temperatures near the critical point, it can be seen that the cell length must be impractically large $\approx$100 m unless one is operating very near the critical point, where, as κ_T diverges, the optimum length approaches zero.

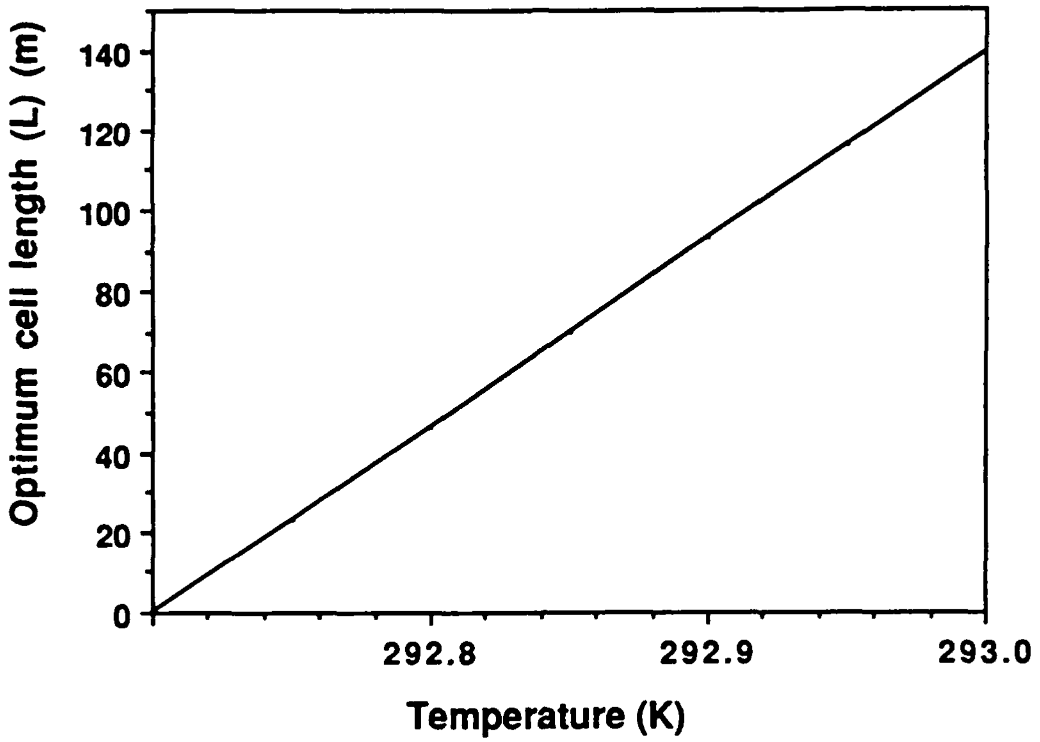

Fig. 2.1.5-1. Optimum interaction length (*L*) as a function of temperature near the critical point. Note that the optimum *L* is on the order of meters unless one approaches very close to T_C.

Let us now consider some limiting cases.

First, consider the case where there is negligible intrinsic absorption, then

$$SNR(\alpha_d \to 0) = \frac{8\pi^3}{n^{12}} \frac{I_0^2 c^4}{\omega^6 k_B^2 T^2} \frac{d^2}{\sigma} e^{-\alpha_s L}\left(1 - e^{-\alpha_s L}\right). \tag{2.1.5-9}$$

If *L* is chosen to satisfy αL=ln(2), then Eq. (2.1.5-9) shows that, under the conditions assumed in the analysis, *in theory the signal to noise ratio* is not *enhanced near the critical point for optimum L.* The *SNR* is increased at longer wavelengths, and for high pump intensity, while it is decreased with increased thermal noise.

In Fig. 2.1.5-2 we show a plot of the *SNR* obtained from Eq. (2.1.5-9) as a function of the interaction length and normalized to $I_0^2 \times 10^{-14}$, where I_0 is in W/m^2, σ=1 mm^2, λ=514 nm, d=10 cm, and r=1.037. It can be seen that the peaks are the same height but occur at different values of *L*; i.e. the peak height is independent of κ_T while the optimum interaction length does depend on κ_T.

It is important that in *practice L* is not optimum unless one is operating very near the critical point. In this sense, we can say that: *in practice, the SNR* is *enhanced near the critical point, since only near the critical point can the optimum L be obtained.* For example, it can be seen in Fig. 2.1.5-2 that at $T\text{-}T_c$=0.1 °K the optimum interaction length is ≈1 m, but if the interaction length is 1 cm we must get closer to the critical point for the *SNR* to be appreciable. To further emphasize this point: while an *SNR* of 10 can be obtained for $I_0 \approx 1\times10^3$ W/m^2=1 kW/cm^2 when L is optimized, we find that if L=1 mm and $T\text{-}T_c$=0.1 °K, I_0 must be ≈100 kW/cm^2 for an *SNR*=10.

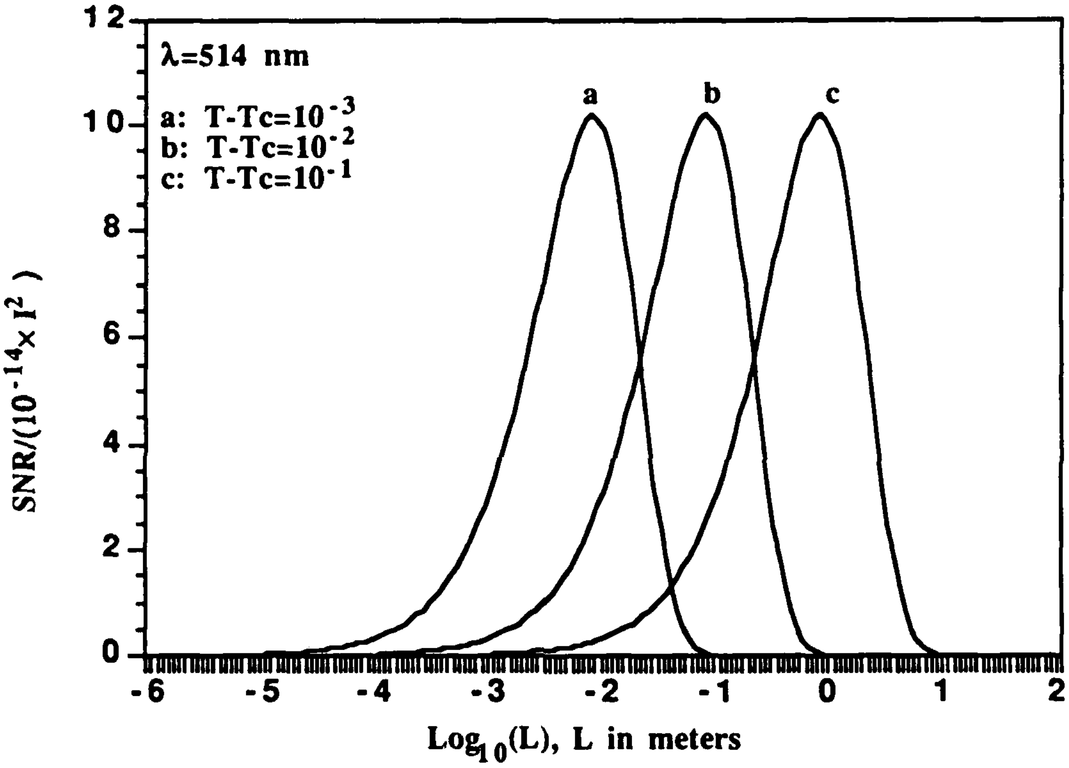

Fig. 2.1.5-2 The *SNR*, normalized to $10^{-14}\times I_0^2$ (where I_0 is in W/m^2) for three different temperatures near the critical point, and λ=514 nm.

In Fig. 2.1.5-3 we use the same numbers as in Fig. 2.1.5-2, except we use the single temperature of $T\text{-}T_c=10^{-1}$, and consider two wavelengths: 1.06 μm and 514 nm. Here the strong dependence of the peak *SNR* on wavelength is clearly shown; it results from the fact that the *SNR* is proportional to λ^6. Also a shift in position of the peaks with respect to L can be seen, and this results from the fact that α_s, which appears in the exponential cofactors, also depends on λ (see Eq. [2.1.5-9]).

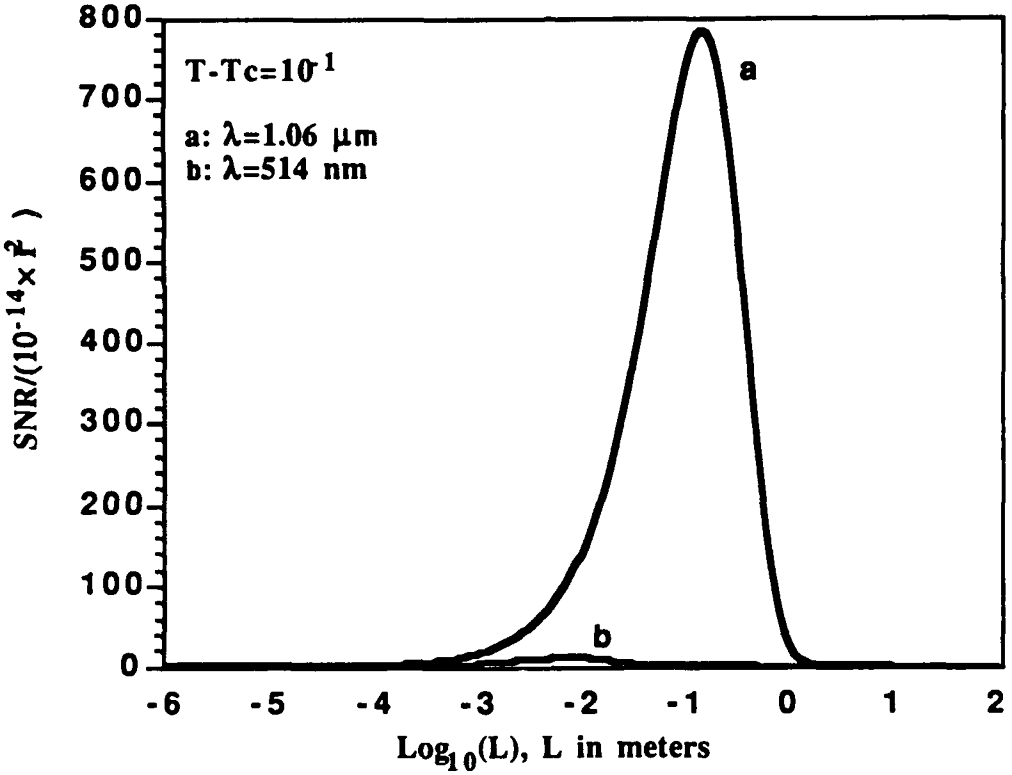

Fig. 2.1.5-3 The *SNR*, normalized to $10^{-14} \times I_0^2$ (where I_0 is in W/m^2) for two different wavelengths and T-T_c=0.1 °K.

Second, consider the case where thermal absorption dominates scattering losses. Note that this becomes impossible in principle if one is too close to the critical point—owing to the divergence in κ_T. However, in practice, κ_T is very sharply peaked, and temperature control is limited, and it is therefore not difficult to arrange for this case when α_d is made large. In this second case:

$$SNR(\alpha_d >> \alpha_S) = \frac{\pi^2}{96n^6} \frac{I_0^2 c^6 \alpha_d \kappa_T}{\lambda_T^2 \omega^6 k_B T} \left(\frac{\partial P}{\partial T} \right)_V^2 \frac{d^2}{\sigma} e^{-\alpha L} \left(1 - e^{-\alpha L} \right). \tag{2.1.5-10}$$

Although Eq. (2.1.5-10) suggests that the *SNR* for highly absorptive materials is enhanced near the critical point, a diverging κ_T is inconsistent with the condition: $\alpha_d >> \alpha_S$

2.2 Time Dependencies in Stimulated Electrostrictive Rayleigh Scattering

While DFWM facilitated analysis, and at first appeared promising as a mechanism for phase conjugation in NCPF, there is the considerable experimental difficulty in aligning the beams. Stimulated scattering, on the other hand, obviates this difficulty, since the return is naturally aligned with the input beam.

Appendix 2 is comprised of a paper that is to be submitted for publication to Optics Letters. This subsection contains the details of the work that lead to Eq. (10) of that paper. The other equations presented in Appendix 2 can be found in numerous references, most notably Refs. [9-11]. Appendix 2 also includes some discussion of the analysis together with comparison of several scattering processes and their strengths in transient and steady state cases.

Also, in Appendix 2, there is a discussion of the successful experimental results. Namely: strong (≈60%), low threshold (≈400 W), phase conjugate reflection of long pulse (≈20 μsec) Nd:YAG laser light was observed.

Following Kaiser and Maier [9], who follow Herman and Gray [10], we begin our analysis of stimulated scattering by writing the linearized hydrodynamic equations. The deviations from the average density (ρ_0), temperature (T_0) are denoted by $\delta\rho$ and δT, respectively. And, these deviations are in turn expressed in the following form:

$$\delta\rho = \frac{1}{2}\left[\rho \exp(ikz - i\omega t) + c.c.\right] \tag{2.2-1}$$

$$\delta T = \frac{1}{2}\left[T \exp(ikz - i\omega t) + c.c.\right] \tag{2.2-2}$$

where

$$\omega \equiv \omega_L - \omega_S$$

$$k \equiv k_L - k_S$$

and k_L (ω_L) and k_S (ω_S) are the wavevectors (frequencies) of the incident and scattered waves, respectively. Thus the electric field that is present can be written

$$E = \frac{1}{2}\left[E_L \exp(ik_L z - i\omega_L t) + E_S \exp(-ik_S z - i\omega_S t) + c.c.\right]. \tag{2.2-3}$$

Substitution of Eqs. (2.2-1)-(2.2-3) together with contraction (via substitution) of the three hydrodynamic equations to two equations results in [9]

$$\frac{\partial^2\rho}{\partial t^2}-(2i\omega-\Gamma_B)\frac{\partial\rho}{\partial t}-\left(\omega^2+i\omega\Gamma_B-\frac{v^2k^2}{\gamma}\right)\rho-2ik\frac{v^2}{\gamma}\frac{\partial\rho}{\partial z}+\frac{v^2\beta_T\rho_0k^2}{\gamma}T=\frac{Dk^2}{8\pi}E_LE_S^{*}, \tag{2.2-4}$$

and

$$\frac{\partial T}{\partial t}-\left(i\omega-\frac{1}{2}\gamma\Gamma_{RL}\right)T-\frac{\gamma-1}{\kappa_T\rho_0}\left(\frac{\partial\rho}{\partial t}-i\omega\rho\right)=\frac{1}{4\pi c_V\rho_0}\left[nc\alpha_d-\frac{1}{2}i\omega T_0\left(\frac{\partial\varepsilon}{\partial t}\right)_\rho\right]E_LE_S^{*}, \tag{2.2-5}$$

where

$$\Gamma_B\equiv\frac{\eta k^2}{\rho_0}, \tag{2.2-6}$$

$$\eta\equiv\frac{4}{3}\eta_S+\eta_B, \tag{2.2-7}$$

η_S and η_B are the shear and bulk viscosities

$$\Gamma_{RL}\equiv\frac{2\lambda_Tk^2}{\rho_0c_P}, \tag{2.2-8}$$

λ_T is the thermal conductivity, c_P is the specific heat at constant pressure

$$\gamma\equiv\frac{c_P}{c_V}, \tag{2.2-9}$$

c_V is the specific heat at constant volume, β_T is the coefficient of thermal expansion, and v is the velocity of sound. The quantities D and α_d have been defined elsewhere. Note that in this section we have used Gaussian units so that we can easily lead into Appendix 2, which, in turn, can be compared directly to the work of Ref. [11]. The reader should also be alerted to the fact that η used in this section is a viscosity, and is not the η defined in Eq. (2.1.2-5).

We define some notation and the Fourier transform variable through transformation of an arbitrary function $f(t)$

$$\tilde{f}(\Omega) \equiv FT\{f(t)\} \equiv \frac{1}{\sqrt{2\pi}} \int_{-\infty}^{+\infty} f(t) \exp(i\Omega t)\, dt, \tag{2.2-10}$$

and its inverse

$$f(t) \equiv FT^{-1}\{\tilde{f}(\Omega)\} \equiv \frac{1}{\sqrt{2\pi}} \int_{-\infty}^{+\infty} \tilde{f}(\Omega) \exp(-i\Omega t)\, d\Omega. \tag{2.2-11}$$

In the plane wave and slowly varying amplitude approximations, the wave equation describes the coupling between the medium and the thermodynamic variables

$$-\frac{\partial E_S}{\partial z} + \frac{n}{c}\frac{\partial E_S}{\partial t} + \frac{1}{2}\alpha_d E_S = \frac{i\omega_S}{4cn}\left[\frac{D}{\rho_0} E_L \rho^* + \left(\frac{\partial \varepsilon}{\partial T}\right)_\rho E_L T^*\right]. \tag{2.2-12}$$

Henceforth we will restrict consideration to the case: $\alpha_d = 0$, and neglect the small $\partial\varepsilon/\partial T$ terms. Thus, Eq. (2.2-12) becomes

$$-\frac{\partial E_S}{\partial z} + \frac{n}{c}\frac{\partial E_S}{\partial t} = \frac{i\omega_S D}{4cn\rho_0} E_L \rho^*. \tag{2.2-13}$$

Fourier transformation of Eq. (2.2-5) gives

$$\left(\frac{1}{2}\Gamma_{RL}\gamma - i\tilde{\Omega}\right) FT\{T^*\} = -i\tilde{\Omega}\frac{\gamma - 1}{\beta_T \rho_0} FT\{\rho^*\}, \tag{2.2-14}$$

where

$$\tilde{\Omega} \equiv \Omega - \omega. \tag{2.2-15}$$

We now assume that the incident wave is not depleted so that E_L is piecewise constant with respect to time. And, we use the ansatz

$$E_S \equiv e_S \exp(-i\psi_S), \quad \{e_S, \psi_S\} \in \Re. \tag{2.2-16}$$

We put Eq. (2.2-16) into Eq. (2.2-4), take $\rho(t)$ to be slow with respect to t, neglect Brillouin scattering, assume low gain, and seek solutions with zero frequency shift. A subsequent Fourier transformation gives

$$FT\{\rho^*\} = \frac{DE_L^*}{8\pi v^2} \frac{\frac{1}{2}\gamma\Gamma_{RL} - i\Omega}{\frac{1}{2}\Gamma_{RL} - i\Omega} FT\{e_S \exp(i\psi_S)\}. \tag{2.2-17}$$

Substitution of Eqs. (2.2-17) and (2.2-16) into Eq. (2.2-13) gives

$$\left(\frac{\partial e_S}{\partial \xi}+i\frac{\partial \psi_S}{\partial \xi}e_S\right)\exp(i\psi_S)=-\frac{i\omega_S D^2 E_L^* E_L}{32\pi c n \rho_0 v^2}FT^{-1}\left\{FT\{e_S\exp(i\psi_S)\}\left(\frac{\frac{1}{2}\gamma\Gamma_{RL}-i\Omega}{\frac{1}{2}\Gamma_{RL}-i\Omega}\right)\right\},\tag{2.2-18}$$

where we have transformed to the coordinates comoving with the beam

$$\xi \equiv z, \quad \eta \equiv t + zn/c.$$

Note now that

$$FT^{-1}\left\{\tilde{f}(\Omega)\tilde{g}(\Omega)\right\}=\frac{1}{\sqrt{2\pi}}\int_{-\infty}^{+\infty}f(t-\tau)g(\tau)d\tau,\tag{2.2-19}$$

which is of the same form as the right hand side of Eq. (2.2-18). We can use a contour integration in the complex Ω plane to find that

$$FT^{-1}\left\{\frac{\frac{1}{2}\gamma\Gamma_{RL}-i\Omega}{\frac{1}{2}\Gamma_{RL}-i\Omega}\right\}=\sqrt{2\pi}\frac{1}{2}\Gamma_{RL}(\gamma-1)\exp\left(-\frac{1}{2}\Gamma_{RL}t\right).\tag{2.2-20}$$

Using Eqs. (2.2-19) and (2.2-20) in Eq. (2.2-18) we obtain

$$\left(\frac{\partial e_S}{\partial \xi}+i\frac{\partial \psi_S}{\partial \xi}e_S\right)\exp(i\psi_S)=-\frac{i\omega_S D^2 E_L^* E_L}{32\pi c n \rho_0 v^2}\frac{1}{2}\Gamma_{RL}\int_{-\infty}^{+\infty}e_S(\tau)\exp\left[-i\psi_S(\tau)-\frac{1}{2}\Gamma_{RL}(t-\tau)\right].\tag{2.2-21}$$

To get an approximation for the initial time development we take

$$e_S(\tau)\exp[-i\psi_S(\tau)]\approx e_S(0)\exp[-i\psi_S(0)],$$

together with $e_S(t<0)=0$. Then we perform the indicated integration, again use the small gain approximation and finally get

$$\psi_S(\xi)=\frac{\omega_S D^2 E_L^* E_L}{32\pi c n \rho_0 v^2}\left[1-\exp\left(-\frac{1}{2}\Gamma_{RL}t\right)\right]+\Psi.\tag{2.2-22}$$

where the quantity Ψ is the implied steady state phase shift.

Equation (2.2-22) is the original analytical result that is used in the Appendix 2, which consist of a paper that was submitted to Optics Letters. This Optics Letter also includes the comparisons of various stimulated processes; their gains and time constants, as well as a discussion and presentation of the significant experimental results that were obtained near the end of this program.

References

1) F. W. Sears and G. L. Salinger, *Thermodynamics, Kinetic Theory, and Statistical Thermodynamics* (Addison-Wesley, Reading, Massachusetts, 1975).

2) M. Schubert and B. Wilhelmi, *Nonlinear Optics and Quantum Electronics* (Wiley, New York, 1986).

3) R. W. Hellwarth, "Minimum power requirements for efficient four-wave mixing and self focusing of electromagnetic beams in glasses and fluids," Phys. Rev. **A31**, 533-536, (1985).

4) I. L. Fabelinskii, *Molecular Scattering of Light* (Plenum Press, New York, 1968).

5) B. J. Berne and R. Pecora, *Dynamic Light Scattering* (Wiley & Sons, New York, 1976).

6) H. E. Stanley, *Introduction to Phase Transitions and Critical Phenomena* (Oxford University Press, New York, 1971).

7) M. Fixman, "Density correlations, critical opalescence, and the free energy in nonuniform fluids," J. Chem. Phys. **33**, 1357 (1960).

8) M. R. Moldover, "Interfacial tension of fluids near critical points and two-scale-factor universality," Phys. Rev. **A31**, 1022 (1985).

9) W. Kaiser and M. Maier, *Laser Handbook*, edited by F. T. Arrechi E. O. Schilz-DuBois, (North Holland, New York, 1972).

10) R. M. Herman and M. A. Gray, Phys. Rev. Lett. **19**, 824 (1967).

11) W. Rother, D. Pohl and W. Kaiser, Phys. Rev. Lett. **22**, 915 (1969).

2.3 Two-phase Response (in flowing media) Through Liquid Nucleation and the Degree of Superheating

Phase transformations are considered to proceed discontinuously through the birth and subsequent growth of small nuclei of the new material phase. In the absence of nucleation sites, these nuclei appear at random throughout the original phase, and the nucleation is termed homogenous. Bubbles are formed as density fluctuations occur in the liquid. From visual observation and heat capacity measurements, it is observed that simple fluids can be superheated more than expected on the basis of classical nucleation theory. In its simple form, this theory predicts that the steady-state rate of formation of vapor nuclei J, at which bubbles of a new phase nucleate out of the parent phase is given by [2.3.1]

$$J = 3.73 \text{ x } 10^{35} \left(\frac{\rho_l^2 \gamma}{M^3 B} \right)^{1/2} e^{-\left(\frac{1.182 x 10^5}{T(\eta P_{\infty} - P_0)^{1/2}} \gamma^3 \right)} \tag{2.3-1}$$

where J has units of #/cm^{3}s, , P_{∞}, atm; P_O, atm; T, °K; q, erg/cm^2; p_P, g/cm^3; M, g/mole. Also B=1 for cavitation and approximately 2/3 otherwise. The factor η is defined as

$$\eta = exp \left[\frac{V_l (P_0 - P_{\infty})}{R T_l} \right] \tag{2.3-2}$$

where V_P is specific volume of the liquid. P_{∞} and P_O are the pressures corresponding to the liquid superheated temperature T_{∞} and the saturation temperature T_s, respectively.

The physical implications of Eq. (2.3-1) can be examined as follows: the preexponential terms vary slowly with temperature. However, any temperature change inside the exponential will have a very strong effect on the rate of nucleation. Consider nucleation at an ambient pressure P_c of 1 atm. One observes experimentally that the nucleation occurs at about 0.89 T_c. Using the values for surface tension, vapor pressure; density and molecular weight into (2.3-1), one finds that at 0.89 T_c, the predicted rate of nucleation is about 10^6 bubbles/cm^3 sec, and that the rate changes about three to four orders of magnitude per degree C. The major reason for this extreme sensitivity to temperature is that, so close to the critical temperature, the exponential is of the order of 10^{-30} and the fractional change in the magnitude of the surface tension is very large per degree. For example, increasing T by 1 degree, decreases γ by about 7 to 9% [2.3-2.2,3-3]. In addition to this, the denominator of the exponent contains T and $(\eta P_{\infty} - P_O)^2$, both of which increase with increasing temperature; the vapor pressure ηP_∞ especially so. Thus these factors also decrease the argument of the exponent.

Knowing the values of J, Eq. (2.3-1) may be used to determine the kinetic limit of superheating. Rearranging (2.3-1) gives

$$\eta \; P_\infty - P_0 = \frac{1.182 \times 10^5 \; \gamma^3}{T \; \ln\left[\left(\frac{3.73 \times 10^{35}}{J}\right)\frac{P_l^2 \gamma^{1/2}}{M^3 B}\right]} \qquad (2.6\text{-}3)$$

Thermodynamic tables will yield the desired superheat temperature, T_∞, as a function of the superheat pressure, P_∞, and the saturation temperature, T_s, as a function of the saturation pressure, P_0. The validity of Eq. (2.3-3) has been experimentally verified for a large number of organic liquids [2.3.1].

In the following sections we will estimate the superheating limit using Eq. (2.3-3) for Xenon, (Xe), hexafluoroethane, (C_2F_6); and chlorotrifluoromethane ($CCLF_3$). The physical properties of Xe, C_2F_6 and $CClF_3$ are listed in Table 2.3-3.

TABLE 2.3-3. PHYSICAL PROPERTIES OF Xe, C_2F_6 and $CClF_3$

Material	M (g/mole)	T_c (K)	P_c (atm)	P_c (kg/m^3)	q (erg/cm^2)
Xe	131.1	289.95	58	986	18.7(T=-110°C)
C_2F_6	138.02	292.2	29.8	608	16 (at T=-73°C)
$CClF_3$	104.458	302.1	38.2	581	17 (at T=-73°C)

The surface tensions required in using Eq. (2.3-3) can be estimated based on the corresponding-state correlation proposed by Brock and Bird [2.3.4]

$$\gamma = P_c^{2/3} T_c^{1/3} (0.133\alpha_c - 0.281)(1 - T_r)^{11/9} \qquad (2.3\text{-}4)$$

T_r is the reduced temperature, α_c the Riedel factor [2.6.4] and P_c and T_c are the critical pressure and temperature in atmospheres and degrees Kelvin. Eq. (2.3-4) has been correlated to surface tensions of 84 widely different nonpolar organic compounds and permanent gases with an average deviation of about 3 percent.

Using Eqs (2.3-3) and (2.3-4), the liquid superheat limit, T_∞, of Xe, C_2F_6 and $CClF_3$ at one atmosphere pressure were calculated and the results are summarized in Table 2.3-4. Also included in Table 4 are the saturation temperature T_s, liquid and gas densities p_p and p_V, and the surface tension, α.

The results of Table 2.3-4 were obtained for one atmosphere of pressure. For pressures other than one atmosphere, we estimated the superheat limits based on the correlations obtained experimentally by Blander and Katz[2.3.2] as shown in Fig. 2.3-1. The results are summarized in Tables 2.3-5, 6 and 7 for Xe, C_2F_6 and $CClF_3$ where the degree of superheating T_∞/T_c shown as

function of

TABLE 2.3-4. THERMODYNAMIC PROPERTIES OF Xe, C_2F_6 and $CClF_3$

Material	P (atm)	T_s (K)	P_p (kg/m^3)	P_v (kg/m^3)	α (erg/cm^2)	P_∞ (atm)	T_∞ (K)
Xe	1	161.35	3057	9.86	3.30	29.3	258.06
C_2F_6	1	194.95	1608	8.86	2.51	13.4	261
$CClF_3$	1	191.65	1526	6.94	4.29	28.5	268.9

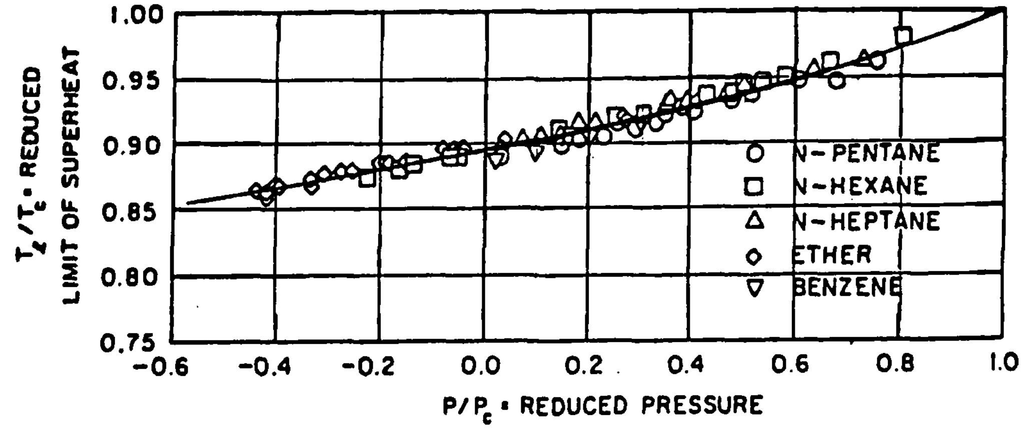

Fig. 2.3-1. Experimental Correlations of Superheat Limit [2.3-1]

pressure. These results indicate that a liquid can be superheated substantially without the occurence of a phase transformation even though its state is such that it lies within the two-phase envelope. Under these conditions, the external isotherm must extend into the stable two phase region. Here the fluid is clearly not in its most stable condition, i.e., a mixture of saturated liquid and saturated vapor; nor is it mechanically unstable as long as the slope of the isotherm remains positive. This condition is commonly called metastable.

It also can be seen from Tables 2.3-5, 6 and 7 that the superheating or metastable limit decreases with increasing pressure. This implies that the limit can be achieved easier when the fluid is heated or expanded at higher pressures than that at low pressures.

TABLE 2.3-5. ESTIMATED SUPERHEATING LIMITS OF Xe
AS A FUNCTION OF PRESSURE

P (atm)	P_r	T_∞ / T_c	T_s (K)	T_∞ (K)
1	0.01724	0.89	161.35	258.06
2	0.03448	0.90	178.20	260.96
5	0.0862	0.905	198.70	263.85
10	0.172	0.910	218.20	263.85
15	0.259	0.915	232.20	265.30
20	0.3448	0.925	243.20	268.20
30	0.517	0.935	258.20	271.10
40	0.689	0.960	270.20	278.35

TABLE 2.3-6. ESTIMATED SUPERHEATING LIMITS OF C_2F_6
AS A FUNCTION OF PRESSURE

P (atm)	P_r	T_∞ / T_C	T_S (K)	T_∞ (K)
1	0.034	0.89	194.95	261.0
2	0.067	0.90	209.20	263.6
5	0.168	0.91	230.20	266.5
10	0.336	0.92	251.20	269.5
15	0.503	0.93	265.20	273.3
20	0.671	0.96	276.20	279.7
25	0.839	0.975	284.20	285.6

TABLE 2.3-7. ESTIMATED SUPERHEATING LIMITS OF $CClF_3$
AS A FUNCTION OF PRESSURE

P (atm)	P_r	T_∞ / T_C	T_S (K)	T_∞ (K)
1	0.0262	0.89	191.65	268.9
2	0.0524	0.90	207.20	271.9
5	0.131	0.905	228.2	273.42
10	0.262	0.915	248.20	276.44
15	0.393	0.925	263.20	279.44
20	0.524	0.940	273.20	283.97
30	0.785	0.97	290.20	293.04
40	0.916	0.98	298.20	296.06

nucleation. The pressure reduction process can be easily obtained by using a convergent nozzle. Since T_∞/T_c is smaller at high pressures or near critical points, one would prefer to generate bubbles at high pressures where the pressure change required, or the input area to nozzle throat area ratio required, for nucleation would be smaller than is required at low pressure nucleation.

References

[2.3.1] Robert Cole "Homogenuous and Heterogeneous nucleation", Chapter 3, pp 77, Boiling Phenomena edited by Sjoerd Van Stralen and Robert Cole, Hemisphere Publishing Corporation, 1979, New York.

[2.3.2] M.Blander and J. L. Katz, "Bubble Nucleation in Liquids", Aiche Journal, Vol. 21, No. 5, 1975, pp 833

[2.3.3] W. Porteous and M. Blander, "Limits of Superheat and Explosive Boiling of Light Hydrocarbons, Halocarbons, and Hydrocarbon-Mixtures", Aiche Journal, Vol. 21, No. 3, 1975, pp 560

[2.3.4] R. G Reid and T. K. Sherwood, "The Properties of Gases and Liquids, pp 371, McGraw-Hill Book Co., New York (1961).

SECTION 3

EXPERIMENTAL FINDINGS

3.1 NCP Materials Selection

Table 3.1-1 lists a large number of fluids whose critical points are given in the literature. The fluids have been sorted by temperature in order to readily identify those whose critical points are near room temperature. Such fluids are of particular interest since their useage reduces the technical difficulties associated with thermal control and avoids adverse effects due to severe thermal gradients on the optics. For these reasons, many fluids whose critical temperatures fall outside the range of zero to one hundred degrees centigrade have been omitted from the table.

The right hand column of the table identifies safety issues associated with the various fluids. The capital letters: E, F, I, N, and T identify explosive, flammable, irritant, narcotic, and toxic hazards, respectively. The small letters: h, s, and w are modifiers indicating highly, slighlty, or weakly. An asterisk (*) designates a relatively benign substance whose only hazards are those associated with the high pressure at the critical point, the displacement of breathable air in case of a vapor release, and any cryogenic fluid that may be produced as a result of a vapor release.

Arrows in the right hand margin of the table indicate fluids that we are considering for use as a phase conjugating medium. The length of the arrow corresponds to the level of our interest in the particular substance.

3.1.1 Primary and Secondary Material Choices

We have selected five fluids for study as phase transition non-linear media. These five materials and their properties are listed in Table 3.1.1-1. The chosen fluids include the four benign fluids that have their critical point in the immediate vicinity of room temperature plus sulfur hexafluoride, a benign fluid that is critical at a hotter, though still safe, temperature. Our primary choice among these five fluids is hexafluoroethane (Freon 116), since it has the lowest critical pressure and is incidently one of the two least expensive of the five,(at about $60 per critical point gallon). Damzen et al. [1] reported on the stimulated brillouin scattering (SBS) properties of four of these five fluids: chlorotrifluoromethane (Freon 13), hexafluoroethane (Freon 116), sulfur hexafluoride, and xenon. Although the bulk of the technical effort emphasizes degenerate four wave mixing (DFWM) over

TABLE 3.1-1 CRITICAL FLUIDS SORTED BY TEMPERATURE

Material	Freon #	Formula	Critical Temperature (C)	Critical Pressure (atm)	Safety
nitrogen		N_2	-146.8	33.5	*
carbon monoxide		CO	-140	34.5	F hT
argon		Ar	-122	48	*
methane		CH_4	-82.3	45.8	F
krypton		Kr	-63.6	54.3	*
tetrafluoromethane	14	CF_4	-45.45	37.43	*
boron trifluoride		BF_3	-12.26	49.2	T
ethylene		C_2H_4	9.91	50.5	F wN <--
carbonyl fluoride		CF_2O	14.7	33.52	hT
xenon		Xe	16.75	58	* <--<<
hexafluoroethane	116	C_2F_6	19.7	29.8	* <-----<<
trifluoromethane	23	CHF_3	25.6	48.37	* <--<<
chlorotrifluoromethane	13	$CClF_3$	28.9	38.2	* <--<<
difluoroethylene	1132a	$C_2H_2F_2$	29.70	44.63	F sT <--
carbon dioxide		CO_2	31	72.9	T
ethane		C_2H_6	32.4	48.2	F
tetrafluoroethylene		C_2F_4	33.3	40.50	E F sT
acetylene		C_2H_2	35.5	61.6	hF N
fluoromethane		CH_3F	44.55	58.74	F
sulfur hexafluoride		F_6	45.7	37.1	* <--<<
bromotrifluoromethane	13B1	$CBrF_3$	67	39.1	*
perfluoropropane		C_3F_8	71.9	26.80	* <--
difluoromethane32		CH_2F_2	78.4	58.30	?F sT
chloropentaF-ethane	115	C_2ClF_5	80.2	31.6	*
hexafluoroacetone		C_3F_6O	84.1	28.41	I T
propene		C_3H_6	92.1	45.4	F sN
chlorodifluoromethane	22	$CHClF_2$	96	49.1	*
propane		C_3H_8	96.9	42	F N
dichlorodiF-methane	12	CCl_2F_2	112	40.6	*
perfluorobutane	610	C_4F_{10}	113.3	24.27	* <--
perfluorocyclobutane	C318	C_4F_8	115.22	27.77	*
propadiene		C_3H_4	120	43.6	F sN
propyne		C_3H_4	128	52.8	F N
ammonia		NH_3	132.5	112.5	hT
dichlorotetraF-ethane	114	$C_2Cl_2F_4$	145.7	32.62	*
n-butane		C_4H_{10}	152	37.5	F N
n-butene		C_4H_8	155.6	40.5	F sT
methylamine		CH_5N	156.9	40.2	F I T
neo-pentane		C_5H_{12}	160.6	31.6	F N
dichlorofluoromethane	21	$CHCl_2F$	178.5	51	sT
boron trichloride		BCl_3	178.8	38.2	T
fluorinert liquids	Mol.Wt.	340 to 971	178 to 373	18 to 9	* <--
trichlorofluoromethane	11	CCl_3F	198	43.5	*
acetone		C_3H_6O	235.5	47	F T
fluorobenzene		C_6H_5F	287	44.6	F T
benzene		C_6H_6	288.9	48.6	F T

Table 3.1.1-1 PROPERTIES OF
PRIMARY AND SECONDARY MATERIALS

Material	hexafluoro-ethane	trifluoro-methane	trifluorochloro-methane	sulfur-hexafluoride	xenon
Freon #	116	23	13	N/A	N/A
Formula	C_2F_6	CHF_3	$CClF_3$	$S\ F_6$	Xe
Cost $/gal	$60	$84	$82	$40	$6850
T_c (C/F)	19.7 / 67	25.6 / 78	28.9 / 84	45.7 / 114	16.75 / 62
P_c (atm/psi)	29.4 / 432	7.7 / 701	38.2 / 561	37.1 / 546	58 / 853
ρ_c (g/cm^3)	0.608	0.516	0.581	0.735	1.110
n @ T_c	1.08	1.16	1.09	1.12	1.19
at.wt. g/mole	138.01	70.014	104.46	146.05	131.1

stimulated scattering processes, these four fluids offered some variety in their chemical makeup and therefore may have been of interest in evaluating the effects of molecular form upon nonlinear response. Freon 116 was the only fulid which we did test because our subsequent analysis showed that the response at optimum interaction length is only weakly dependent on the choice of material. One of our fluids, trifluoromethane (Freon 23), was not tested by Damzen et al. As a result of its fairly high critical pressure and low molecular weight, we expected it to have a higher index of refraction than the other two freons; the index should be midway between those expected for xenon and sulfur hexafluoride. We have flagged our primary material choice with the longest arrow in Table 3.1-1 and have flagged the four secondary material choices with medium length arrows.

3.1.2 Tertiary Material Choices

Five other fluids are flagged with short arrows to indicate that, although they have some interesting characteristics, they also have some adverse properties that limited our interest in them. Ethylene and difluoroethylene (Freon 1132a) each have a double bond and therefore can be expected to have a high polarizability. However, they are both flammable. Dupont claims that Freon 1132a is slightly toxic and therefore declines to offer it for sale; on the other hand, Union Carbide lists flammability as its only hazard in their catalog. Perfluoropropane and perfluorobutane are interestingbecause they have relatively low critical pressures, although their critical temperatures of 71.9 and 113.3 degrees centigrade are significantly above room temperature. For perfluorobutane, this may offer some safety advantages, since its vapor pressure is 3 to 4 atmospheres at 30 to 40 degrees centigrade; thus the phase conjugating apparatus can be safely filled with the liquified gas under pressure (only 30 to 45 psi above ambient) at room temperature and then be heated to achieve the appropriate temperature and pressure when needed. In other words, it offers a safety trade-off by being a lesser hazard while in storage and fill situations, while being a twin hazard (temperature and pressure) under operating conditions, as opposed to room temperature critical materials that are pressure hazards all of the time.

The last fluid entry in the table flagged by a short arrow is the "fluorinert liquids". These are high molecular weight, fully fluorinated carbon chains that have the notable advantages of being liquids at room temperature at one atmosphere pressure, of having low critical pressures (as low as 9 atmospheres for the highest molecular weight fluid), and of having a sound velocity at the critical point that is about half that of freon 116 for the heaviest molecular weight fluid, which would be an advantage since it results in a lower SBS redshift as compared to Freon 116. The fluid can be poured as an open air liquid into the fluid apparatus, then heated to the critical temperature while expanding a piston accumulator against nitrogen pressurized at the fluid's critical pressure. To shut down the experiment, simply disconnect the power to the heater and release the nitrogen pressure; the apparatus will then safely cool off to room temperature and pressure. However, the advantanges of these fluids are not strong enough to overcome the technical difficulties of working at their high critical temperatures, particularly if the use of DFWM rather than SBS is preferred as a phase conjugating process.

Since Freon 116 has been chosen as the preferred fluid in our static and flowing experiments, a visible and IR transmission scan was performed from 0.2 µm to 3 µm to determine what range of wavelength s would be suitable for potential operation. A 4 cm cell was used with 200 psig of Freon 116 in the scan shown in Figure 3.1.2-1. Within the error of the Beckman spectraphotometer, the material is nonabsorbing at 514 nm and 1.064 µm.

In conclusion, we selected hexafluoroethane (Freon 116) as our preferred fluid due to considerations of safe material properties, near room temperature critical point, and comparatively low critical pressure. As secondary fluids, we have identified Freon 13, Freon 23, sulfur hexafluoride and xenon as giving a variety of chemical form while having reasonably safe and convenient fluid properties.

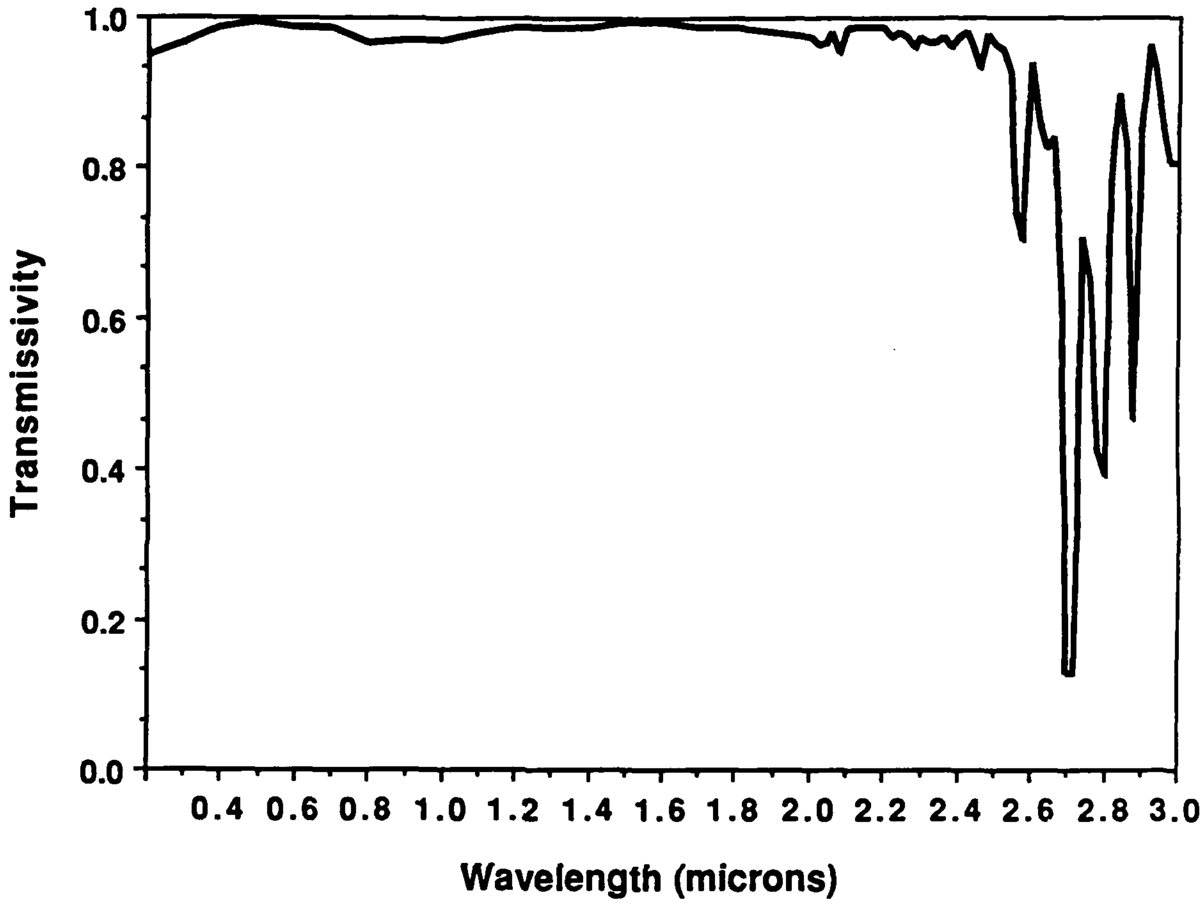

Fig. 3.1.2-1 Transmission scan of Freon 116.

3.2 Fabrication of Test Apparatus

The expected enhancement of nonlinear response can only be achieved by maintaining the media near a region in PVT space where the compressibility of the medium diverges. There, an optically induced electrostriction can exert pressure perturbations that in turn induce disproportionatly large changes in the thermodynamic and optical density. Figure 3.2-1 shows a typical pressure-volume diagram of a fluid in the liquid, gas and liquid-gas transition region. The dome shaped region represents the region of co-existance of both liquid and gas defined by the Maxwell construction which equates the Gibb's free energy of changing from a liquid to a gas and visa versa. The fluid is a pure liquid to the left of the dome and a pure gas to the right of the dome.

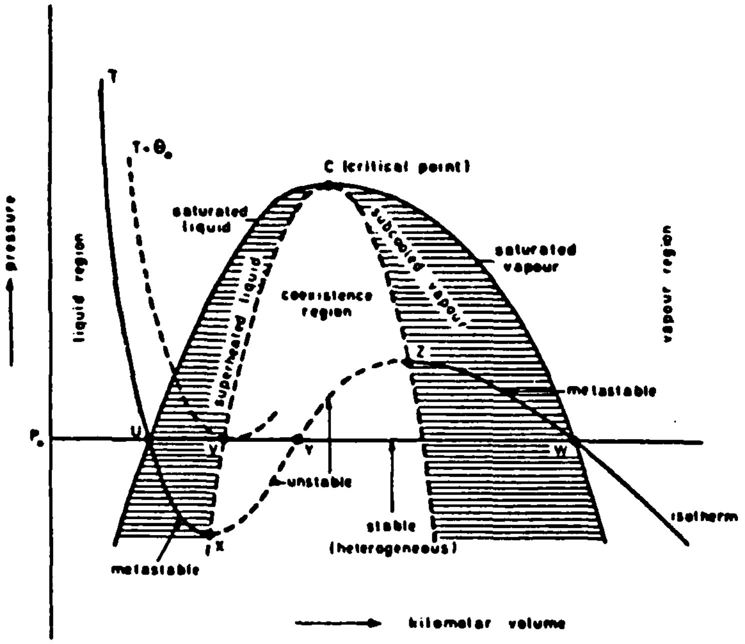

Figure 3.2-1 Pressure-volume diagram of a typical fluid showing the critical point, the two phase, and the metastqable regions (shaded in grey).

In a true equilibrium condition ; ie. "in the dome", the fluid exists as a combination of liquid and gas, whose densities are determined by the two points where a line of constant pressure intersects the dome. In equilibrium, isotherms are horizontal within the dome. This is equivalent to an infinite static, zero frequency, compressibility within the dome. However, this compressibility is not useful as an enhancement to the DFWM gain because there is no way to tap into the stored energy in the phase transition to create a grating at equilibrium. A closer look at the inside of the dome in a nonequilibrium condition shows us that there is a possibility for enhancement that is even greater than that found at the critical point.

The point at the top of the dome is called the critical point. This is the point at which the distinction between liquid and gas no longer exists. For example, the liquid miniscus disappears at this point and critical opalescence occurs. This point is also the only region of PVT space outside the dome in which a isotherm approaches horizontal.

We identify two regions that can be considered for our experiments - the critical point or very near it, and the nonequilibrium region inside the dome (i.e., inside the co-existance line). In these two regions, the fluid can exhibit a diverging compressibility and can be considered for zn enhanced electrostrictive index modulation. This assumption of using the diverging compressibility assumes that the time constants for application of the optical fields are long enough that the compression can be considered static as was shown in Section 2.1.5 for the near critical point operation. However, the metastble region in the dome may not have the same dynamics so we are not able to predict what the correct time constants are for operation in the dome.

A major program objective was to construct a means to explore the region inside the dome using a flowing system with a nozzle. This two phase region inside the dome is interesting for several reasons, but mainly because of the variation in fluid responses that can be found there. The spinodial line represents the region of diverging isothermal compressibility and separates the central thermodynamically unstable region from the metastable regions, which are shaded. The shaded region in Figure 3.2-1 between the co-existance curve and the spinodial line represents the metastable region where phase transition occurs dependent upon nucleation. This region is mechanically stable yet unstable to heat flows; therefore, nonequilibrium conditions may exhibit considerable lifetimes. The shaded region to the left is also metastable and is variously referred to as the region of nucleate boiling, superheat, or cavitation. In this region, for a clean fluid, a nucleation site is usually necessary for a bubble to form. This is the regionof operation for the bubble chamber in experimental particle physics. The shaded region to the right side of the dome is referred to as the region of supersaturated condensation. This region is used in a cloud chamber. The spinodial region in the center of the dome is spontaneously unstable to perturbations and poses a difficult problem; we will not consider it further.

We are left with two choices for operation in the metastable region: - the left side, where the fluid is a liquid undergoing bubble formation; or the right side, where the fluid is a gas undergoing droplet condensation. Early in the program, a somewhat *arbitrary* choice was made to operate on the liquid side of the curve. Here, there is the advantage of higher density in a liquid. However, if operation is near the top of the co-existance curve; i.e. near the critical point, this distinction becomes small. There are also arguements in favor of operating on the vapor side of the co-existance curve, and this issue remains open for exploration.

The issue of nucleation in the metastable region requires that the apparatus provide transient nonequilibrium conditions. Nucleation is both a problem and a potential enhancement. If the fluid spontaneously transitioned from one state to another as soon as the co-existance curve was crossed, it could be expected that the fluid would maintain a very nearly homogeneous density. If a nearly infinitely fine cloud of bubbles or droplets were formed, so that the bubbles or droplets were much smaller than the wavelength of light, the loss from Mie or Rayleigh scattering of light would be small. However, since nucleation in the metastable region tends to precipitate upon relatively few sites (in the absence of seeding), nucleation will tend to result in the formation of a relatively few bubbles. Once formed, these bubbles will rapidly grow to large size since the fluid is in a metastable region and the equilibrium condition is to convert completely to vapor. This would be unsuitable for optical applications since optical scattering increases as the fourth power of diameter.

Nucleation is a potential advantage because the metastable region provides for the growth of any initial pertubations that exceed the critical minimum size for a proto-bubble. Thus, an incident optical field of sufficient strength to overcome thermal noise creates a standing wave electrostrictive pressure modulation, which in term modulates the spontaneous nucleation rate of bubbles so that bubbles are preferentially nucleated and grown in the nodes of the standing wave field. As the state of the fluid is moved further from the critical point, the difference in refractive index between a liquid and a vapor bubble increases, increasing the modulation in average optical index of the fluid. In addition, the spontaneous nucleation rate becomes more sensitive to the pressure and temperature, and the growth rate of the bubbles increases. The growth of the bubbles requires energy, which is provided for by the thermodynamic excess free energy that is inherent in the metastable state. The pumping station adds the energy to the fluid and the nozzle causes the fluid to then find itself in a nonequilibrium state. Thus, it is possible that the laser merely triggers the growth of the grating, whose further development utilizes energy that was injected into fluid through the pump. The result is an expectation of greater response, higher refractive index modulation, and higher phase conjugate reflectivity per input laser power from the flowing system as compared with the static NCP cell.

In summary, use of a nozzle allows control of nucleation rate and bubble size through a choice of the PVT and velocity parameters. In addition, amplification of nonlinear response should increase as the distance from the critical point is increased, at the expense of a need for more critical temperature control.

3.2.1 Flowing Cell

The originally proposed flowing system consisted of a nozzle with a simple blowdown system using a high pressure freon reservoir and a low pressure recovery tank. The analysis of spontaneous nucleation rates performed in Section 2.3 indicated that temperature control was very important to the proper performance of the phase transition media. In order to increase the likelihood that the media would be at the proper conditions of pressure and temperature when the laser was operating, a decision was made to change the design to a fully recirculating system that could operate on a continuous basis. This would allow more time to tune the fluid to the correct operating conditions, and stabilize the temperature under flowing conditions. This presumably would increase the amount of running time for the experiment, where the laser, optics and fluid system would all be operational. The nozzle design was independent of this decision and its design and fabrication preceded the fabrication of the recirculation system.

3.2.1.1 Nozzle Design

The design of the nozzle is illustrated in Figure 3.2.1.1-1. A simple convergent-divergent nozzle allows operation on the liquid side of the two-phase region. The nozzle is formed by a two-dimensional throat with replaceable inserts that define the nozzle shape and contraction ratio. The nozzle uses one inch inlet and outlet AN fittings, and has a total contraction ratio of 32:1 , with about 4:1 supplied by the transition region from the circular cross-section AN tube fitting to the two-dimensional nozzle. The nozzle region is formed in the gap between two large sapphire windows. Appendix 3 gives the engineering drawing for the nozzle and Figure 3.2.1.1-2 is a photograph of the disassembled nozzle and its windows. This two-dimensional nozzle design utilizes sapphire windows as walls giving optical access to the throat region from both sides. In additon, the slight turns in the flow at the entrance and exit of the nozzle allow the use of sapphire windows mounted at Brewster's angle which give optical access to the throat along an axis that is parallel to the flow. This allows DFWM gratings to be generated by optical beams normal to the flow or parallel to (or antiparallel) the flow.

The windows are edge polished to allow an O-ring to form a high pressure seal around their diameter. The throat spacing was 2.5 mm in the plane of the figure, and 5 mm in the plane normal to the figure; the 25 mm fluid channels taper down to the 5 mm spacing between the pressure taps and the normal incidence windows.

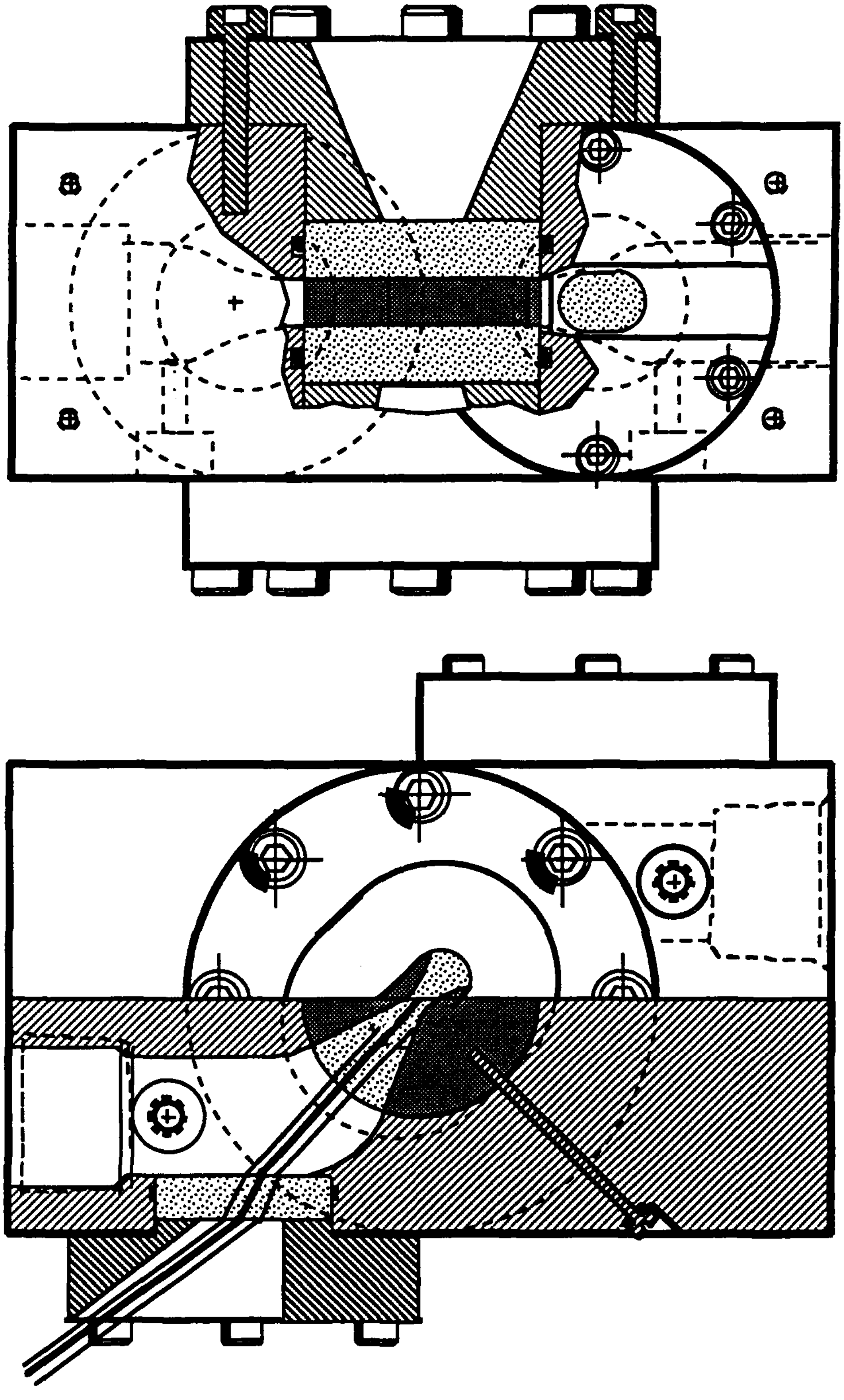

Figure 3.2.1.1-1 Illustration of the flow cell geometry. Top view (top) and side view (bottom).

Figure 3.2.1.1-1 The flow cell assembly.

3.2.1.2 Freon Recirculator

The most obvious means of providing for a continuous freon recirculation is by the use of a rotary or reciprocating pump. However, the operating conditons that are desired for the system are equivalent to operatIng the fluid very near the point of incipient cavitation. This is precisely the most difficult regime for most pumps, especially centrifugal pumps (which would be desirable because they have little flow pulsation compared to the piston pumps). Because of the unusual nature of the fluid, and the necessity to use pure freon; i.e., without disolved lubricants, the use of any conventional off-the-shelf pump would be risky.

The chosen alternative was to use a modification of the pressurized blowdown system that does not require suction on the pump inlet. This approach was implemented using a pair of accumulators. Accumulators are high pressure tanks whose internal volume is separated with rubber bladders . They are usually used in hydraulic systems as surge suppressors, with oil on one side of the bladder and compressed gas on the other side. In the first freon recirculation system design, liquified freon was used on one side and high pressure nitrogen was to be used on the other side to change the pressure of the accumulators. At the start of a cycle, one accumulator is full and the other one is empty. The system is pressurized to the desired operating pressure and nitrogen pressure would cause the freon to flow from the full tank to the empty tank. Since the accumulators hold 5 gallons, this would give at least 30 seconds of operation at the design pump rate before the tank would be emptied. The flow could then be reversed to pump the freon in the other direction through the nozzle.

To provide unidirectional flow in the nozzle, a pair of solenoid operated valves that switch one inlet between two possible outlets were used so that the system could pump fluid from one tank to the other but the nozzle would only experience unidirectional flow. This is shown on the left side of the schematic in Figure 3.2.1.2-1. Since a heat exchanger is located upstream of the nozzle, unidirectional flow would provide better temperature control. When it became apparent that the rather considerable nitrogen pressure and flow rate would not be available from the plant facilities, and laboratory sized gas bottles would not last long enough, the system design was modified so that the pumping was supplied by a hydraulic pump that pumped pumping oil rather than nitrogen. This system consisted of a constant speed motor with a shunt to vary the pumping speed. The motor runs unidirectionally so that a second pair of solenoid operated valves allows bidirectional pumping with the unidirectional motor. These valves are switched in unison with the freon valves. The system is now self-contained and only requires electric power for the 1 hp pump motor and GN_2 and freon gas bottles.

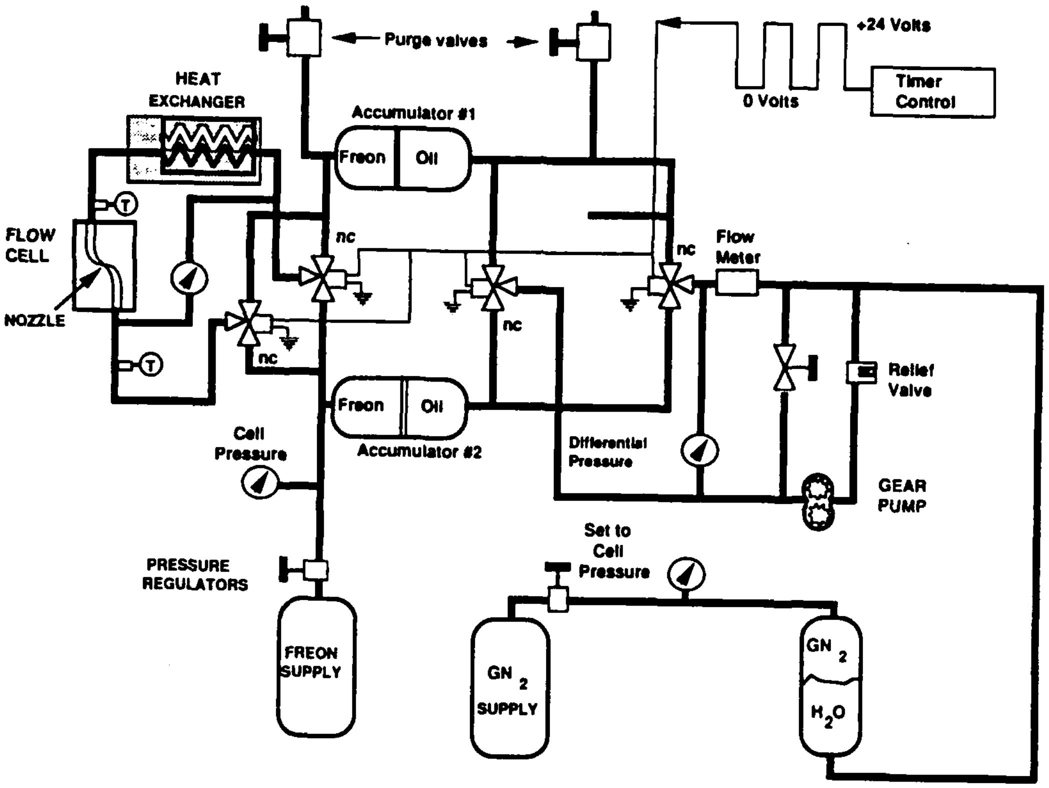

Fig. 3.2.1.2-1 The flow cell pumping stand fluid schematic.

A third accumulator is located in the hydraulic oil circuit, as shown on the right side of Figure 3.2.1.2-1. It is pressurized with a high pressure nitrogen bottle and provides a means to independently adjust the volume of the system. This allows the system to make up for small amounts of leakage by changing the volume of the system while keeping the pressure constant. A loss of approximately 2 1/2 gallons in leakage of either freon or oil can be tolerated before the system pressure will drop from the setpoint. This is set by the nitrogen pressure in the third accumulator, provided that the original fill of freon and oil is sufficient.

The pressure drop through the nozzle and freon recirculation loop was calculated using standard fluid methods, assuming the freon was well removed from the critical point. An upper limit of one to two horsepower in pumping demand was set as a practical limit on cost of the recirculation system. The heat exchanger, which was also the major pressure drop in the loop, was sized to be able to dissipate the heat from a one horsepower pump, assuming normal fluid properties. The pressure drop in the nozzle was calculated on the basis of constant density and Bernoulli's equation. The operating envelope along the coexistance curve of the PV diagram of figure 3.2-1 was then determined from the available pressure drop on the assumption that it might be necessary to take the fluid to the spinoidal line where spontaneous nucleation would occur without nucleation sites.

The final configuration of the freon recirculation system is shown in Figures 3.2.1.2-1 and 3.2.1.2-2. The system can be evacuated before filling with a roughing pump through the purge valves. The nozzle flow loop has a heat exchanger that uses a water bath that is thermostatically controlled by a recirculating water chiller and proportional heater system. The heat exchanger consists of 8 stock production liquid-to-air heat exchangers on a manifold that is immersed in the thermostatically controlled water bath. Thermocouple-type temperature monitors, silicon strain gauge pressure transducers and Bourden tube pressure gauges are used to monitor the fluid going to the nozzle. Not shown on the schematic, but later added during the experimental checkout phase, is a rotating vane type flowmeter to monitor the freon flow independently of the oil flow rate. This was thought necessary because of the large compressibility of the freon.

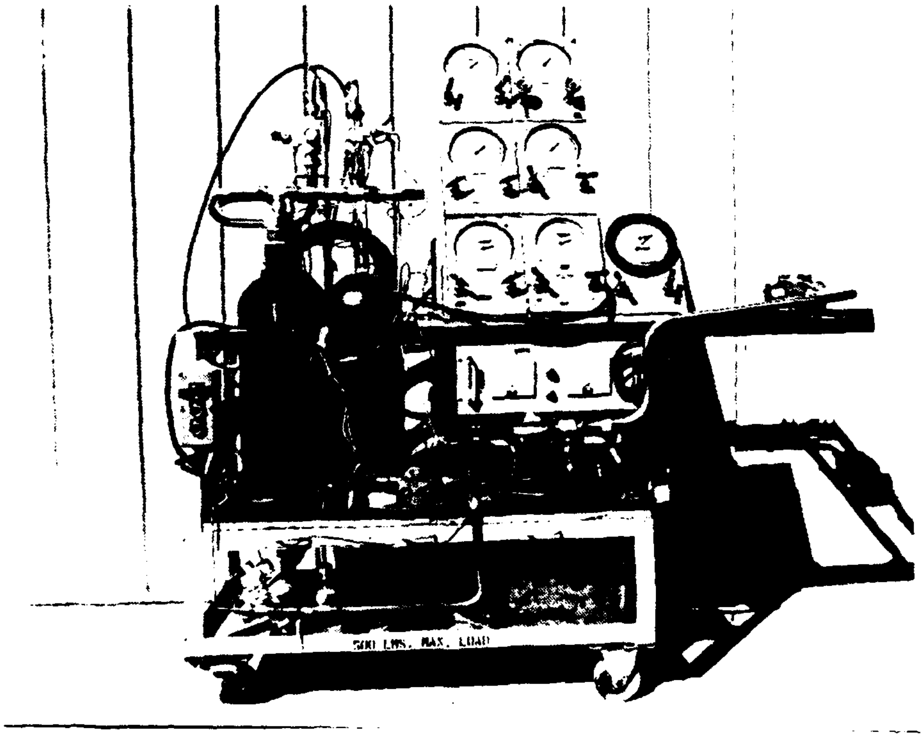

Fig. 3.2.1.2-2 Photograph of the completed flow apparatus.

Accumulators #1 and #2 act as a two piston pump to force the freon to flow through the nozzle. The "piston" in the accumulators is a bladder that separates the oil from the freon. An electrical timer based on a 555 IC chip switches all four valves simultaneously. The original timer circuit was supplemented during the checkout phase by end-of-stroke limit switches that were mounted in the neck of Accumulators #1 and #2. These specially fabricated high pressure switches closed when the bladders reached the top of their stroke and began to close a shutoff valve in the accumulators. This gave us a positive indication of the location of the bladders when a bladder would reach the top of it's stroke and close the contact. Closure of the switch would cause the controller to activate the valves and reverse the direction of the fluid flow between the two accumulators.

The GN_2 gas bottle supplied high pressure to the third accumulator to provide a constant pressure reservoir to make up for leaks in the system. A second GN_2 bottle also supplied GN_2 to the servo-actuators on the valves that amplify the force of the solenoids that in turn controlled the valves. A relief valve on the outlet of the positive displacement pump prevents overpressure in the oil circuit in case the accumulators should bottom out in stroke and the shunt valve is closed. The complete system was mounted on a cart as is shown in Figure 3.2.1.2-2. The Bourden tube gauges and valves were supplied from engineering stock (on loan) at no cost to the contract.

3.3 *Flowing Cell Operation*

The last 6 months of the program were devoted to bringing the flowing system to operational status and running optical experiments. Intially, leaks in the system were unacceptably large and the first couple of months were spent to eliminate this problem. This required the installation of gaskets and the replacement of all four 3-way solenoid-operated system valves.

Since it was found that the leakage of the valves was reduced by operating the servo-pneumatic portion of the valves at a pressure of at least 200 psig higher than the system pressure, the GN_2 pressurization system that provided both the system pressure and the servo-pneumatic actuator pressure was modified so that separated regulators and tanks could supply each function at a different pressure. The disadvantage of this modification is that there is the possibility of leakage of the high pressure GN_2 into the freon and contamination of the experiment with an inert gas. In the future, this might be avoided by finding either a more leak-tight valve or using freon in the servo-pneumatic actuator circuit as well.

The present leakage rate of the system allows operation of the system for about two days before the system pressure begins to drop. The system consists of three 5 gallon accumulators that are each half-filled with oil and half-filled with either freon or GN_2. The system has two freon accumulators and thus contains a total of approximately 5 gallons of freon at approximately the critical density and pressure (433 psia). Approximately 7 1/2 gallons of low viscosity oil was added to the oil circuit so that, at the operational pressure, each accumulator diaphram was at its midpoint. The system pressure was stabilized by a high pressure GN_2 regulator that set the pressure of the remaining 2 1/2 gallon volume in the third accumulator. This allowed a total leakage of about 2 1/2 gallons of critical point density freon (and/or oil) before the GN_2/oil accumulator diaphram would bottom and the system would begin to drop in pressure. Thus, the current leakage rate is about 2 lbs. of freon per hour. Fortunately, Freon 116 (C_2F_6) is not considered damaging to the earth's ionosphere since it is not a chloro-fluoro-carbon, so that the main drawbacks of the leakage are the time to refill, cost, and availability of the fluoro-carbon.

We found that availability was a problem since Freon 116 was not a commonly used refrigerent. The problem was made worse by the high fill pressure of the system. Typically, the freon tanks are delivered at around 600 psig. Although the pressure is only fractionally higher than the system pressure, a considerable fraction of the mass in the tank can be transferred before the pressure drops below the required system pressure of 433 psia because the freon is in a liquid-like state above the critical point. Nevertheless, the freon tanks do have a fraction of their freon remaining in the tank at 433 psia. At one time we resorted to pumping this out by chilling a small auxiliary tank in LN_2 and using it to liquify the remaining freon and then warming the tank while valved to the system to transfer the freon into the system. A more convient system would be a high pressure pump to transfer the freon. The present leakage rate is still much higher than desirable, and there should be considerable room for improvement. Automotive air conditioners operate at about 275 psig with a mechanical rotating seal and their leakage rates are typically less that about 3 lbs. per year.

This freon recirculaton system gave good control over the system pressure as long as there was adequate freon. However, control of the velocity and temperature was inadequate. The accumulator bladders offered unexpected resistance to filling. They behaved somewhat like an elastic ballon being filled rather than a rolling diaphram membrane. This caused the velocity in the system to vary according to the position of the bladders in accumulators #1 and #2 as they are cycled. When one accumulator was nearly full at the end of its stroke, the velocity would slow due to the elastic resistance of the near full bladder. The present system uses a fixed speed pump with a shunt valve to set the flow rate. Replacement of this with a variable speed pump with tachometer feedback would remove this problem. The use of floating piston accumulators was considered in the design phase, but the concern was that static (sticking) friction might cause irregularities in the nozzle inlet and outlet pressure.

The substitution of a specially designed centrifugal pump for freon would have greatly simplified the system. One local manufacturer expressed confidence in being able to construct one for $30 k in 3 months. The main issues were cavitation in the inlet, turbulence in the flow, and lubrication of the bearings with oil-free freon. Because of these uncertainties, we elected to go with the accumulator recirculation system. However, if this centrifugal pump alternative were sucessful, the system difficulties with leakage would probably have been much smaller and the system would have been quieter since the gear pump was quite noisy.

The temperature control of the freon recirculator was not as good as we would have liked. Fortunately, since the freon chosen has an operating temperature very near room temperature, the initial temperature could be controlled with the room air-conditioning thermostat as well as the temperature bath. The orginal flow loop design pivoted about the performance of the heat exchangers in the flow loop. Since these heat exchangers operated at high pressure, there were no off-the-shelf units available with suitable ratings, including Rocketdyne saftey factors. In addition, the major pressure drop in the flow loop was calculated to be caused by the heat exchanger. The heat dissipation caused by the heat exchanger pressure drop was thus the largest contributor to the load on the heat exchanger. Furthermore, the heat exchangers had to be rated and tested to a pressure of several times the operating pressure for safety reasons. This problem was finally solved with the selection of a low capacity oil heat exchanger using small diameter tubes. Although rated for a much lower pressure, they were tested to over 1350 psig without failure, so they were more than adequate for freon (but not Xenon). Up to 10 of these were mounted on a manifold in parallel and immersed in a water bath that was controlled by a large capacity chiller. Since the chiller provided control only by cycling the refrigeration pump on and off, an electric heater was added that was proportionally controlled by a very accurate temperature controller.

Despite this engineering and design effort, the heat exchanger does not appear to provide the temperature control that we calculate that we need. Two contributors to this are the location of the temperature measurement, and the specific heat, C_p ,of the freon. First, near the critical point the specific heat gets very large, this was not taken into account in the first calculations and it makes it more difficult to control the temperature of the freon. Second, a much larger heat flux can be delivered by the heat exchanger if the temperature difference across the heat exchanger wall is made larger. If the water bath temperature is controlled by a thermocouple in the freon loop just upstream of the nozzle rather than by a thermocouple in the water bath, the performance should be better. Since this freon thermocouple is built into the system, it should be a simple matter to make this change.

When the system is first run with the room temperature different from the water bath temperature, the largest fraction of the freon is in the accumulators rather than the heat exchangers. It is quite noticable then that the temperature is stepping up or down as the freon stored in the accumulators passes through the nozzle or the freon stored in the heat exchangers passes through the nozzle. This causes the freon to move about on the PV diagram and the degree of bubble formation to vary. If the system is recirculated long enough, this temperature nonuniformity decreases. However, the overall system temperature rises with time due to the heat input from the pumping energy deposited in the system. This should be considerably reduced if a variable speed motor is used and the shunt valve is closed. Together with the different water bath temperature control discussed in the above paragraph, it should be possible to control this problem of rising temperature.

To bring the freon more quickly to a common temperature, it would be desirable to provide water bath controlled temperature control to the accumulators as well. Since the majority of the freon is stored there, a modification using a water bath or copper pipes wrapped around the accumulators would bring the whole system more nearly to a common starting temperature. This would reduce the present dependence on accurate room temperature control.

Despite the difficulties discussed above, we were able to run the system for extended periods of time, totalling over 40 hours. Temperature control at present is about +/-0.5 ^{o}C at best. The operating point can be moved about on the PV diagram at will and placed at the desired point. At first there was a difficulty of inadvertantly jumping from the left (liquid) side of the co-existance curve to the right (gas) side. With experience this could be controlled and the desired incipient formation of bubble opalescence could be induced in the nozzle. Since the windows allow viewing only of the throat region of the nozzle, there is sometimes doubt as to just what are the upstream conditions of the nozzle. An upstream window to monitor the fluid conditions prior to the nozzle would help us determine just how close the system is to incipient bubble formation.

3.3.1 DFWM in the Flowing Cell Using the Ar^+ Ion at 514 nm

To bring the system to the point where we could perform experiments exhausted the alloted time and funds. We were able to run the system for about 8 hours with the nozzle situated in the DFWM optical experiment (details of this are discussed in Section 3.4.3). Using only the CW Ar^+ Ion laser, we were not able to detect a DFWM signal using the chopper and lock-in amplifier apparatus discussed in Section 3.4.3.

This brief experiment is far from conclusive, and it may well be possible to improve upon the details of this experiment and see a return. The pulsed dye laser should yield a larger signal and a few additional days of research would have made such a test possible. Since we have seen the DFWM signal with the near critical point static signals discussed in the following Section 3.4.2, it should be possible to acquire a comparable return even if the fluid is not flowing. Flowing the fluid and moving into the two-phase region could then be compared against the static case for the predicted enhancement. In the light of theoretical understanding of near critical point fluids, a longer pulse laser such as the YAG laser used in Section 3.4.6 probably would have yielded positive results. Evidence of additional enhancement from two-phase operation would be the goal of such long pulse flowing experiments.

3.4 Static NCP Cell Operation

Figure 3.4-1 shows the static cell mounted on the optical table. Temperature control is provided by circulating water from a thermostatically controlled water chiller/heater through the aluminum cell body. The static cell utilizes six uncoated sapphire windows, one on each face with normal incidence.

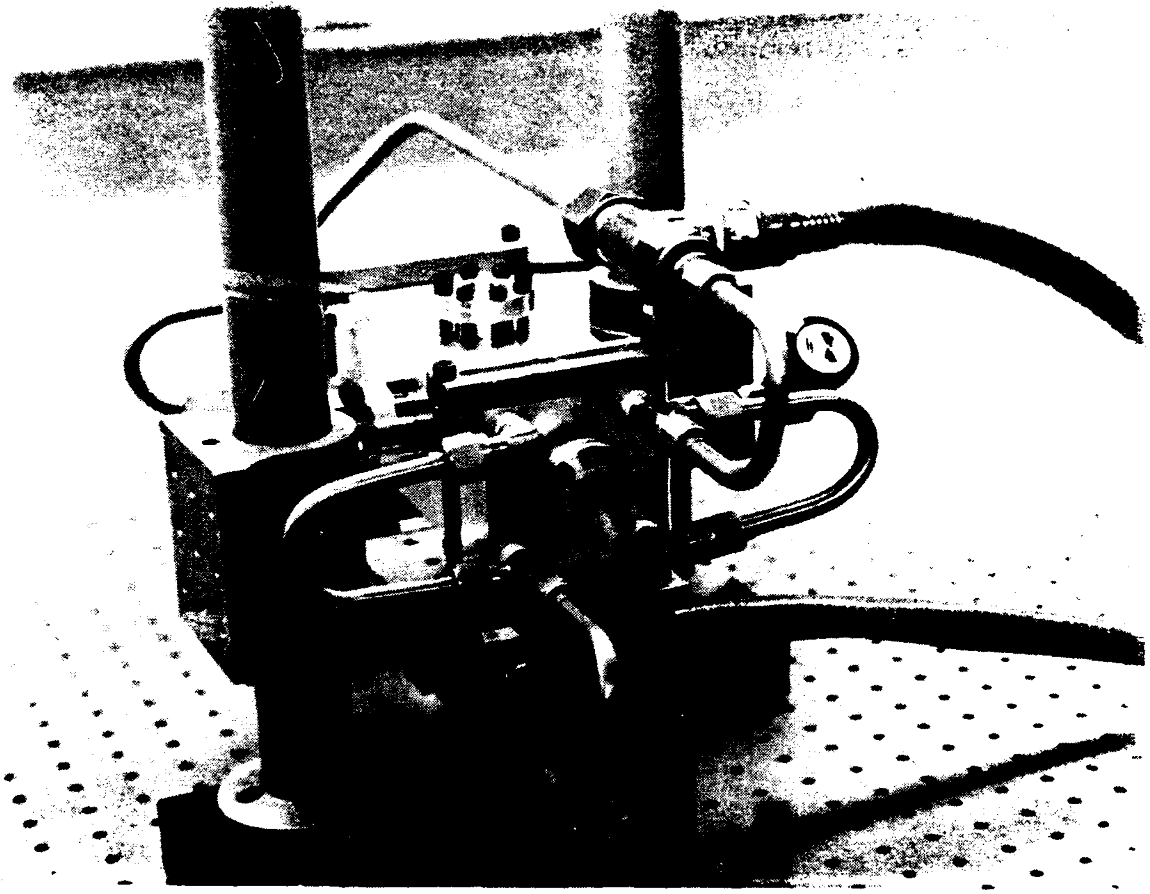

Figure 3.4-1 The static NCP cell showing the cooling connections and sapphire window flanges.

3.4.1 SBS Using an Excimer Laser at 351 nm

We began experiments with Freon 116; the experimental layout is shown in Figure 3.4.1-1 A collimated beam from a 351 nm excimer laser passes through a variable attenuator, an uncoated beamsplitter, an aberrator plate, and is then focussed by a positive focal length lens into the static cell. Beams travelling in the backwards direction are sampled by the beamsplitter and then observed on the fluorescent card near the beamsplitter. We have preliminary results indicating that we have observed Stimulated Brillion Scattering (SBS) and consequently phase conjugation of the 351 nm beam. Although we have not yet confirmed these results with the required SBS red shift and beam quality measurements, we obtained a collimated reflection that had a threshold, that occurred with and without an aberrator plate, and (most significantly) that remained collimated when the lens in front of the cell was translated. (Note that a spurious refection from the window of the cell would have gone in and out of collimation as the lens was translated.)

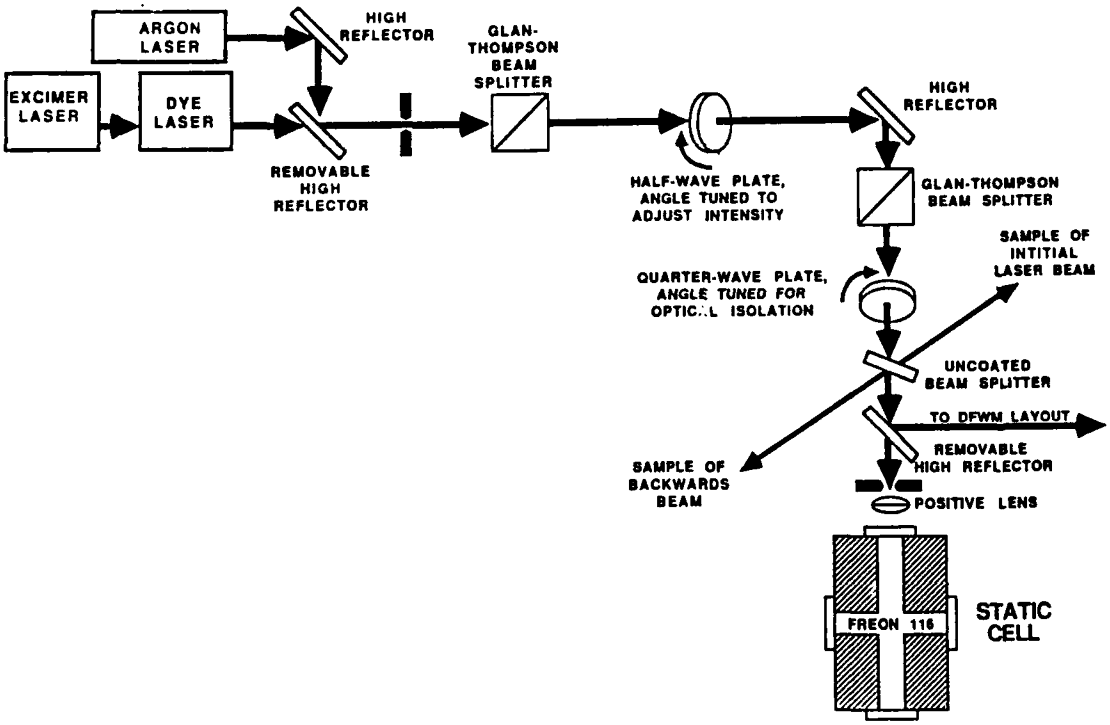

Fig 3.4.1-1 Experimental layout for SBS.

3.4.2 SBS Using an Excimer Pumped Dye Laser at 514 nm

While the SBS experiment at 351 nm was not difficult, the awkward beam size and invisible beam were expected to make the DFWM experiment difficult because alignment of the beams would become critical. A CW Ar^+ Ion laser and an excimer pumped dye laser were available for the DFWM experiments. The 514 nm operating wavelength was chosen so that the lasers could use the same beam path. The optical setup time was now reduced since the same optics and alignment could be used for both the high power pulsed experiments and the low power CW experments. The pulsed dye laser, a Lambda-Physik Model 2002 master oscillator plus power amplifier design, was operated without beam expansion optics in the power amplifier. This had the advantage of improving the beam quality and reducing the beam diamenter to more nearly match the Ar^+ Ion beam diameter. Since the maximum power that was necessary for the DFWM experiment was limited by the SBS threshold in any of the pump beams, the reduced power of the dye laser was still more than adequate.

Preliminary SBS experiments were repeated with this dye laser to verify the operation of the detectors and the data acquistion system. The experimental setup is the same as shown in Figure 3.4.1-1. Data taken using the static cell near the critical point are shown in Figure 3.4.2-1. Each data point is the average of 10 laser shots. This is the first data taken of nonlinear optical effects in near critical point (NCP) fluids.

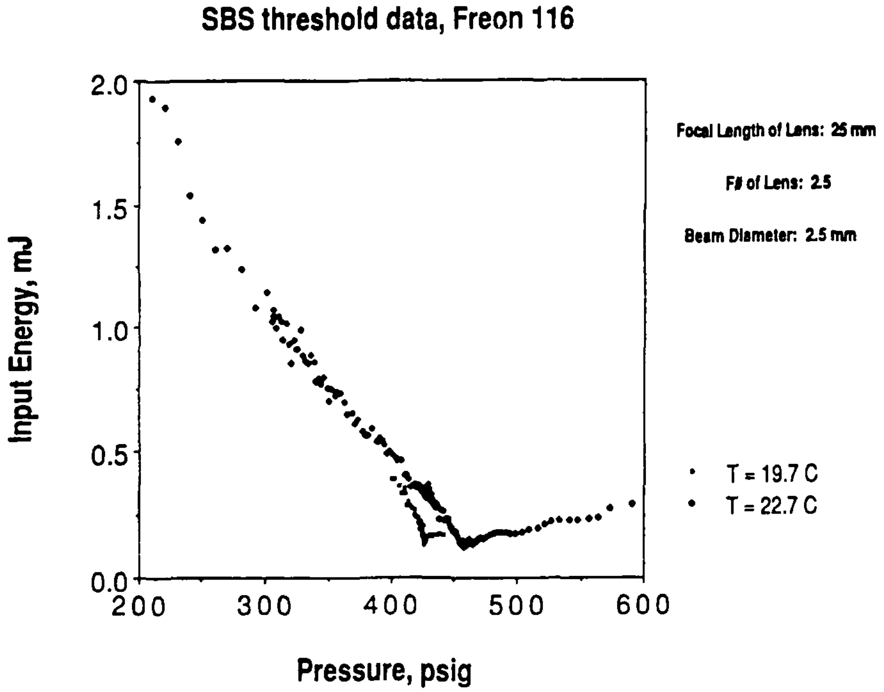

Fig 3.4.2-1 SBS threshold as a function of pressure.

The data in Figure 3.4.2-1 were taken by slowly scanning the pressure in the static cell from high perssures well above the critical point to low pressure while keeping the temperature at the critical temperature. The temperature was monitored with a Hewlett Packard quartz thermometer accurate to better than 0.01 C. However, since the temperature probe was not suitable for mounting into the static cell, and a more suitable type could not be obtained during the program, the temperature was monitored in the recirulating water bath so there is some unknown error in the temperature measurement that results from the difference in temperature between the recirculated water and the actual static cell fluid. These data, together with the measurements of sound velocity in Freon 116 [1] were taken near the critical point (and data taken very near the critical point in CO_2 - Ref [2]), verify that the finite adiabatic compressibility near the critical point limits the reduction in SBS threshold. If the fluid were more nearly infinitely compressible, the sound velocity would go to zero and the threshold for SBS would also drop to zero. The finite compressibility results from the relatively rapid response required of the media for these short pulses because only the DC response diverges near the critical point.

It is interesting to see that the SBS disappears entirely near the critical point. In Figure 3.4.2-2 the data are replotted with higher resolution to show the narrow region of extinction. This extinction is coincident with the observation of strong critical opalescence. As shown in Appendix 2, the increase in scattering losses from thermal noise-induced density fluctuations (critical opalescence) exceeds the increase in SBS gain as the critical point is approached.

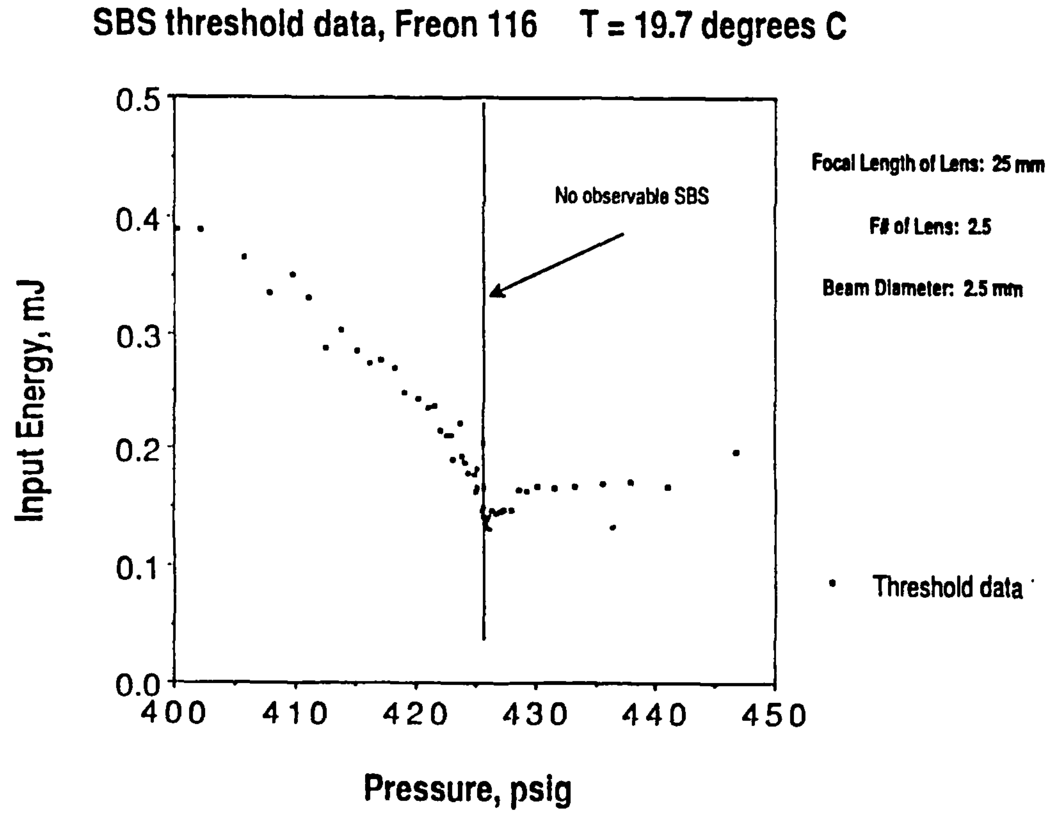

Fig. 3.4.2-2 SBS threshold as a function of pressure, (high resolution).

In Figure 3.4.2-2 it is also interesting to see that the curves for SBS threshold on the low pressure side are essentially identical for a large change in the focal length of the lens used for focusing the beam into the fluid. In other words, the SBS threshold is total power dependent rather than intensity dependent. This is what would be expected for any SBS process since the SBS threshold is dependent upon the laser intensity times the interaction length. The shorter focal length lens increases the intensity and decreases the interaction length so as to keep the product constant. Very near the critical point the short focal length lens has a slightly lower SBS threshold. This is thought to be due to the greater length of propagation of the converging cone of light in the long focal length geometry. Since light is scattered out of the beam by critical opalescence in the converging beam before the beam waist is reached, and since the input power is near threshold, a large reduction in the focal length reduces the propagation length and thus the scattering losses in the approach of the light to the beam waist, slightly decreasing the apparent threshold.

The usual experiments were made to verify that the return from the observed SBS was the phase conjugate return. Movement of the lens and tilt of the windows showed no changes in the return beam. The beam quality was monitored and no change in the collimation or beam quality was observed when aberrators were inserted into the input beam path.

Figure 3.4.2-3 shows the measured reflectivity of the NCP SBS as a function of the input power and the pressure. Again, the largest response occurs near the critical point with reflectivities over 50% for modest input powers. This response is roughly an order of magnitude greater than the response that is available from the best Kerr media. In addition, due to the depression in acoustic velocity, the red shift is expected to be very low. This has been recently verified by Hovis and Kelly [3] to be as low as 150 Mhz at 1.06 μm for the conditions of their experiment.

The results of this Section alone are interesting. These experiments also gave us the impetus to understand the stimulated response in a deeper level as we did not see the expected divergences in the reflectivity. The reasons, mentioned above in references to the gain to noise competition and other dynamics, did not come to light until after the experiments had been terminated to allow for the DFWM tests. The experiment also served to verify the operation of our DFWM apparatus. However, since much larger increases in response were felt possible in DFWM, we continued on with the DFWM experiments described in the next Section.

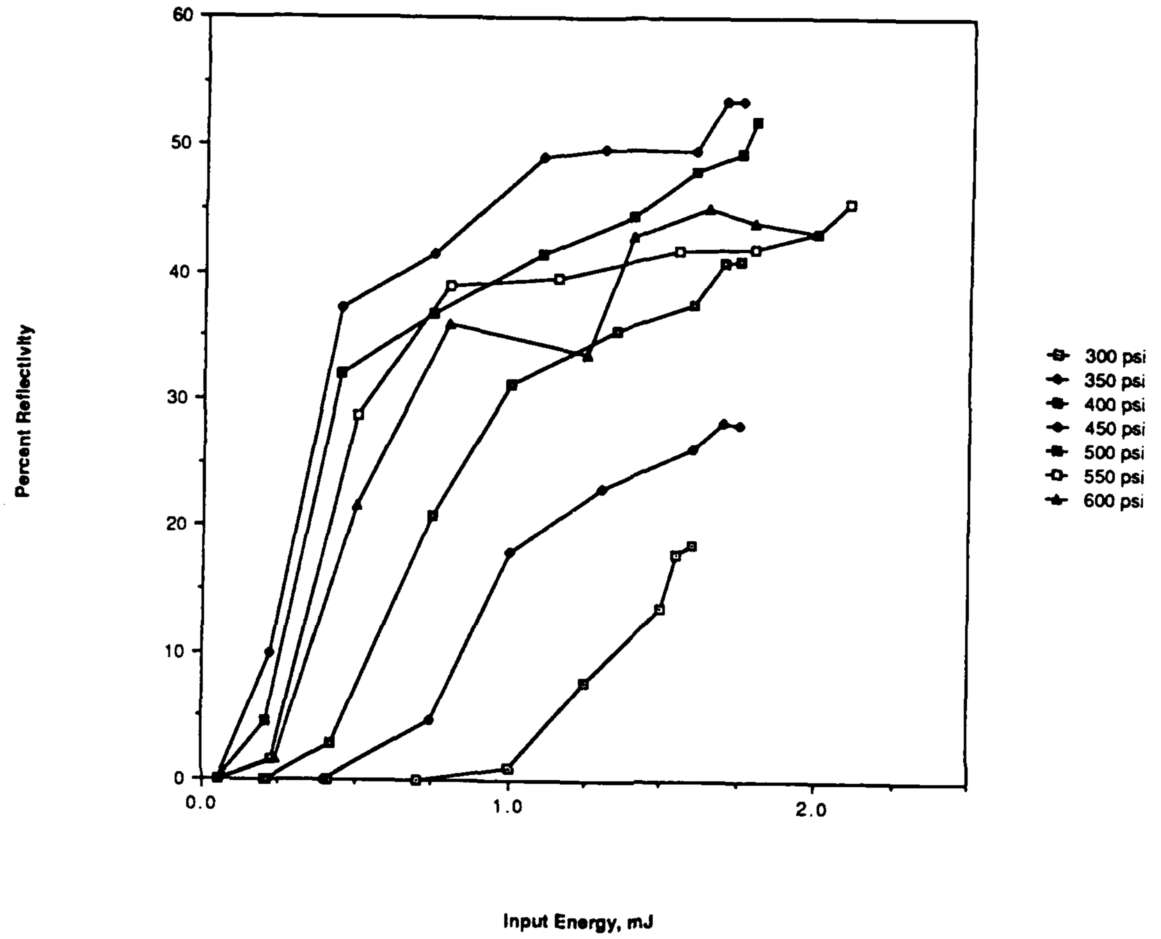

Fig. 3.4.2-3 Experimental SBS reflectivity as a function of input energy and pressure.

3.4.3 Search for Self-Focusing Using the Ar^+ Laser at 514 nm

The first measurements of the response of Artifical Kerr Media used self-focusing rather than DFWM since it is a much easier experiment. In addition, we now understand that the SNR of DFWM is generally poor at the low power levels that are available CW. A quick exploration of self-focusing using the Ar^+ Ion laser was made but no evidence was seen. This is disturbing since the physics would predict its exisence. However, it is a welcome result as self-focusing is a common limitation in NLO experiments. We think that the explanation for this may lie in the long time constants associated with bulk self-focusing. Since the time constant is proportional to $D_T q^2$, the formation time of the density gradient for whole beam self-focusing is much longer than the grating formation time. For our experiment, the predicted grating time constant for the 0.25 μm grating is about 20 μsec, while the approximately one mm diamter beam would have a time constant of nearly 100 sec. This would probably have exceeded the thermal stability of the temperature regulation so that convective instabilities would have interfered with the growth of the self-focusing. Since no coherent effects were needed and beam quality was not an issue, the cw beam in this experiment could be turned up to 17 watts by running on all lines. Using this input power, the NCP medium showed signs of absorption driven convective instabilities. This could be an issue in using NCP media at high power. The nearer the medium is to the critical point, the more susceptable the medium is to a thermal disturbance which can deflect the beam or change the temperature away from the desired near critical point. Presumably, these consideration would be reduced in the flowing nozzle system for two reasons. First, the medium is flowing rapidly, so the temperature rise is minimized. Second, the medium is not near the critical point so that its susceptability to critically divergent behavior may be reduced. However, we do know that the nucleation rate has a extreme temperature sensitivity, so that good temperature control may still be an issue for the nozzle based system.

3.4.4 DFWM Using the Excimer Pumped Dye Laser at 514 nm

The DFWM experiment involves several added complications beyond the SBS experiment, not the least of which was the careful alignment of the beams. It was discovered that near the critical point, the gravitational gradient in density of the fluid was sufficient to create a prism-like effect, which deflected the beam towards the table as a function of the fluid temperature or pressure. For this reason, it was necessary to perform the experiments with the pump and probe beams near vertical. Otherwise, the alignment of the experiment would become a function of the temperature or pressure of the static cell. In addition, since both the excimer laser and the dye laser used oscillator-amplifier geometries (to provide good laser linewidth control and good beam quality), they are very susceptable to retroreflection of power back into the laser. Backwards going power is concentrated on the master oscillator mirrors and can easily cause damage.

The simple quarter-wave plate technique for isolating the laser is not sufficient for DFWM without certain modifications. The two counterpropagating pump beams were generated with equal path lengths to minimize laser coherence issues. Their polarizations were made orthogonal so that the pump beams would not be fed directly back into the laser. With this geomentry, a polarizing beamsplitter directs the pump beams out after they have passed through the cell. The polarization of the probe beam may be selected to match one or the other of the pump beams, the gratings that are formed can be selected to be the result of either pump plus the probe, or any combination of the two. Since the probe beam is very nearly parallel to the pump beam path, the grating formed by the counterpropagating pump and the probe will have a very short period, and the grating formed by the pump that is nearly parallel with the probe will have a long grating period. The choice of these two gratings is made by rotation of a half-wave plate in the probe path.

The maximum size of the DFWM signal is reduced by at least two in this geometry. However, the grating formation time constants are different for the two gratings. As is discussed in Section 2.1.4, only the short grating is expected to generate a signal for the very short laser pulses used. The "breathing mode" grating is not expected since the media response time is insufficient. Finally, the polarization selection has the advantage of rejecting thermally induced scatter from the near parallel pump beam, and thus increasing the signal to noise ratio by two.

A schematic of the DFWM experiment is shown in Fig 3.4.4-1, and a photograph of the experiment using the pulsed dye laser is shown in Figure 3.4.4-2. The input beam passes through a kinematically mounted mirror that allows the selection of either the Ar^+ Ion laser or the pulsed dye laser with almost no change in the experiment. A single lens system expands and then focuses the beam into the experiment. This adjustable telescope system allowed a choice in the beam waist diamenter. The path lengths of the two pumps and the probe are all exactly matched in the geometry that is shown. The pumps form a parallelagram and the probe beam is split off in a parallel geometry as shown. The laser power is split into equal one third fractions for each of the two pumps and the probe. This gives the maximum grating modulation and phase conjugate return signal.

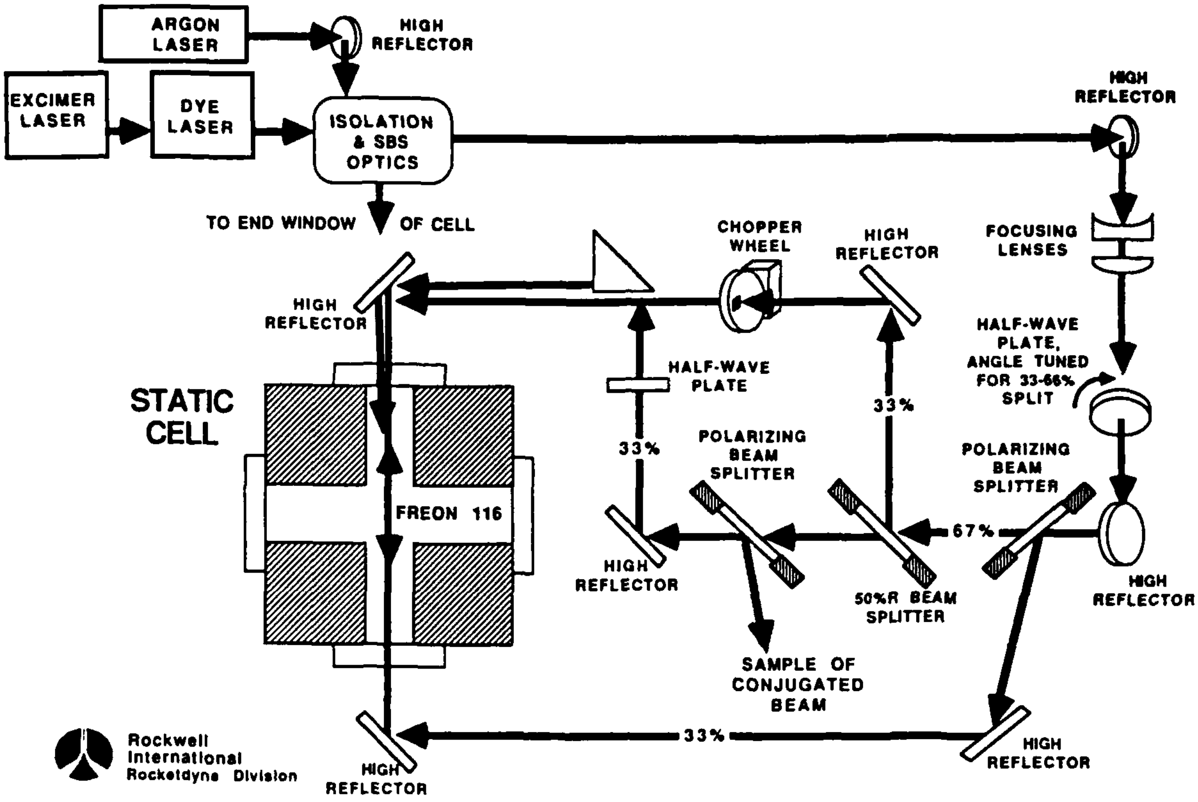

Fig 3.4.4-1 Schematic of DFWM experiment.

In order to ensure that the three beams overlap in space, and focus to a common point, a microscope with a CCD camera was used to observe the interaction region. A metal pinhole was installed in the static cell at the center, and the position of the beams was observed with, and without Freon in the cell. Since no motion was seen, later experiments were aligned by sliding out the static cell and replacing it with a thin cover slip glass or tissue paper at the height of the center of the cell. The microscope was used to overlap the three beams and to find the beam waist of each beam in turn. The two pumps are made exactly counterpropagating by first overlapping the beams on their mirrors, and then by using a polarizer at 45 degrees to the polarization of both pump beams to resolve an interference pattern. When the fringe spacing is made larger than the beam diameter, the pumps must be counterpropagating to better than a wavelength divided by the beam diameter. These alignments can be done using either the pulsed dye laser or the cw Ar^+ laser, but most of the time the Ar^+ ion laser was used for preliminary alignment before switching over to the pulsed dye laser for final alignment.

In the photograph of Figure 3.4.4-2 the phase conjugate beam path can be seen as the faint beam that comes out of the plane of the pump and probe beams and enters a lens in the foreground. The lens focuses the beam on a photodiode. The alignment of this photodiode was done by increasing the power of the probe above the SBS threshold and changing the polarization of the return beam with a halfwave plate. This allows the SBS return to match the expected DFWM polarization and pass through to the detector. The highly collimated phase conjugate return can be seen as a bright focused spot on the detector.

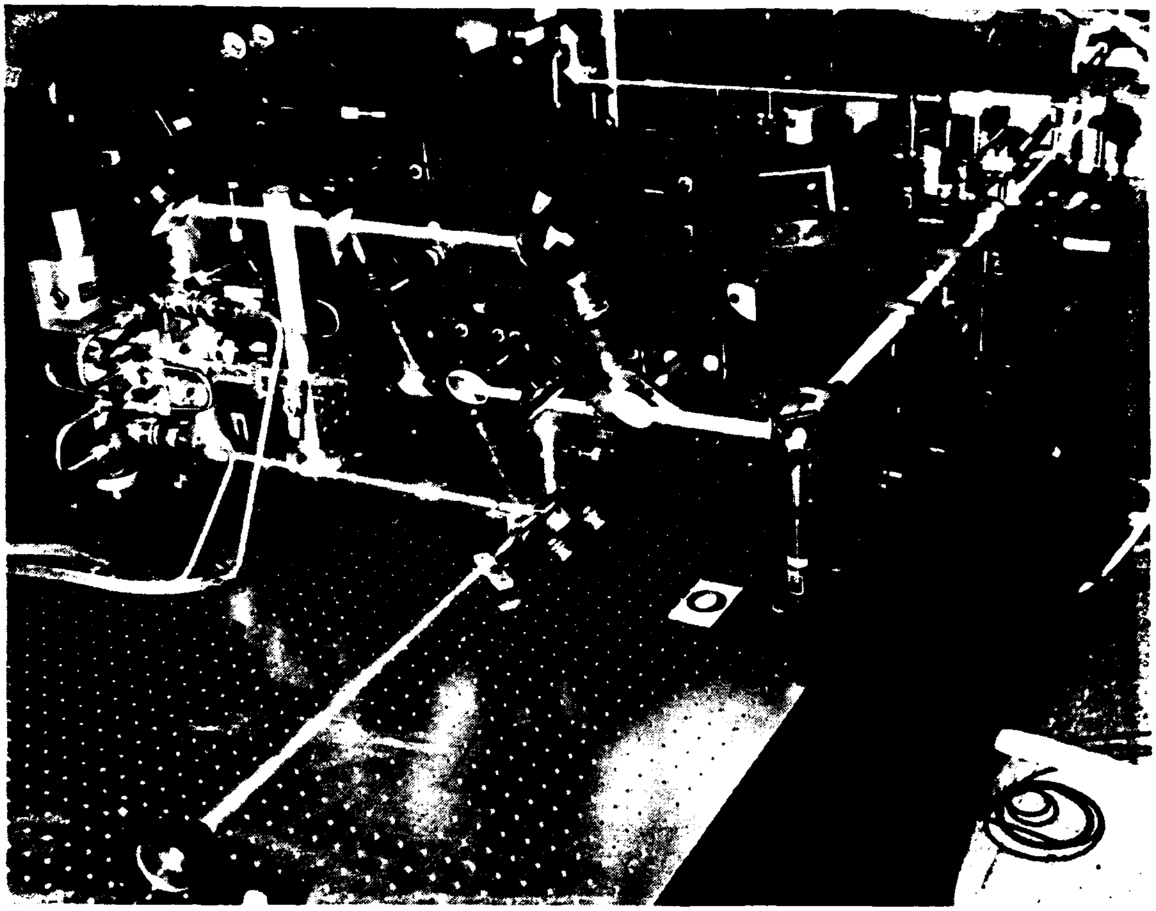

Fig. 3.4.4-2 Photograph of phase conjugate return in DFWM experiment.

The experimental layout was also configured to allow the flowing cell, which was under construction at that time, to directly replace the static cell without modification to the optical layout. Thus, preliminary experiments with the static cell could be directly followed by experiments in the nozzle, with and without flow.

A DFWM return in the phase conjugate direction was observed by eye and recorded in Figure 3.4.4-2. However, there was considerable fluctuation in the magnitude of the signal, and Fig. 3.4.4-3 shows the enhancement of processing the signal with a boxcar integrator using a 30 pulse moving average. Blocking either pump beam completely eliminated the signal proving that the signal was not generated by simple SBS. The extreme right of the trace shows the unaveraged signal. Fig. 3.4.4-4 shows a plot of the magnitude of the signal as a function of the temperature of the cell. The lack of positive correlation with the reduced temperature ($T - T_c$), immediately brougth our attention to the matter of the role of the dynamics in DFWM. The theory developed in Section 2.1.4. was in direct response to this missing temperature dependence. In short, the integration time of the DFWM grating reduced the effective laser peak laser power of the dye laser to only 100 watts. In addition the temperature control problems and the narrow region of the reflectivity peak in PVT space added to the small DFWM reflectivity.

The primary contribution of this expriment was to demonstrate that DFWM can be done in a NCP fluid using a high peak power source. A concern of the experiment was misalignment of the beams due to thermally induced gradients in the fluid. Absorption of laser power appeared to contribute noticeable to this problem in the CW experiment described in the next Section. Pulsed DFWM using the nozzle with the flowing system remains untried due to time and funding limitations. Since our theoritcal understanding of the time constants associated with operation inside the co-existance region (that the nozzle would generate) remains undeveloped, it is not known at present whether the large enhancement would be seen in that experiment.

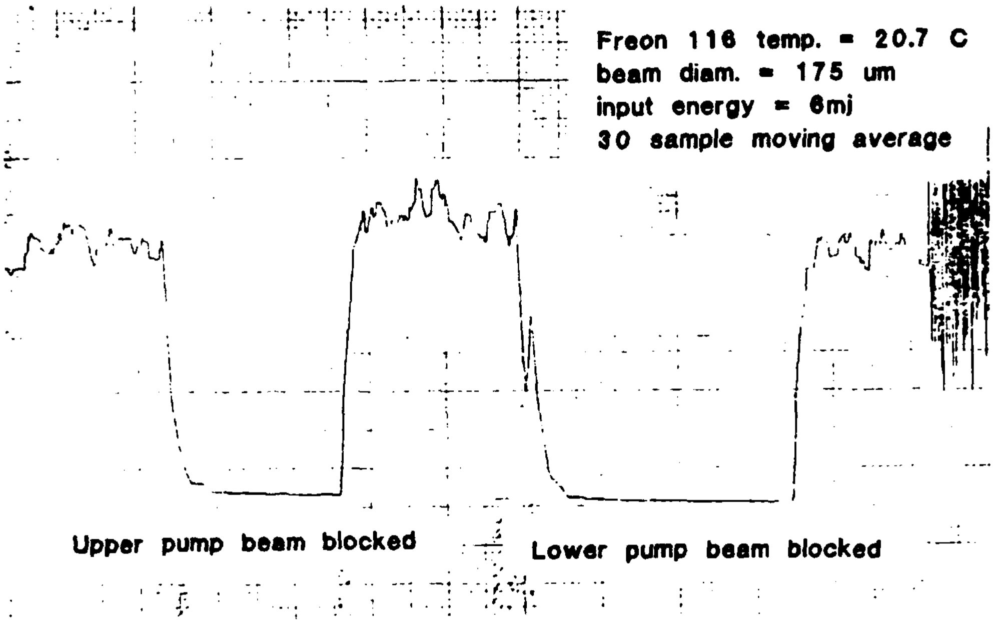

Fig. 3.4.4-3 DFWM return signal.

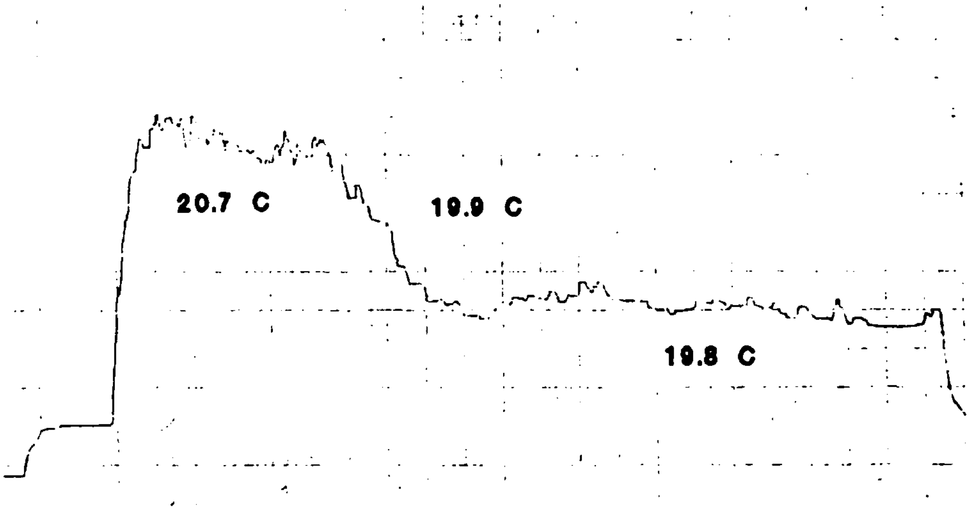

Fig 3.4.4-4 DFWM return as a function of temperature.

3.4.5 DFWM Using the Ar^+ Laser at 514 nm

Following the experiments described in the previous section, CW experiments using the Ar^+ Ion laser were attempted. In this case a dual frequency chopper wheel was used to chop the pumps and the probe at two different frequencies. The phase conjugate return was monitored at either the sum or difference frequency with a lock-in amplifier. Although the laser is capable of nearly 17 watts at full output, when operated single line at 514 nm and TEM_{00}, the output was about two watts. After losses in the optics, the net power in the experiment was about one watt. The experiment was also tried with a pair of short focal length lenses mounted in the pump beams just before the beam turns to enter the test cell. These lenses reduce the beam waist from approximately 175 µm to 60 µm. As discussed in Section 2.1.3, this increased intensity is predicted to increase the DFWM reflectivity for our experimental conditions where the optimum interaction length is much greater than the experimental interaction length.

The result of these experiments was inconclusive, with a signal to noise ratio close to or below unity. In contrast, our analysis predicted that an optimized experiment should have a reflectivity of about 10^{-4}, which should have been observable. The sensitivity of the apparatus was in the 10^{-8} range of reflectivities. Signals, deep in the noise, were seen, but they could not be identified as DFWM with absolute certainty. The infinitesimal signals and the difficulty in obtaining them, contrary to what we thought would happen from our pulsed DFWM experiment, led us to pursue the theory for the reflectivities and the SNR in much greater detail. Much of section 2.0 was done after the null results of the CW 514 nm DFWM experiments.

3.4.6 DFWM Conclusions

The main reason we did not see the high reflectivities was the fact that the predictions for the scattering loss did not agree with the laboratory observations. We knew that the total loss of a laser beam traversing the cell should be about 30% to achieve the maximum reflectivities. In the laboratory, this level of scattering was seen at only 0.05 C away from the critical point. It was under these conditions where DFWM was attempted. The results could not be bettered, even though it was argued that the reflectivity should be orders of magnitude greater.

The discrepancy was discovered when the scattering loss at 0.05 C away from the critical point was calculated and was shown to be approximately two orders of magnitude smaller, hence less DFWM return, than what was observed. The fluid should have been clear, but it is now postulated that transient fluctuations from cycling the cell in temperature became "frozen in". The equlibirating time of the cell is long and the transients cannot decay in the short time changes were made in the cell temperature. Therefore, the scattering loss is augmented by the presence of these long-lived transients, but they do not add to the DFWM gain. The calculations indicated that the cell must be operated much closer to the critical point than before. However, to achieve these conditions, our control of static cell temperature would require that we approach the critical point to better than 10^{-4} degrees, which would have required an undesirably long time to reach equilibrium in the cell. In addition, the absorption coefficient of the freon would have to be extremely low so that temperature rise from the laser beam does not move the fluid away from the critical point.

The reflectivities were then recalculated with this new information about the true scattering loss incorporated into them. An example of the calculations are sumarized in Table 3.4.6-1. The first column, entitled peak power, takes into account the energy per pulse and the pulse duration for the dye laser and the average power for the Ar^+ Ion laser. The second column folds in the dynamic effects of finite grating formation time on the peak power. The Ar^+ Ion laser is not reduced while the dye laser is reduced by the ratio of the grating formation time to the pulse duration. The spotsize is taken to be a 100 µm square. R (L=*opt*) is the calculated reflectivity assuming an optimized interaction length at 0.05 C away from the critical point. It is calculated from Equation 2.1.3-5. The temperature is 292.7 K and the wavevector is for 514 nm incident light. The R (L=0.04) calculation replaces the αL product required at 0.05 K away from the critical point with a product which uses the same α, but the L is now the true length of the interaction region, 4 cm. The drop in reflectivity is great and is much more in agreement with the experimental results for both the pulsed and the CW lasers.

TABLE 3.4.6-1 Calculated Reflectivities at 514 nm

	P_{peak}	P_{eff}	w_0	R (L= *opt*)	R (L=0.04)
Pulsed	33 kW	16.6 W	100 µm	0.31	8.1×10^{-5}
CW	0.3 W	0.3 W	100 µm	9.9×10^{-5}	2.6×10^{-8}

This peak in the reflectivity through optimization of the αL product is seen to be strongly dependent on the thermodynamic divergences at the critical point, as was pointed out in section 2.1.2. For these reasons, it was decided that this experiment to demonstrate high DFWM response at the level of a one watt signal was not reasonable given the new understanding of optimized DFWM response in NCP media that we now have. Instead, we returned to a pulsed laser to get higher power levels, but with a laser of much longer pulse than the 10 nsec pulsed dye laser. Since the NCP media is nonresonant there was no difficulty in switching to 1.06 um and this experiment is described in the next section.

3.4.7 SRS at 1.06 μm Using a Nd:YAG Laser

We conclude from Section 2.1 and the experiments in 3.4, that pulse lengths in the microsecond regime are necessary to see NCP enhancemnts. In addition, the SNR is greater at longer wavelength although the reflectivity would be lower for all other conditions equal. In order to test this prediction, an experiment was quickly assembled that used a long pulse Nd:YAG laser that was developed on a Company sponsored program for use as an FEL photocathode laser. This laser, shown in Figure 3.4.7-1, uses a CW master oscillator and two flashlamp-pumped amplifier stages to create long pulses of very carefully controlled flat-topped time-amplitude profile. This sharp turn-on and turn-off with constant amplitude is achieved with feedback controlled electrooptic modulators. This laser system has a mode-locked master oscillator that was orginally designed to deliver pulse trains of micropulses in macropulse groups to synchonize with an RF FEL. For the purposes of this experient, the mode-locking feature was turned off so that there were no high intensity pulses to obscure the results. The laser operated multi-longitudinal mode with a beam quality twice the diffraction limit.

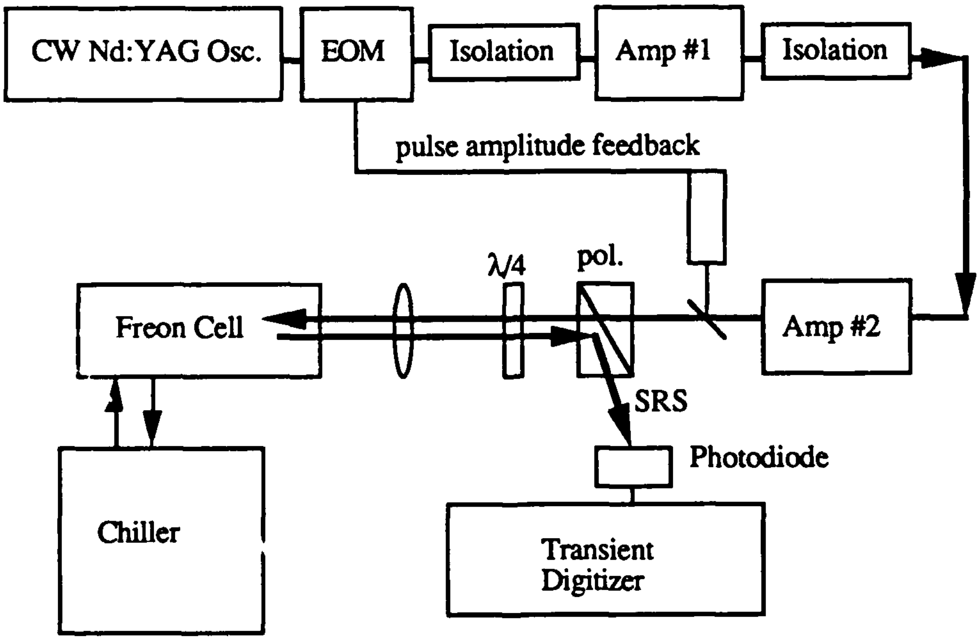

Figure 3.4.7-1 Long Pulse SRS Experimental Layout

Faraday isolators between the laser amplifier stages and a polarizer / quarter-wave plate isolator after the final amplifier stage attenuate the spontaneous and backscattered radiation. The standard SBS type of experimental layout was used, as shown schematically in Figure 3.4.7-1. Backscattered light is directed out by the polarizing beamsplitter. Some backscattered light leaks past this polarizing beamsplitter and the Faraday isolators and is amplified in the reverse direction by the YAG amplifiers. This backward going light limits the output of the laser to about 20 mJ or 10 % of its maximum output when the NCP cell is operating near its CP.

The backscattered light is monitored by a photodiode with neutral density filters to attenuate the light and calibrate the detector. A transient digitizer acquires the data and provides the output display. A second photodiode is used as the trigger for the transient digitizer.

The results of this experiment are quite convincing evidence of CP enhancement and are shown in Figure 3.4.7-2. A flat topped laser pulse of 20 usec duration is focused into the cell with a lens of 15 cm focal length. When the static cell is operated more than a fraction of a degree (0.3 ^{o}C ?) away from the critical point no backscatter is seen at a peak intensity of ~4 kW. Temperature scans could not be done at higher powers than this, because when the reflectivity did peak the stimulated backscatter overcame the isolation in the laser. At NCP conditions, a strong bacscatter is seen with a 10 usec turn-on time. At a power level of only 2 kW, the average reflectivity is about 30% with a peak reflectivity of about 60%. The reflectivity is seen to be still rising sharply at the end of the 20 usec laser pulse, which suggests that still higher reflectivities can be seen with longer laser pulses. These data were obtained very quickly and time was not available to redo all of the experiments. Other factors entered into the difficaulties of obtaining high reflectivity data. At large reflectivites a hole was burned through several of the ND filters in front of the photodiode. This gives some evidence as to the phase conjugate properties of the backscattered beam. Upon visual inspection, near the critical poin the cell is completely murky and opalescence in appearence. The non-stimulated backscattered light from the cell is irregular in shape and changes with the cell fluctuations. The stimulated backscattered beam, however, was close to circular in shape and did not fluctuate with the cell at the large peak returns. A frequency redshift and a precise phase conjugation fidelity measurement were not attempted.

Several backscattered pulses of decreasing intensity are shown superimposed in Figure 3.4.7-2. These represent backscattered returns for the same laser operating conditions but with the static cell temperature moved slightly off the critical point. The temperature of the NCPF is not known exactly since the cell is stabilized and the experiment is run over a period of only approximately 5 minutes. This time is insufficient for the NCPF to reach a thermal equilibrium due to the "critical slowing down" of equilibrating processes in the fluid. Preliminary evidence suggest that the backscattered reflectivity reaches a maximum for pulses in the 100 to 200 usec regime and the threshold of stimulated backscatter has been reduced from 750 watts to approximately 400 watts. The grating formation time constants varied from about 3 µsec to about 20 µsec during the experiments. A plot of time constant versus temperature could not be made to the accuracy required, because of the inability to precisely measure and control the temperature and the lack of dynamic range due to isufficient isolation in the laser.

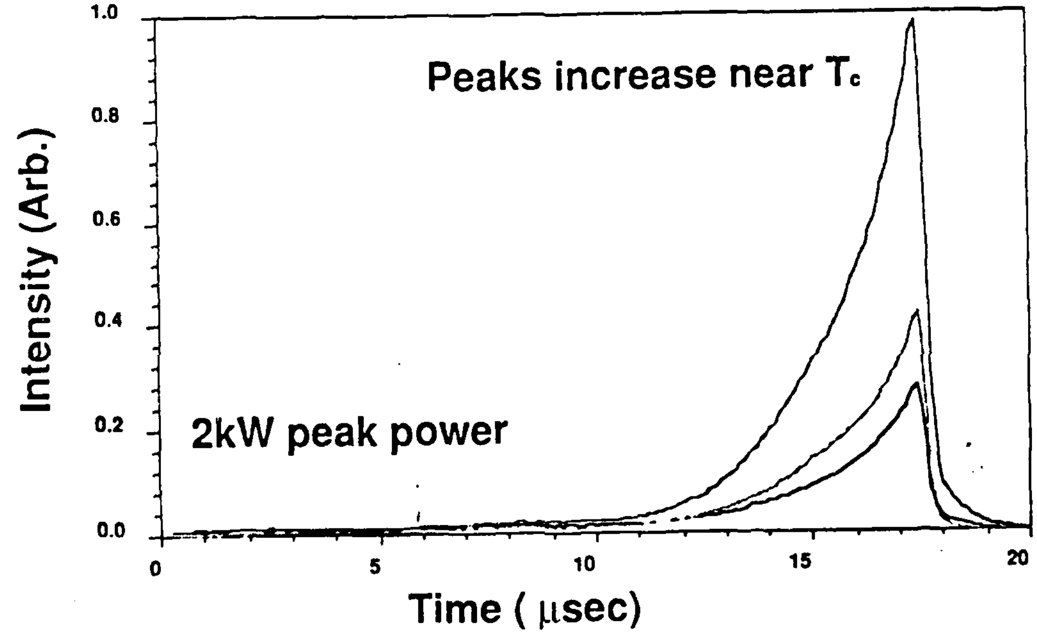

Fig. 3.4.7-2 SRS exhibits 20 µsec response time.

The observed stimulated scattering threshold is a factor of 1000 below the threshold of previous materials like CS_2. This very sharply dependent enhancenment in the nonlinear response was not seen in the short pulse SBS data, and the theory developed in Section 2 strongly suggests that these are the critical point enhanced, nearly stationary density waves generated by either electostriction or thermal effects. This process is identified with Stimulated Rayleigh Scattering (SRS). SBS can most probably be ruled out by the fact that the SBS accoustic wave time constants are still in the tens of nanoseconds, even at the critical point, because they do not depend on the thermal transport properties of the fluid, but on the viscosities. Since the predicted absorption coefficient in the NCPF where

Stimulated Thermal Rayleigh Scattering (STRS) can equal Stimulated Electrostrictive Rayleigh Scattering (SETS) is only .0005 cm^{-1}, a careful measurement of absorption coefficient in the actual test cell (to include the effects of contaminants) is necessary before we can be certain which mechanism dominates.

Obviously, a great deal remains to be done to explore this NCP enhanced mechanism. While we have not explicitly tested for phase conjugation fidelity, the very collimated nature of the backscattered beam is very encouraging. The beam is collimated enough to pass through the long amplifier chain, even when the NCPF is obviously highly distorting due to frozen in turbulence from the rapid temperature scans that we used. With longer pulses and more optimized interaction lengths, the theory leads us to believe that the threshold should be another order of magnitude lower. In addition, better isolation will provide scans with higher input powers so that the dynamic range of the enhancement as well as the temperature dependence of the risetimes may be studied.

In conclusion, the long pulse Nd:YAG laser verified the correctness of our theoretical approach that predicted the requirements, on the laser and the fluid, necessary to demonstrate the critical point enhancement of the nonlinear optical processes. It is unfortunate that the flow cell was not in a position to take advantage of this laser system.

References

1. M. J. Damzen, M. H. R. Hutchinson, and W. A. Schroeder, IEEE J. Quantum. Electron. **23**, 328 (1987).
2. J. O. Hirschfelder, C. F. Curtiss, and R. B. Bird, *Molecular Theory of Gases and Liquids* (Wiley and Sons, New York, 1954).
3. F. E. Hovis and J. D. Kelley, J. Opt. Soc. Am. B 4, 840 (1989)

SECTION 4

SUMMARY AND SUGGESTIONS FOR FUTURE WORK

4.1 Summary of Phase Transition Media

It is clear that a material of high nonlinear susceptibility will facilitate the low power application of phase conjugation . Where sub-millisecond response is necessary, today's materials are compatible only with pulsed lasers. CW lasers, which include most high power chemical lasers, cannot generate sufficient nonlinear response unless a very slow integrating media such as a photorefractor or artificial Kerr media is used. Paradoxically, a more sensitive nonlinear medium is needed to allow the application of phase conjugation to large high power chemical lasers systems - the very systems that often have severe beam combining problems and that require aberration correction. In addition, higher response should contribute to more efficient phase conjugate reflectors and thus higher power extraction efficiency in a laser system.

Table 4.1-1 is a list of current nonlinear material candidates and some of their desirable properties. Applications of nonlinear materials are limited by the availability of materials that simultaneously possess all of these characteristics. The most responsive materials (such as Na) often use a resonance that requires a narrow line tunable laser. In this program, a relatively simple and very high response material has been developed that offers a thousand-fold increase in response in return for a thousand-fold reduction in speed when compared to nonresonant electrostrictive nonlinear materials such as CS_2. This phase transition response time is in the microsecond range and it is adequate for most applications. Furthermore, the response and speed can be adjusted by controlling the reduced temperature.

Since the medium absorption is low it is well-suited to high power applications. Also, the flowing nozzle-driven system, as it is now constructed, is very well suited to high power applications. Not only is the fluid rapidly recirculated for cooling, but the sapphire windows are also well-cooled. This phase transition medium appears well suited as a substitute for a cw SBS medium in experiments such as the APACHE program or it's successor. For example, the lower threshold power requirements should greatly ease the engineering problems associated with the input windows.

Candidate Media	Sensitivity	Speed	Power Handling	Nonspecific Frequency
Kerr Media (electronic polariz.)	low	high	high	yes
Artificial Kerr Media	high	low	high	yes
Photorefractors	high	low	low	yes
Semiconductors	medium	high	low	no
Resonant Absorbers	high	high	low	no
Inverted Laser Media	medium	high	high	no
Metal colloids (plasma resonance)	high	high	medium	no
Phase Transition Media	high	high	high	yes

Fig. 4.1-1 Classification of candidate nonlinear optical materials.

Perhaps most interesting, the NCP phase transition media is predicted to have almost no redshift, even when used for Stimulated Rayleigh Scattering. This would make it possible to build phase conjugate resonators with a useful power, efficiency and speed of response. A phase conjugate resonator possesses the advantage of self-aligning like retroreflector resonators, and it has the added ability to correct aberrations and combine beams like a phase conjugate MOPA systems. In addition, it removes the need for nonreciprocal devices to separate the input and output beams.

The basic goal of validating the phase transition concept has been successfully completed in NCPF with a long pulse laser. The premise that the two-phase region of the flowing system would gain an additional degree of response has not yet been proven, but the response seen thus far in NCP mode demonstrated a peak phase conjugate reflectivity of 60% with input power levels of only a few kilowatts and response times in the microsecond range. This response is several orders of magnitude greater than conventional Kerr or electrostrictive media.

The engineering required to construct a flowing system for two-phase media exceeded our original estimates. As a result, the phase conjugate experiments in the two-phase region that were originally planned have not yet been carried out. However, this system is now operational, valuable operating time has been accumulated and a great deal of useful information has been learned about the operation of a flowing system in NCP conditions.

This experience should prove valuable for high power applications, where flow is required, regardless of the possibility of higher response from off-critical point operation.

The understanding of this new area of physics (a combination of nonlinear optics with thermodynamics) has greatly advanced during this program. Under the impetus of the NCP experimental work, we now understand the reflectivity, time dependence, signal to noise ratio and optimum interaction length for DFWM in NCPF. The response of NCPF is predicted to be nearly independent of the choice of material for all the cases we have examined, and adjustable by control of temperature.

In addition, SRS is predicted to dominate over SBS in NCPF for pulse lengths in the µsec range. The simple geometry of stimulated phase conjugators makes this discovery particularly useful. Because the redshift of this stimulated response is expected to be neglectable, this simple mechanism should be ideally suited for phase conjugate resonators.

4.2 Suggested Research topics

The experimental demonstration of this phenomenon is at its most basic stage today. A great deal remains to be done to test the range of possible performance from this class of materials. In addition to fluids, low power applications might benefit from solid state phase transitions near a Curie point.

As discussed in Section 2.1.1, both electrostrictive and thermal effects can lead to the large nonlinearities seen in our experiments. For low power operation, very large enhancements should be possible by adding an absorber to the fluid to enhance STRS. Obvious work that needs to be done includes higher sensitivity measurements of the freon absorption coefficient, measurement of the redshift of the SRS (this is expected to require heterodyne methods because of the low expected redshift), and long pulse DFWM experiments analogous to the short pulse work that was done in Section 3.4.4.

Demonstration of a phase conjugate resonator with this medium would have a far reaching impact on the design of laser resonators and there is also the possibility that mutually pumped phase conjugators could be based upon these media.

APPENDIX 1

ANGULAR DEPENDENCIES IN NEAR-CRITICAL-POINT FLUIDS

In this appendix we derive an expression for the light scattered by thermal fluctuations. Unlike the case of independently scattering density fluctuations, the light scattered in NCPF's is shown to depend on scattering angle, even when the analysis is confined to the plane orthogonal to the incident polarization. In Section A1.2 we discuss, for the case of long correlation length, the electrostrictive grating that results from the standing wave intensity pattern produced by two counter-propagating beams. We show, for the first time, that the directional dependence of the depth of such a grating is identical to that for scattering. We believe this result to be of fundamental interest. In Section A1.3 we conclude Appendix 1 with a quantification of the directional dependencies found in Sections A1.1 and A1.2, and show that for the experimentally accessible parameters these dependencies can be neglected.

A1.1. Angular Dependence of Light Scattered by Thermal Fluctuations

In this subsection we establish the formalism and the basic concepts that are used in later subsections of this appendix.

For isotropic fluids, the change in dielectric constant induced by an applied electromagnetic field, E, can be written as

$$\varepsilon(\vec{r}) = \varepsilon_B + \varepsilon_I \vec{E} \bullet \vec{E}, \tag{A1.1-1}$$

where ε_B is the background permittivity, and ε_I gives the nonlinear, intensity induced, response. It has been assumed in Eq. (A1.1-1) that there exists only a local relationship between the permittivity and the applied field.

We consider fluctuations in the permittivity $\delta\varepsilon(r)$ that can be resolved into Fourier components; i.e., the Fourier transform

$$\delta\varepsilon(\vec{q}) = V_I^{-1} \int_{V_I} d^3r\, \delta\varepsilon(\vec{r}) \exp(i\vec{q} \bullet \vec{r}), \tag{A1.1-2}$$

where V_I is the interaction volume, outside which $\delta\varepsilon(r)$ vanishes. The q'th component of $\delta\varepsilon$ appearing on the left hand side of Eq. (A1.1-2) can be thought of as the amplitude of a fluctuation grating associated with the wavevector q.

The relationship between the grating and the incident and scattered wavevectors is shown in Fig. A1-1. k_1 is the wavevector of the incident wave and k_2 is the wavevector of the scattered wave; the wavevector of the grating associated with the interference of the incident and scattered waves is q, as shown in the figure. For q matching—in the sense of Fig. A1-1—the wavevector of the laser induced grating, the fluctuations scatter light in the direction of the output field (k_2) as noise. When the wavevectors have the same amplitude

$$k = |\vec{k}_1| = |\vec{k}_2| \quad \rightarrow \quad q = 2k\sin(\theta/2), \tag{A1.1-3}$$

where θ is the angle between the incident and scattered wavevectors.

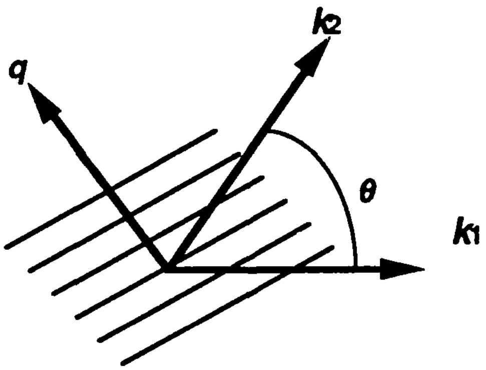

Fig. A1-1 k_1 is the wavevector of the incident light, k_2 is the wavevector of the scattered light, and q is the wavevector of the material refractive index grating associated with k_1 and k_2.

Using the fluctuation-dissipation theorem, and assuming a local relationship between electromagnetic field and $\delta\varepsilon$, one can show, via Eq. (A1.1-2) that

$$\left\langle |\delta\varepsilon(\vec{q})|^2 \right\rangle = 8\pi k_B T \varepsilon_I V_I^{-1}, \tag{A1.1-4}$$

where the angular brackets indicate an averaging over the beam interaction volume V_I. It is clear from Eq. (A1.1-4) that, since ε_I is a constant, $\delta\varepsilon$ is independent of q. In the remainder of this section we will show that this independence of q breaks down as the critical point is approached closely, and the correlation length approaches q^{-1}; i.e., when the local relationship assumed in Eq. (A1.1-1) is no longer valid.

Berne and Pecora [4] have considered the directional dependence of NCPF's. In determining the q dependence of the light scattering, their approach is to derive an expression for the density fluctuations ($\delta\rho$) in the Ornstein-Zernike approximation (OZA) [5,6]. From $\delta\rho$ it is a simple matter to obtain an expression for $\delta\varepsilon$ using the Clausius-Massotti relation. Corrections to the OZA have been proposed; however, for the temperature ranges of interest here, the uncorrected OZA has been found to agree well with experiment [6].

The scattered intensity is related to the structure factor $S(q)$ as follows:

$$I(d) = I_0\left(\frac{k_2^4}{16\pi^2 d^2 \varepsilon_0^2}\right)\left(\frac{\partial\varepsilon}{\partial\rho}\right)_T^2 \sin^2(\phi)S(q), \tag{A1.1-5}$$

where I_0 is the incident intensity, d is the distance from the scattering volume, k_2 is the scattered wavevector, ϕ is the angle between the incident polarization and the scattered wavevector, and ε, ρ, and T are the permittivity, density, and temperature, respectively.

Using the Clausius Massotti relation to solve for $\partial\varepsilon/\partial\rho$ we get

$$I(d) = I_0\left(\frac{n^2\pi\omega^2 D}{dc^2\varepsilon_0^2}\right)^2 \sin^2(\phi)S(q), \tag{A1.1-6}$$

where

$$D \equiv \varepsilon_0\frac{(r-1)(r+2)}{3}. \tag{A1.1-7}$$

Here, ω is the optical frequency, c is the speed of light in vacuum, and ε_0 is the permittivity of vacuum. The structure factor can be shown to be given by [4]

$$S(q) = V_I k_B T \rho^2 K_T\left(\frac{1}{1+(q/q_0)^2}\right). \tag{A1.1-8}$$

In the course of deriving Eq. (A1.1-8), the so-called "direct correlation function" was expanded in powers of q. The coefficients of this expansion can be expressed in terms of known or measurable quantities, and q_0. Clearly, from Eq. (A1.1-8), q is significant in determining the light scattering only when it is of the same order or larger than the parameter q_0. This observation, and the fact that it is the long range interactions in NCPFs that admit small q_0, motivates the definition of the correlation length

$$\xi \equiv q_0^{-1}. \tag{A1.1-9}$$

A1.2. Angular Dependence of Light Scattered by a Field Induced Grating

We now consider the case where the refractive index grating is induced by an electromagnetic field, rather than being the result of spontaneous fluctuations. For this purpose, two degenerate plane wave beams are assumed to contribute to the total field,

$$E = \frac{1}{2}\left\{\vec{e}_1 A_1 \exp\left[i\left(\vec{k}_1 \bullet \vec{r} - \omega t\right)\right] + \vec{e}_2 A_2 \exp\left[i\left(\vec{k}_2 \bullet \vec{r} - \omega t\right)\right]\right\} + c.c. \tag{A1.2-1}$$

where e_i are the unit polarization vectors, A_i are field amplitudes and k_i are the wavevectors. The intensity produced by the field in Eq. (A1.2-1) is

$$I = I_1 + I_2 + 2\vec{e}_1 \bullet \vec{e}_2 \sqrt{I_1 I_2}\cos(\vec{q} \bullet \vec{r}), \tag{A1.2-2}$$

where

$$\vec{q} \equiv \vec{k}_1 - \vec{k}_2.$$

The electrostrictive pressure is typically given by

$$\nabla P = \frac{1}{2}\rho\left(\frac{\partial \varepsilon}{\partial \rho}\right)\nabla E^2, \tag{A1.2-3}$$

where it is understood that E^2 is averaged over one optical period. It is necessary here to replace the pressure gradient with the following expression due to Fixman [7]

$$\nabla P = \left(\frac{\partial P}{\partial \rho}\right)\nabla\left(\rho - \frac{\nabla^2 \rho}{q_0^2}\right). \tag{A1.2-4}$$

The analysis leading to Eq. (A1.2-4) is somewhat lengthy and will therefore not be repeated here; the details can be found in Ref. [7]. The last term in parentheses becomes important when the correlation length approaches the characteristic size of the density fluctuations. Substituting Eq. (A1.2-4) into Eq. (A1.2-3) results in

$$\nabla\rho - \frac{\nabla^3\rho}{q_0^2} = \frac{1}{2}\rho^2 K_T\left(\frac{\partial\varepsilon}{\partial\rho}\right)\nabla E^2. \tag{A1.2-5}$$

We now wish to determine the effects implied by Eq. (A1.2-5) on the medium response as the correlation length becomes large. To this end we write the density in the form

$$\rho = \langle\rho\rangle + a_1\cos(\vec{q}\bullet\vec{r}) + a_2\cos(2\vec{q}\bullet\vec{r}) + \cdots \tag{A1.2-6}$$

Keeping only the first order grating term in the density and substituting Eq. (A1.2-16) into Eq. (A1.2-15), we get an expression for the amplitude of the first order grating in equilibrium with the applied field,

$$a_1 = \frac{1}{2}\rho^2 K_T\left(\frac{\partial\varepsilon}{\partial\rho}\right)\hat{e}_1\bullet\hat{e}_2 A_1 A_2 \frac{1}{1+(q/q_0)^2}. \tag{A1.2-17}$$

Comparing Eqs. (A1.2-7) and (A1.2-6) [with the aid of Eq. (A1.2-8)], we see that the effect of the long range correlations in a medium near its critical point is to reduce the field-induced grating response by the same factor that these correlations reduce the spontaneous fluctuations having the same wavevector q.

A1.3. Quantification of Angular Dependencies

We know of no data that presently exist for the correlation length and critical exponent of Freon 116. Thus, to obtain some sense of the relative importance of the anisotropy in scattering, we consider xenon, which has been characterized by Moldover [8]. The correlation length at a given temperature was found to be

$$\xi = \xi_0 T_r^{-0.63}\ ,\ T_r \equiv \frac{T - T_C}{T_C}, \tag{A1.3-1}$$

where $\xi_0=2.0\times10^{-10}$ m, and T_C is the critical temperature, T_C=289.73 K for xenon. We have computed the ratio $S(q)/S(0)$ for $\theta=\pi$ (backward scattering), where $S(0)$ is equivalent to the case where the correlation length vanishes. The data are plotted in Fig. A1.3-1.We find that the backward scattered intensity drops to ≈45% of the forward scattered intensity at 0.05 K from T_C, it then rises sharply to nearly 90% at 0.3 K from T_C.

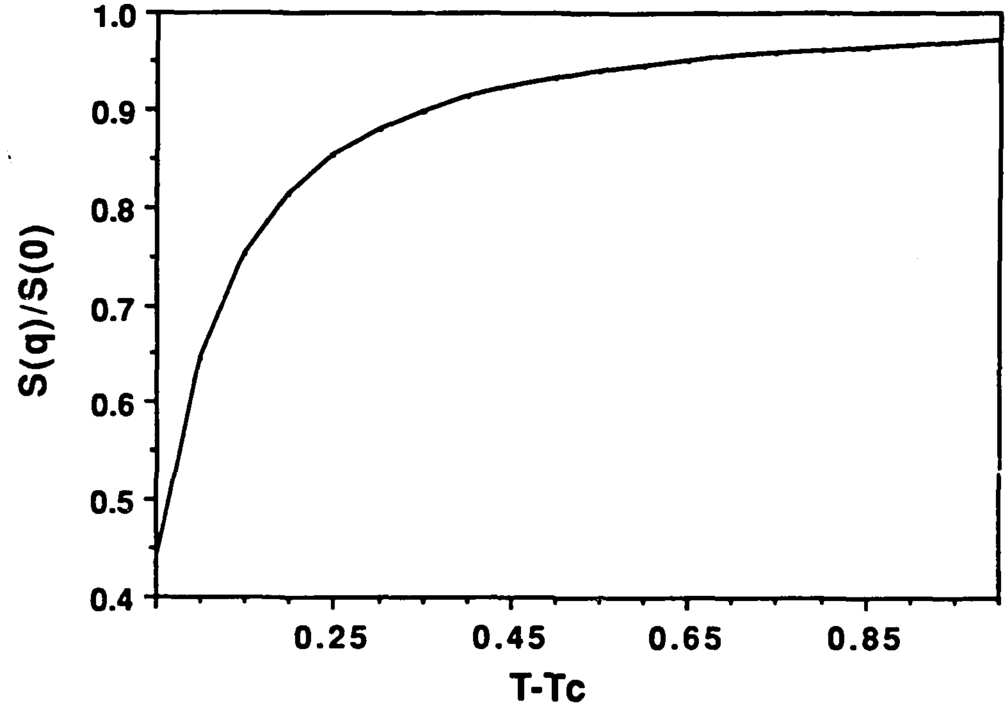

Fig. A1.3-1 Plot indicating importance of finite correlation length as a function of T-T_c.

We now make the following three points: i) Figure 2 is for xenon rather than Freon 116, which was used throughout the experimental portion of this program; ii) for T-T_c=>0.05 K, the backward scattering is reduced only by a factor of order unity, iii) one must exercise caution when using any equation of state near the critical point, and for small T-Tc the response is more strongly influenced by κ_T than by the anisotropies. It is precisely this region where inaccuracies in the equation of state become most important. Consequently, for order of magnitude calculations, it suffices to neglect anisotropies.

APPENDIX 2

STIMULATED RAYLEIGH SCATTERING IN C_2F_6 NEAR THE GAS-LIQUID CRITICAL POINT

This appendix is comprised of a paper that is to be submitted to Optics Letters. Its format, unlike the body of this final report, is that which is requested by the Optical Society of America for submissions to Optics Letters. The equation, figure, and table numbers are those used in the Optics Letter and have no relation to the numbers in the body of this report.

Stimulated Rayleigh scattering in C_2F_6 near the gas-liquid critical point

G. T. Bennett
K. L. Schehrer
and
V. Wang

Rockwell International
Rocketdyne Division
Canoga Park, California 91303

ABSTRACT

Stimulated scattering of 1.06 µm light from C_2F_6 (Freon 116) near its gas-liquid critical point has been observed experimentally. For an incident power of 1 kW the reflectivity was 60% at the trailing edge of a 20 µsec incident pulse. Based on the long risetime (> 10 µsec) that was observed for the reflectivity, and theoretical consideration of the gain and risetime behavior of stimulated scattering in near critical point media, we conclude that the observed scattering was stimulated Rayleigh scattering.

Of the many nonlinear optical processes known to phase conjugate an optical signal, stimulated scattering is especially attractive due to the relative insensitivity to alignment of the laser beams and optical elements. In contrast, for example, in four wave mixing one must ensure good overlap of counter-propagating beams to maximize the interaction length.

Because the compressibility of a fluid is characteristic of its response to perturbations (such as an applied field), and the compressibility can become quite large near the gas-liquid critical point (CP), near CP media are promising candidates for nonlinear optical processes. Of course this sensitivity to perturbations can lead to processes that are detrimental to efficient coherent scattering; the most notable such process is critical opalescence.

In this Letter, we present experimental results for the time and temperature dependences of the stimulated scattering from C_2F_6 near its CP. Theoretical considerations allow us to establish the criterion for determining whether the stimulated process is stimulated electrostrictive Rayleigh scattering (SeRS), or stimulated thermal Rayleigh scattering (StRS). Also, we discuss why previous investigators [2] have observed stimulated Brillouin scattering (SBS) rather than stimulated Rayleigh scattering (SRS).

Damzen et al. [1] used SBS to measure the speed of sound in C_2F_6, and they found that it reached a minimum in the vicinity of the gas-liquid CP. More recently, Hovis and Kelley [2] observed SBS reflections from near critical point $CClF_3$. In particular, they observed the small Brillouin frequency shifts expected near a minimum in the speed of sound. We remind the reader that speed of sound (v) can be written: $v=(\rho_0\kappa_S)^{-1/2}$, where κ_S is the *adiabatic* compressibility, and ρ_0 is the density. A minimum in v corresponds to a maximum in κ_S.

At steady state, and in the absence of thermal absorption, the gain for SBS is given by [3]

$$g_B = g^{e}_{B\max}\frac{1}{1+(2\Delta\omega/\Gamma_B)^{1/2}}, \tag{2a}$$

with

$$g^{e}_{B\max} = \frac{\kappa_S^{1/2}}{\eta}\frac{\omega_S^2\rho_0^{5/2}}{c^3nk^2}\left(\frac{\partial\varepsilon}{\partial\rho}\right)_T^2, \tag{2b}$$

where $\Delta\omega=\omega-\omega_B$, $\omega=\omega_L-\omega_S$, ω_L is the incident laser frequency, ω_S is the frequency of the scattered light, k is the difference between the incident and scattered wavevectors, $\Gamma_B=\eta k^2/\rho_0$, and $\eta=4/3\eta_S+\eta_B$, where η_S and η_B are the shear and bulk viscosities, respectively. The quantity η is believed finite near the critical point [4], and all other quantities in Eq. (2b) are finite. Since κ_S is large near the critical point [1], it follows that the Brillouin gain is slightly enhanced near the critical point. (The reason for stating "slightly" will become apparent shortly.)

While SBS can be identified with isentropic shifts in pressure, another type of stimulated scattering results from isobaric shifts in entropy, and this is termed stimulated Rayleigh scattering (SRS). In addition, two types of SRS can be identified, and in the slowly varying envelope approximation one can derive steady state gains for each [3]. For SeRS the steady state gain is

$$g^e_{RL} = g^e_{RL\max} \frac{4\omega / \Gamma_{RL}}{1 + (2\omega / \Gamma_{RL})^2}, \tag{3a}$$

where

$$g^e_{RL\max} = \frac{\omega_S(\kappa_T - \kappa_S)}{4c^2 n^2} \left(\rho_0 \frac{\partial \varepsilon}{\partial \rho}\right)_T^2, \tag{3b}$$

c is the speed of light in vacuum, n is the linear refractive index, ρ_0 is the density in the absence of an applied field, ε is the permittivity, Γ_{RL} is the Rayleigh linewidth, λ_T is the thermal conductivity, and C_P is the specific heat at constant pressure.

For StRS the steady state gain is

$$g^a_{RL} = g^a_{RL\max} \frac{4\omega / \Gamma_{RL}}{1 + (2\omega / \Gamma_{RL})^2}, \tag{4a}$$

where

$$g^a_{RL\max} = -\alpha \frac{c\kappa_T}{8\pi^2 n^3 \omega_S \lambda_T} \left(\frac{\partial P}{\partial T}\right)_V \left(\rho_0 \frac{\partial \varepsilon}{\partial \rho}\right)_T, \tag{4b}$$

and α is the linear absorption coefficient; P and T are the pressure and temperature, respectively. Using Eqs. (2b) and (3b), we find the ratio of the maximum gain coefficients in SeRS and SBS near the critical ($\kappa_T >> \kappa_S$) point to be

$$\frac{g^e_{RL\max}}{g^e_{B\max}} = \frac{\kappa_T}{\kappa_S^{1/2}} \frac{\eta c k^2}{4\rho_0^{1/2} n \omega_S}. \tag{5}$$

The quantities in the second factor of Eq. (5) are finite at the critical point; hence, at steady state, SeRS should be much stronger than SBS near the CP because of the divergence of the first factor. A similar argument for StRS leads to the conclusion that StRS also dominates SBS.

We now compare the electrostrictive and thermal effects in SRS near the critical point. Using Eqs. (4) and (6), we can write the ratio of the steady state gains for the two types of SRS as

$$\frac{g^{e}_{RL\max}}{g^{a}_{RL\max}} = \frac{2\pi^2\omega_S^2 n\lambda_T}{\alpha c^3}\left(\frac{\partial P}{\partial T}\right)^{-1}\left(\rho_0\frac{\partial\varepsilon}{\partial\rho}\right)_T \tag{6}$$

The Redlich-Kwong equation of state; i.e.,

$$P = \frac{RT}{V-\beta} - \alpha\frac{T^{-1/2}}{V(V+\beta)} \tag{7}$$

can be used to compute $\partial P/\partial T$, where the relevant parameters for C_2F_6 are given in Table 1. We use the Clausius-Massotti relation to determine $(\rho_0\partial\varepsilon/\partial\rho)$. With the absorption coefficient (α) in units of cm^{-1}, the ratio of the gains is $g_{RL}{}^{e}/g_{RL}{}^{a}=0.005/\alpha$; if $\alpha>5\times10^{-3}$ cm^{-1} then StRS dominates, and if $\alpha<5\times10^{-3}$ cm^{-1} then SeRS dominates.

We now turn to consideration of the transient, rather than steady state, case.

Rother et al. [7] have considered the transient response in StRS of an input step function pulse. They used a small signal and small gain approximation, neglected $\partial\varepsilon/\partial T$, and used the ansatz

$$E_S = e_S\exp(i\psi_S), \tag{8}$$

where E_S is the complex field amplitude of the scattered wave, and e_S and ψ_S are the real amplitude and phase. They found that the phase is given by

$$\psi^{a}_{RL}(z,t) = -g^{a}_{RL\max}I_L z\left[1-\exp\left(-\frac{1}{2}\Gamma_{RL}t\right)\right] + \psi_0. \tag{9}$$

We have used the same ansatz and approximations as Rother et al. [7] in considering the transient response for SeRS. We find that

$$\psi^{e}_{RL}(z,t) = -g^{e}_{RL\max}I_L z\left[1-\exp\left(-\frac{1}{2}\Gamma_{RL}t\right)\right] + \psi_0. \tag{10}$$

In Eqs. (9) and (10) the time dependence is given by the same risetime, $\tau_{RL}=2/\Gamma_{RL}=r_0C_P/2\lambda_T k^2$. The time constant τ_{RL} also increases rapidly for finite or weakly diverging λ_T because of the rapid increase with temperature in C_P near the CP. Using the numbers in Table 1 we find that even far from the critical point, where C_P is relatively small, the risetime is quite long: $\tau_{RL}\approx2.8$ μsec.

Equation (5) led us to conclude that at steady state near the CP, SRS is stronger than SBS. Assume for the moment that SRS is observed. Following Eq. (6) we established the value of α that determines whether SeRS or StRS dominates. However, both forms of SRS exhibit the same time dependence in the transient case [Eqs. (9) and (10)], and of course their time dependence is the same at steady state. Therefore, their time dependence is the same at all times. As a result, if we determine which of the forms of SRS dominates at steady state, we have also determined which of them dominates during the transient.

Now consider SBS vs. SRS near the CP. Based on Eq. (5) we conclude that, for sufficiently long times, electrostrictive SRS dominates. However, the time constant for SBS remains finite [3] as the CP is approached while that for SRS diverges. Consequently, for times short compared to Γ_{RL}, SBS can dominate until sufficient time has passed for SRS to increase. This explains why Hovis and Kelley [2] observed SBS with their short Q-switched pulses, while we observed SRS with our long, microsecond pulses.

Convenience motivated our choice of C_2F_6 to investigate the nonlinear optical properties of near CP fluids. C_2F_6 is non toxic, its critical point temperature (19.7 ^{0}C) is near room temperature, and its critical pressure is not difficult to achieve (3.0 MPa). The fluid was kept in an aluminium cell with a sapphire window centered on every face. The lengths of the optical axes through the fluid were 7.5 cm, 7.5 cm, or 20.0 cm depending on the orientation of the cell. A cooling unit was used to maintain the temperature of the fluid to better than 0.05 ^{o}C.

Using the equation of state [Eq. (7)], one can easily determine that κ_T is very sharply peaked near the CP. Consequently, near the CP, the effect of relatively small pressure or temperature inhomogeneities whose size is spatially macroscopic (of size $>>\lambda^3$), gives rise to very large inhomogeneities in κ_T. If fine temperature control cannot be maintained for long periods of time then the system does not become homogeneous, and one should expect that there are regions where κ_T is quite large, and others where it is not. In our apparatus we lack such fine temperature control, and we suspect that the scattering we observe is from many—not necessarily contiguous—regions that are very near the CP in PVT space.

The 1.06 μm wavelength light source was a CW Nd:YAG laser with two flashlamp pumped amplifiers. Pulses were shaped by two electrooptic modulators in series to increase the pulse-to-interpulse contrast. The switching of the Pockels cells was sufficiently rapid that the output pulse was square at the front and rear, with an adjustable duration of 2 to 20 μsec, and a variable energy of 1 to 200 mJ. However, peak power of 2.0 kW during an experiment was sufficient to observe the stimulated return when operating 0.2 ^{o}C away from the CP, and so the amplifiers were never operated near their rated output. The pulse shape was controlled by a feedback loop that sampled the pulse after the amplifiers and sent the error signal back to the Pockel's cells.

The portions of the experimental apparatus important to this discussion are shown in Fig. 1. The linearly polarized incident beam passed through a polarizing beam splitter followed by a quarter wave plate and a lens. The 15 cm focal length lens was placed in front of the cell so that when the ~6 mm diameter (twice diffraction limited) beam traversed the window-to-fluid interface its diameter was 4 mm, and at its focal point the diameter was approximately 20 μm; thus, the range in intensities in the cell was nominally 16 kW/cm^2 to 650 MW/cm^2. The latter number is slightly misleading; because of the large amount of scattering taking place in the cell, the beam waist was not measurable and was probably larger than the simple twice diffraction limit suggests. Also, at the exit window of the cell, the laser beam was severely distorted if it was discernable at all, which suggests that optimal focusing does not take place.

The return from the cell, orthogonally polarized relative to the incident light, was sent by the polarizing beam splitter to a photodetector. The signal from the photodetector was sent to a digitizer, where 512 samples were taken at 100 nsec intervals, and the averaging was over 100 pulses. The trigger for the digitizer was provided by the leading edge of the incident light; thus, the sampling was started at the same time relative to the input pulse, regardless of the reflectivity of the fluid.

In Fig. 2 we show the reflected pulse power as a function of time as the temperature was decreased through the critical point, the lowest curve corresponds to the highest temperature. We monitored the temperature both at the cell wall and at the water bath of the heat exchanger. We are confident that when we allowed the temperature of the bath and cell walls to approach the CP, the relative number of "high κ_T" regions increased. The long time constant expected for SRS is clearly evident in Fig. 2. In the inset of Fig. 2 we have plotted the same data as in the main figure, except that all peaks were normalized to unity. Remarkably, the time constant for each curve is the same, even though the measured gain differs by as much as a factor of three. One possible explanation is that λ_T is sometimes found to diverge near the [illegible]. Thus, while the gain diverges as C_P, the time constant only diverges as $\tau_{RL} \approx C_P/\lambda_T$; [illegible]e time constant diverges less strongly than the gain. However, we have no evidence to support this and we suspect that there may be some other cause.

In a separate set of experiments we measured the energy reflectivity and found it to be ~30%. This implied a peak reflectivity of ~60% at the trailing edge of the pulse.

Table 1. Numerical values used in calculations.

Symbol	Value
α	2.7782×10^{50} J m^3 Kg^{-1} K$^{-1/2}$
β	8.3123×10^{22} m^3 Kg^{-1}
C_P (NC)	$\approx$48 J kg^{-1} K^{-1}
ω_S	1.77×10^{15} sec^{-1}
λ_T (NC)	1.61×10^{-2} J m^{-1} s^{-1} K^{-1}

1. M. J. Damzen, M. H. R. Hutchinson, and W. A. Schroeder, IEEE J. Quantum. Electron. 23, 328 (1987).

2. F. E. Hovis and J. D. Kelley, J. Opt. Soc. Am. B 4, 840 (1989)

3. W. Kaiser and M. Maier, *Laser Handbook*, edited by F. T. Arrechi E. O. Schilz-DuBois, (North Holland, New York, 1972).

4. H. E. Stanley, *Introduction to Phase Transitions and Critical Point Phenomena*, (Oxford Science Publications, New York, NY, 1971).

5. J. O. Hirschfelder, C. F. Curtiss, and R. B. Bird, *Molecular Theory of Gases and Liquids* (Wiley and Sons, New York, 1954).

6. Dupont supplied data

7. W. Rother, D. Pohl and W. Kaiser, Phys. Rev. Lett. 22, 915 (1969).

Fig. 1. Schematic of the experimental set-up. BS=beam splitter, PBS=polarizing beam splitter, QWV=quarter wave plate, PD=photodetector, DZ=digitizer. The cell was filled with C_2F_6.

Fig. 2. Intensity as a function of time. The three curves were obtained consecutively as T was decreased towards the critical temperature (T_c), the lowest curve was at the highest T, and the highest curve was obtained nearest to T_C. The small figure in the inset was obtained by normalizing the three peaks in the main figure.

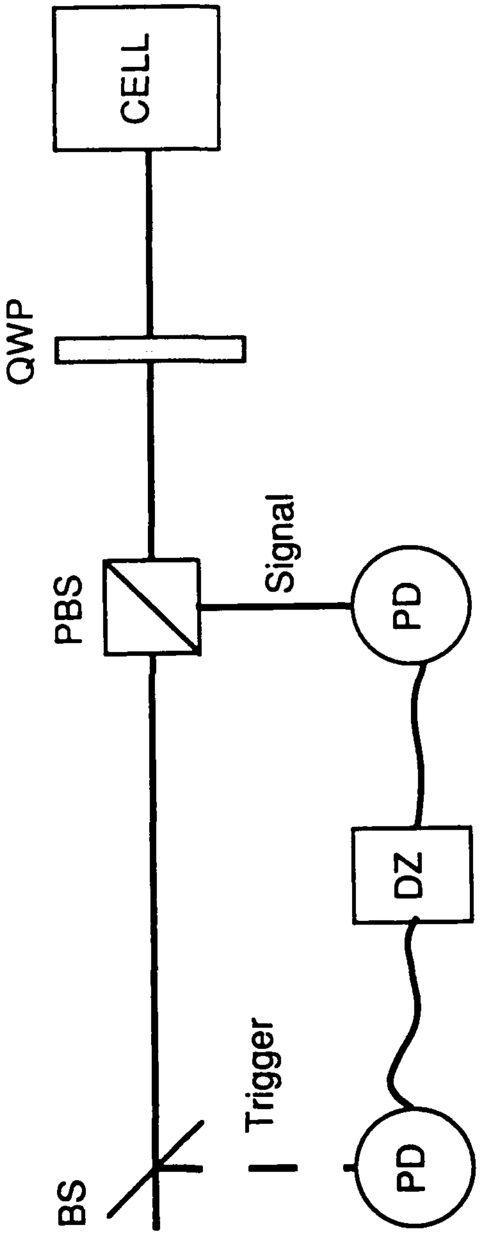

Fig. 1

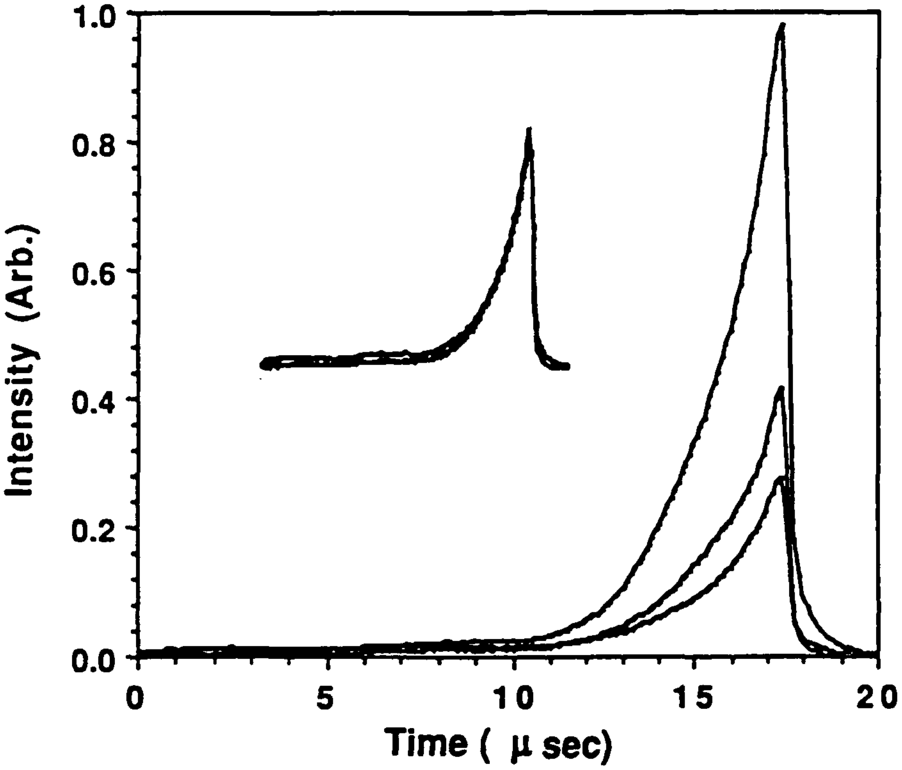

Fig. 2

APPENDIX 3

FLOW CELL ENGINEERING DRAWING

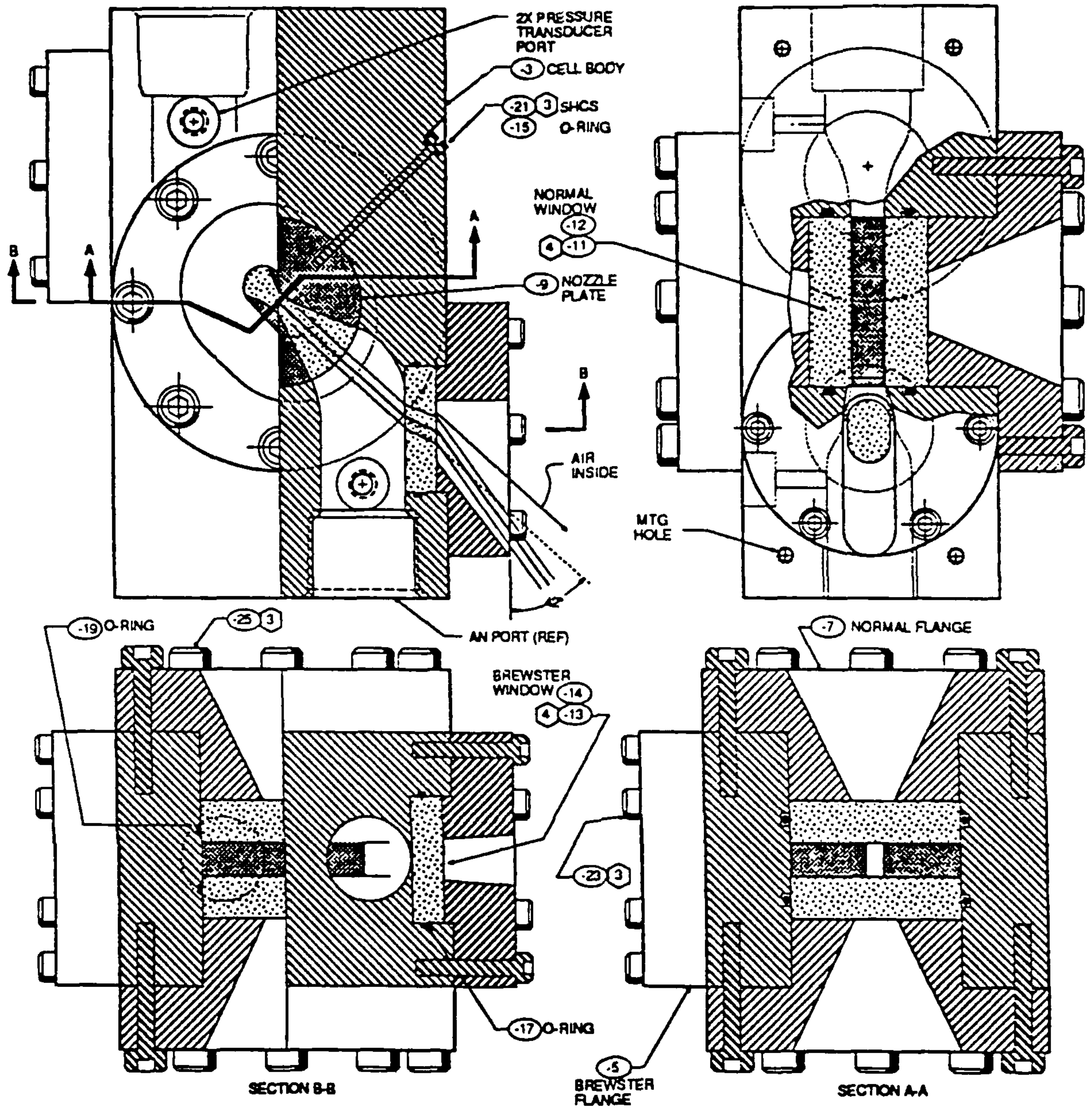

-1 ASSEMBLY OF

RELEASED DOCUMENT

REV STATUS OF SHEETS	REV	
	SHEET	ALL

NLESS OTHERWISE
PECIFIED TOLERANCES
DN: ANGLES = ± 30'
DECIMALS .XX = ± .03
.XXX = ± .010

DWN G. CULP 9-28-87	DATE
CHK	DATE
DSGN	STRUCT 87-9-29
MATL	
DESIGN ACTIVITY APVD R G. BARNSDALE	DATE [illegible]

Rockwell International Corporation
Rocketdyne Division
Canoga Park, California

FLOW CELL

SIZE	FSCM NO.	DRAWING NO.
A	02602	7R028654
SCALE	REV NC	SHEET 1 OF 7

ORM R 110-N-11 REV 3-78

(P. 101)

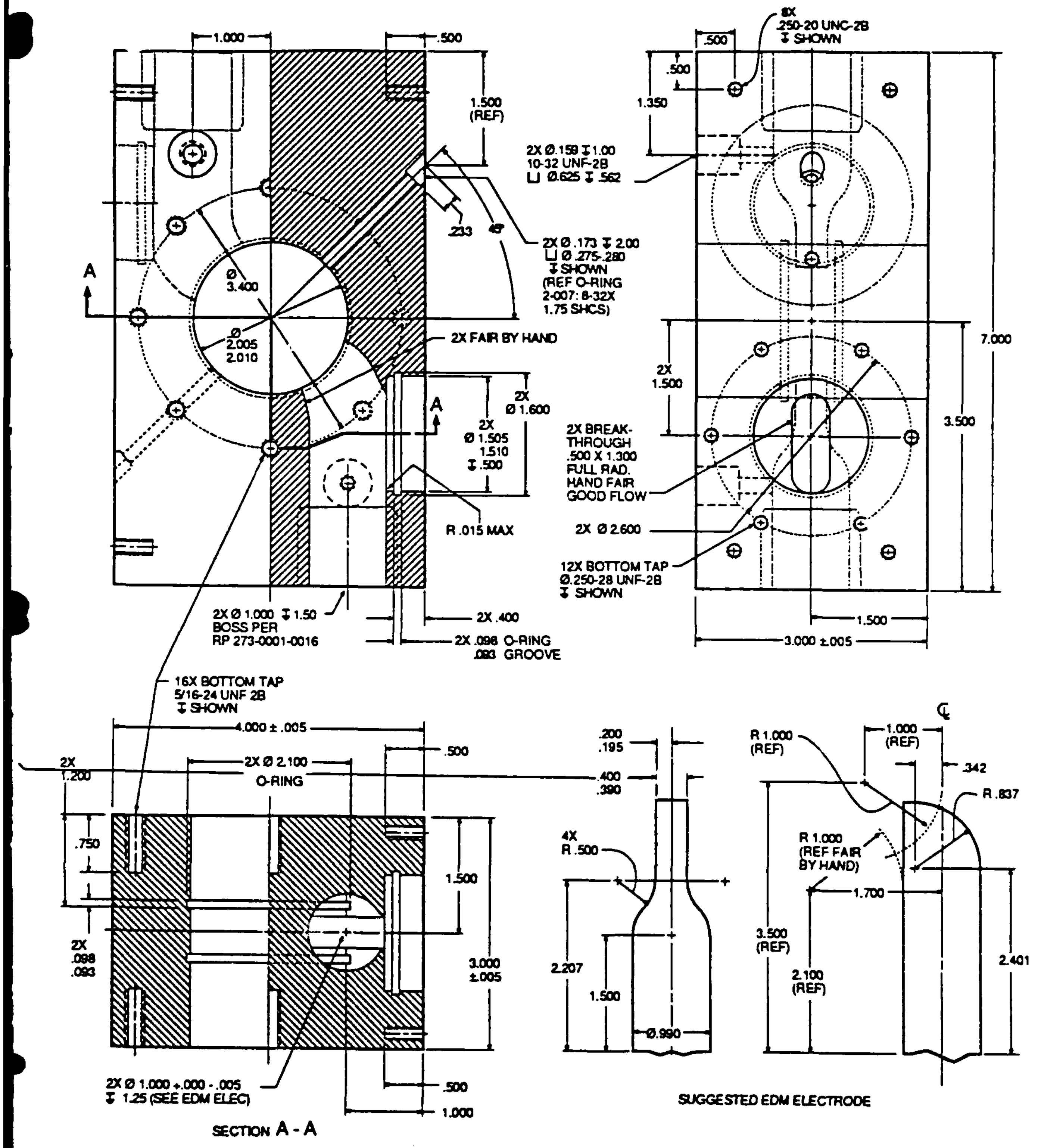

MATERIAL:
316 CRES

—3 BODY - FLOW CELL ①②

(P.102)

SIZE	FSCM NO.	DRAWING NO.
A	02602	7R028654

SCALE	REV nc	SHEET 2 OF 7